9-14-2023

# Constraining Subtleties of General Relativity and Quantum Phenomena of Gravitational Radiation with Gravitational-Wave Observations

Matthew Fowler Carney
*Washington University in St. Louis*

## Recommended Citation

Carney, Matthew Fowler, "Constraining Subtleties of General Relativity and Quantum Phenomena of Gravitational Radiation with Gravitational-Wave Observations" (2023). *Arts & Sciences Electronic Theses and Dissertations*. 3174.
https://openscholarship.wustl.edu/art_sci_etds/3174

WASHINGTON UNIVERSITY IN ST. LOUIS

Division of Physics

Dissertation Examination Committee:
Francesc Ferrer, Chair
Henric Krawczynski
James Mertens
Andrina Nicola
Yajie Yuan

# Constraining Subtleties of General Relativity and Quantum Phenomena of Gravitational Radiation with Gravitational-Wave Observations

by
Matthew Fowler Carney

A dissertation presented to
Washington University in
partial fulfillment of the
requirements for the degree
of Doctor of Philosophy

August 2023
Saint Louis, Missouri

# Contents

# List of Figures

# List of Tables

# Acknowledgements

Several people played crucial roles in helping me write this dissertation and I'd like to take a page to express my appreciation.

I'd like to thank my parents for their undying support and encouragement which has come in so many different forms. I am immensely privileged to have such wonderful role models in my life.

I'd like to thank my family Aunt Kathy, Uncle Tony, Travis, Brittany, Patrick, and Meg for always being there for me during my time in St. Louis.

I'd like to thank Les and Maddie Wade for their continued mentorship and friendship throughout my graduate school experience.

I'd like to thank Hannah Simmons for her undying support throughout writing this dissertation and for reminding me to stop and appreciate the flowers every once in a while.

Matthew Fowler Carney

*Washington University in St. Louis*
*August 2023*

# ABSTRACT OF THE DISSERTATION

## Constraining Subtleties of General Relativity and Quantum Phenomena of Gravitational Radiation with Gravitational-Wave Observations

by

Matthew Fowler Carney

Doctor of Philosophy in Physics

Washington University in St. Louis, 2023

Francesc Ferrer, Chair

Henric Krawczynski

James Mertens

Andrina Nicola

Yajie Yuan

Initial observations of gravitational-waves (GW) from the mergers of compact binaries have further solidified GR as an accurate model of gravity on large scales, as well as provided novel insight into the populations of the compact objects from which they originate. Next-generation detectors such as LISA, Einstein Telescope, and Cosmic Explorer are slated for operation in the next few decades and will bring with them vastly improved sensitivities and orders of magnitude more GW events. It is therefore imperative that model development and characterization of secondary effect—either smaller in magnitude in than current noise levels or too infrequent at current event rates for meaningful statistical statements to be made—be in place before observational data from these detectors becomes available. In this dissertation, we explore the observational prospects for two promising candidates for future–or even current–detection: observation of the GW middle-time-tail produced by off-axis massive perturbers, and measurement of quantum effects on GW propagation under the polymer quantization scheme. We present the waveform modifications that describe each of these phenomena, and provide the first constraints on the parameters describing them from analysis of existing GW data.

# Chapter 1

# Introduction

Einsteins General Theory of Relativity (GR) is one of the most successful physical theories of all time. On large scales it's strikingly accurate, describing myriad physical phenomena from the motion of planets to the origins of black holes, the most extreme physical systems in our Universe. Its success can be identified at its inception; Einstein reimagined gravity as a consequence of the marriage of space and time, promoting it from a simple force-mediated interaction between massive objects to a characteristic of a fundamental backdrop upon which all natural phenomena occur.

The advent of GR resolved so many astrophysical mysteries with its arrival. The precession of Mercury's orbit's inconsistency with Newtonian gravity. The observation of gravitational lensing further questioned the validity of classical physics, in which massless photons experience no gravitational force. While Newton's gravity fails to explain observations of each of these perplexing phenomena, they are natural consequences of GR. But perhaps the most interesting consequence of GR is one that has no Newtonian counterpart: the emission of gravitational waves from accelerating massive objects.

Einstein's GR predicts that, as a massive object moves through spacetime, information about its motion travels throughout the universe at the speed of light, analogous to the production of electromagnetic radiation from the acceleration objects charged under the electromagnetic force. Unlike electromagnetic radiation, however, gravitational waves are extremely weak and were long thought to be undetectable, to the extent that even Einstein himself claimed we would never directly observe them. We now have the good fortune to know he was mistaken. On September 14, 2015, the Laser Interferometer Gravitational-wave Observatory (LIGO), made the first direct observation of a gravitational wave caused by the coalescence of two black holes [1]. Since then, LIGO, joined by other GW observatories such as Virgo, have built up a growing catalog of 90+ gravitational wave detections, ushering in a new era of “gravitational-wave astronomy”. And while the production and success of the instrument was in and of itself a major scientific breakthrough, the analyses that follow a gravitational-wave detection are rich with new physics.

Through the use of Bayesian statistical techniques, we’ve successfully extracted from these spacetime perturbations the rich information they carry about their sources and spacetime itself. It’s allowed us to peer into the interiors of neutron stars, infer characteristics about our Universe’s populations of stellar remnants such as neutron stars (NS) and black holes (BH), and even test GR itself. Next-generation detectors such as Cosmic Explorer (CE) and Einstein Telescope (ET) will bring orders-of-magnitude improvements in sensitivity and orders-of-magnitude more GW events which will in turn likely bring definitive answers to the questions current detectors are just beginning to probe. However, in addition to improving constraints on phenomena under active investigation by current GW observatories, future detectors will be able to confirm or deny the existence of secondary effects: those either below the noise of current detectors or highly unlikely to be observed at current event rates. Such secondary effects may be able to probe the dark matter distribution on astrophysical scales or even quantum effects of GW propagation. In this work we develop models, forecast detection prospects, and provide the current-generation GW constraints for two such phenomenon: the middle-time-tail (MTT) of GW signals scattering off of massive perturbers, and quantum effects of GW propagation under the polymer quantization scheme.

This dissertation is organized as follows: In chapter II we’ll review the basics of

GR and the conditions that lead to GW production. Additionally, we'll look at some examples of sources of GWs. The anatomy and practical limitations of Michelson-like GW observatories are discussed in chapter III, followed by an overview of the parameter estimation techniques used to translate GW strain data into constraints on the source properties of the compact binary. Chapter 5 comprises the first of two projects that serve as the main material for this thesis: the search for GW MTT in confirmed LIGO detections. This will involve discussing the conditions required to produce a detectable glint, a model for the alteration it induces in the primary signal waveform, an injection study to characterize the detector response across glint parameter space, and finally the analysis of existing LIGO events. Chapter 6 outlines the second project which consists of an effective model for quantum corrections to propagating GWs under polymer quantization and the first empirical constraints placed on the characteristic scale of the theory.

# Chapter 2

# Gravitational Wave Physics

A healthy understanding of the mathematical description of spacetime will be a necessary prerequisite for understanding the search for extensions of GW models. In this chapter, we briefly review the derivation of spacetime's dynamical and constraint equations from first principles, known as the Einstein Field Equations (EFEs). From there, we demonstrate how in the linear perturbative limit these EOMs show that spacetime satisfies the familiar wave equation, which will set the groundwork for discussions of GW sources and a derivation of the Newtonian approximated plus and cross polarized GW waveform. Finally, we explore regimes in which the Newtonian approximation breaks down and compare modern waveform families that address these limitations.

## 2.1 Overview of General Relativity

### 2.1.1 The metric tensor

The foundational mathematical object of GR is the metric tensor whose components encode the relationship between spacetime basis vectors:

$$g_{\mu\nu} = \mathbf{g}(\mathbf{e}_\mu, \mathbf{e}_\nu) = \mathbf{e}_\mu \cdot \mathbf{e}_\nu, \tag{2.1}$$

where Greek indices such as $\mu$ and $\nu$ label the dimension of spacetime they are associated with. Alternative theories of gravity can extend beyond four dimensions, but here we restrict ourselves to a spacetime comprised of one timelike and three spacelike dimensions, thus $\mu, \nu \in \{0, 1, 2, 3\}$. The metric is symmetric, $g_{\mu\nu} = g_{\nu\mu}$, leaving 10 independent degrees of freedom. It should be noted that the metric components themselves do not carry physical meaning. Indeed, we can always choose coordinates in which the metric components are Minkowski and their first derivatives vanish. The second derivatives, however, only vanish when the underlying spacetime is flat and therefore have direct physical meaning.

In the absence of curvature, the basis vectors are strictly orthogonal, and thus the metric tensor takes a form that defines special relativistic mechanics known as the Minkowski metric,

$$g_{\mu\nu} = \eta_{\mu\nu} = \begin{pmatrix} -1 & 0 & 0 & 0 \\ 0 & 1 & 0 & 0 \\ 0 & 0 & 1 & 0 \\ 0 & 0 & 0 & 1 \end{pmatrix}, \tag{2.2}$$

where we've adopted the $(-, +, +, +)$ metric convention. The information contained in the metric can equivalently be expressed as a line element, which obviates its interpretation as encoding the relationship between basis vectors

$$ds^2 = g_{\mu\nu} dx^\mu dx^\nu \tag{2.3}$$

$$\eta_{\mu\nu} dx^\mu dx^\nu = -dt^2 + dx^2 + dy^2 + dz^2 \qquad \text{(Minkowski)}. \tag{2.4}$$

We also distinguish between vectors that transform with (covariant) and against (contravariant) the metric, denoted by subscripts and superscripts respectively[1]. To visually

---

[1] The indices of covariant and contravariant vectors are sometimes colloquially referred to as "downstairs" and "upstairs" , respectively.

simplify the equations we will encounter in GR, we'll adopt the familiar Einstein summation convention in which multiplication between contravariant and covariant vectors imply summation over their components:

$$x^\mu x_\mu \equiv \sum_0^3 x^\mu x_\mu = x^0 x_0 + x^1 x_1 + x^2 x_2 + x^3 x_3. \tag{2.5}$$

"Raising" and "lowering" indices–transformation between covariant and contravariant vector forms–is also performed by contraction of vectors with the metric

$$x_\mu = g_{\mu\nu} x^\nu, \tag{2.6}$$

while the inverse transformation from covariant to contravariant, is performed by contraction with the inverse metric $g^{\mu\nu}$

$$\begin{aligned} x^\mu &= g^{\mu\nu} x_\nu & (2.7) \\ &= g^{\mu\nu} g_{\nu\alpha} x^\alpha & (2.8) \\ &= x^\mu & (2.9) \end{aligned}$$

We can further visually simplify our equations by employing defining shorthand notation for derivatives with respect to covariant coordinates. That is, given covariant vector $x^\mu$, and some function $f(x^\mu)$, we express the derivative of $f$ with respect to the coordinates $x^\mu$ as

$$\frac{\partial f(x^\mu)}{\partial x^\mu} = \partial_\mu f = f_{,\mu}. \tag{2.10}$$

Note that the derivative of a function with respect to a contravariant vector transforms *covariantly* and thus should be treated as a "downstairs" index for summation purposes.

### 2.1.2 The Einstein Field Equations

Contrary to Eq. 2.2, spacetime is not ubiquitously flat. The components of the metric are not constant and evolve over time in interesting and non-trivial ways. And indeed the evolution of the metric components in curved spacetime has fascinating consequences that will lay the groundwork for the work presented here. The first of these consequences is reflected in the geodesic equation:

$$\frac{d^2x^\alpha}{d\tau^2} = -\left\{\frac{1}{2}g^{\alpha\beta}\left(-\frac{dg_{\beta\mu}}{dx^\nu} + \frac{dg_{\beta\nu}}{dx^\mu} + \frac{dg_{\mu\nu}}{dx^\beta}\right)\right\}\frac{dx^\mu}{d\tau}\frac{dx^\nu}{d\tau} \tag{2.11}$$

$$= -\Gamma^\alpha{}_{\mu\nu}\frac{dx^\mu}{d\tau}\frac{dx^\nu}{d\tau}, \tag{2.12}$$

where $\tau$ is the proper time according to an observer at position $x^\alpha$, and we've defined

$$\Gamma^\alpha{}_{\mu\nu} = \frac{1}{2}g^{\alpha\beta}\left(-\partial_\nu g_{\beta\mu} + \partial_\mu g_{\beta\nu} + \partial_\beta g_{\mu\nu}\right), \tag{2.13}$$

known as the Christoffel coefficients. The geodesic equation communicates the first of many profound consequences of the dynamics of curved spacetime: in the absence of any external forces, a test particle whose spacetime location is given by $x^\alpha$ will not remain constant.

The geodesic equation does not describe the dynamics of the metric itself, though the Christoffel symbols that they introduce do play a crucial role. Indeed, the object that lays the foundation for the metric's dynamical equations, the Riemann curvature tensor, is defined in terms of the Christoffel coefficients and its derivatives,

$$R^\mu{}_{\nu\delta\gamma} = \Gamma^\mu{}_{\gamma\nu,\delta} - \Gamma^\mu{}_{\delta\nu,\gamma} + \Gamma^\mu{}_{\delta\lambda}\Gamma^\lambda{}_{\gamma\nu} + \Gamma^\mu{}_{\gamma\lambda}\Gamma^\lambda{}_{\delta\nu}. \tag{2.14}$$

which is related to a vector's deviation from its original state when parallel transported around a closed contour in spacetime. The Riemann tensor contains more curvature information than is required to describe the metrics dynamics. To eliminate redundancies, the Riemann tensor can be summed over its first and third indices to produce the Ricci tensor:

$$R_{\mu\nu} = R^{\alpha}{}_{\mu\alpha\nu}. \tag{2.15}$$

This summation eliminates some information about spacetime shear contained within the Riemann tensor. The Ricci tensor can finally be further contracted with the metric to produce a single scalar curvature

$$R = R^{\mu}{}_{\mu}. \tag{2.16}$$

From here, we insert the scalar curvature into the action, making the profound statement that the curvature of spacetime contributes to the energy content of the Universe, producing the famous Einstein-Hilbert action defined on the manifold $\mathcal{M}$,

$$S_{\text{EH}} = \frac{1}{2}\int_{\mathcal{M}} \sqrt{-g}\,\{\alpha R + 2\mathcal{L}_m\}\, d^4x, \tag{2.17}$$

where $\mathcal{L}_m$ is the Lagrangian density for the matter content of the Universe which describes its energy content, $\alpha$ is a constant of proportionality (to be determined later on), and $g = g_{\mu\nu}g^{\mu\nu}$. Minimizing the Einstein-Hilbert action results in the following:

$$\begin{aligned}\delta S_{\text{EH}} = \frac{1}{2}\int_{\mathcal{M}} \sqrt{-g}\left\{-\frac{\alpha}{2}g_{\mu\nu}R + \alpha R_{\mu\nu} + 2\frac{\partial \mathcal{L}_m}{\partial g_{\mu\nu}} - g_{\mu\nu}\mathcal{L}_m\right\}\delta g^{\mu\nu} d^4x \\ + \frac{1}{2}\int_{\mathcal{M}} \alpha\sqrt{-g}g^{\mu\nu}\delta R_{\mu\nu} d^4x = 0,\end{aligned} \tag{2.18}$$

where the second integral, present when the underlying spacetime manifold has a boundary, can be expressed as a surface term after invoking Stokes' theorem. Adding the

Gibbons-Hawking-York term

$$S_{\rm GHY} = \int_{\partial\mathcal{M}} d^3y\sqrt{h}K \tag{2.19}$$

to Eq. 2.17 ensures the variational principle is well-defined. Eq. 2.19 is an integral over the 3-dimensional boundary hypersurface $\partial\mathcal{M}$ parameterized by the coordinates $y^a$, $h = \det[h_{ab}]$ is the determinant of the induced metric on the boundary which satisfies

$$h_{ab} = g_{\mu\nu}e^\mu_a e^\nu_b \tag{2.20}$$

where the components of the basis vectors, $e^\mu_a$, encode the relationship between the manifold and boundary coordinates,

$$e^\mu_a = \left(\frac{\partial x^\mu}{\partial y^a}\right)_{\partial\mathcal{M}}, \tag{2.21}$$

for $a \in 1, 2, 3$. Finally, $K$ is the trace of the extrinsic curvature

$$K = h^{\mu\nu}(n_{\mu,\nu} - \Gamma^\rho_{\mu\nu}n_\rho) \tag{2.22}$$

where $h^{\mu\nu} \equiv g^{\mu\nu} - n^\mu n^\nu$ and $n^\mu$ is the unit normal to the hypersurface. Variation of the sum of these two actions yields

$$\begin{align}
\delta S_{\rm total} &= \delta S_{\rm EH} + \delta S_{\rm GHY} \tag{2.23}\\
&= \frac{1}{2}\int_{\mathcal{M}} \sqrt{-g}\left\{-\frac{\alpha}{2}g_{\mu\nu}R + \alpha R_{\mu\nu} + 2\frac{\partial\mathcal{L}_m}{\partial g_{\mu\nu}} - g_{\mu\nu}\mathcal{L}_m\right\}\delta g^{\mu\nu}d^4x \tag{2.24}
\end{align}$$

where we recognize that setting the integrand equal to 0 is one solution of this equation. This leaves us with the equations of motion for the metric:

$$\alpha\left[R_{\mu\nu} - \frac{1}{2}g_{\mu\nu}R\right] = g_{\mu\nu}\mathcal{L}_m - 2\frac{\partial\mathcal{L}_m}{\partial g_{\mu\nu}}. \tag{2.25}$$

The left hand side of Eq. 2.1.2 is a rank 2 tensor known as the Einstein tensor, $G_{\mu\nu}$, and is related to the curvature of spacetime:

$$G_{\mu\nu} \equiv R_{\mu\nu} - \frac{1}{2} g_{\mu\nu} R. \tag{2.26}$$

From the righthand side, which contains information about the energy density contents of the Universe not due to curvature (baryonic matter, radiation, etc), we define *stress-energy tensor*:

$$T_{\mu\nu} \equiv g_{\mu\nu} \mathcal{L}_m - 2 \frac{\partial \mathcal{L}_m}{\partial g_{\mu\nu}}. \tag{2.27}$$

Finally, we arrive at the Einstein Field Equations,

$$G_{\mu\nu} = \frac{8\pi G}{c^4} T_{\mu\nu}, \tag{2.28}$$

where we've chosen $\alpha = c^4/8\pi G$ such that taking the non-relativistic limit gives the Newtonian gravitational relation. Eq. 2.28 are known as the Einstein field equations (EFE). The indices $\mu$ and $\nu$ both range from 0 to 3, for a possible 16 combinations. The symmetry of the Ricci tensor eliminates 6 duplicate equations. Of the remaining 10 equations, only 6 are independent due to the four Bianchi identities, representing the remaining gauge degrees of freedom.

The Einstein tensor contains only curvature information, being constructed strictly from the metric and its first and second order derivatives. The stress-energy tensor on the righthand side represents all other energy contributions: matter, radiation, dark matter, etc. and has the following anatomy:

$$T^{\mu\nu} = \left(\begin{array}{c|c} \text{energy} & \leftarrow \text{energy flux} \rightarrow \\ \text{density} & \\ \hline & \\ \uparrow & \nwarrow \qquad \nearrow \\ \text{momentum} & \text{stress} \\ \text{density} & \text{tensor} \\ \downarrow & \swarrow \qquad \searrow \\ & \end{array}\right).$$

The components of the stress-energy tensor, shown above in its contravariant representation, are familiar for certain sources:

$$T^{00} = \rho \qquad\qquad T^{00} = \frac{1}{c^2}\left(\frac{\epsilon_0}{2}E^2 + \frac{1}{2\mu_0}B^2\right). \tag{2.29}$$

$$\text{(perfect fluid)} \qquad\qquad \text{(electromagnetic field)} \tag{2.30}$$

The mixed time-space indices are the momentum density ($T^{i0}$) and energy flux ($T^{0i}$) and the purely spatial components $T^{ij}$, are known as the stress tensor. The stress tensor diagonals $T^{ii}$ represent directional pressures, while its off-diagonal components are shears.

### 2.1.3 Consequences of linearized GR

Consider a small perturbation to the Minkowski metric (Eq. 2.2), $h_{\mu\nu}$ such that the metric now looks like

$$g_{\mu\nu} = \eta_{\mu\nu} + h_{\mu\nu} \tag{2.31}$$

In this section, we'll derive the Riemann and Ricci tensors, scalar curvature, and ultimately the EFEs that govern the evolution of the above metric tensor. Moving forward, we'll assume the metric perturbation is small, i.e. $|h_{\mu\nu}| \ll 1$, which will allow us to ignore terms $\mathcal{O}(h^2)$ and higher. Under this simplifying assumption, Eq. 2.31 has inverse

$$g^{\mu\nu} = (\eta_{\mu\nu} + h_{\mu\nu})^{-1} = \eta^{\mu\nu} - h^{\mu\nu} + \mathcal{O}(h^2), \tag{2.32}$$

where again $\eta_{\mu\nu}$ is the Minkowski metric. Taking only linear terms in $h$, the Christoffel coefficients are

$$\Gamma^{\alpha}{}_{\mu\nu} = \frac{1}{2}\eta^{\alpha\beta}\left[h_{\beta\mu,\nu} + h_{\beta\nu,\mu} - h_{\mu\nu,\beta}\right]. \tag{2.33}$$

From the Christoffel symbols, the next step is to construct the Riemann tensor. Note that the last two terms in Eq. 2.14 will produce only terms quadratic in $h$, making the Riemann tensor

$$R^{\mu}{}_{\nu\delta\gamma} = \Gamma^{\mu}{}_{\gamma\nu,\delta} + \Gamma^{\mu}{}_{\delta\nu,\gamma}. \tag{2.34}$$

This yields the following linearized Riemann tensor:

$$R^{\mu}{}_{\nu\delta\gamma} = \frac{1}{2}\eta^{\mu\beta}(h_{\beta\gamma,\nu\delta} - h_{\gamma\nu,\beta\delta} - h_{\beta\delta,\nu\gamma} + h_{\delta\nu,\beta\gamma}). \tag{2.35}$$

Summing over the first and third indices, we arrive at the Ricci tensor. With the derivatives written out explicitly, this looks like

$$R_{\nu\gamma} = R^{\mu}{}_{\nu\mu\gamma} = \frac{1}{2}\left\{\frac{\partial^2 h^{\mu}{}_{\gamma}}{\partial x^{\nu}\partial x^{\mu}} - \eta^{\mu\beta}\frac{\partial^2 h_{\gamma\nu}}{\partial x^{\beta}\partial x^{\mu}} - \frac{\partial^2 h^{\mu}{}_{\mu}}{\partial x^{\nu}\partial x^{\gamma}} + \frac{\partial^2 h^{\mu}{}_{\nu}}{\partial x^{\mu}\partial x^{\gamma}}\right\}. \tag{2.36}$$

Contracting the Ricci tensor with the inverse metric yields the last quantity needed for the Einstein tensor. Again, many terms quadratic in $h$ are spawned in the process which can be safely ignored for small $h$. The surviving terms of the scalar curvature are

$$R = g^{\nu\gamma} R_{\nu\gamma} \tag{2.37}$$

$$= (\eta^{\nu\gamma} - h^{\nu\gamma}) \frac{1}{2} \left\{ \frac{\partial^2 h^{\mu}{}_{\gamma}}{\partial x^{\nu} \partial x^{\mu}} - \eta^{\mu\beta} \frac{\partial^2 h_{\gamma\nu}}{\partial x^{\beta} \partial x^{\mu}} - \frac{\partial^2 h^{\mu}{}_{\mu}}{\partial x^{\nu} \partial x^{\gamma}} + \frac{\partial^2 h^{\mu}{}_{\nu}}{\partial x^{\mu} \partial x^{\gamma}} \right\} \tag{2.38}$$

$$= \frac{1}{2} \left\{ \eta^{\nu\gamma} \frac{\partial^2 h^{\mu}{}_{\gamma}}{\partial x^{\nu} \partial x^{\mu}} - \eta^{\nu\gamma} \eta^{\mu\beta} \frac{\partial^2 h_{\gamma\nu}}{\partial x^{\beta} \partial x^{\mu}} - \eta^{\nu\gamma} \frac{\partial^2 h^{\mu}{}_{\mu}}{\partial x^{\nu} \partial x^{\gamma}} + \eta^{\nu\gamma} \frac{\partial^2 h^{\mu}{}_{\nu}}{\partial x^{\mu} \partial x^{\gamma}} \right\} \tag{2.39}$$

$$R = \frac{\partial^2 h^{\mu\nu}}{\partial x^{\mu} \partial x^{\nu}} - \eta^{\mu\nu} \frac{\partial^2 h}{\partial x^{\mu} \partial x^{\nu}}, \tag{2.40}$$

where $h = \eta^{\mu\nu} h_{\mu\nu}$ is the trace of the metric perturbation. Combining the Ricci tensor and scalar curvature according to Eq. 2.26 gives us the Einstein tensor for a perturbed Minkowski spacetime:

$$\begin{aligned} G_{\mu\nu} = \frac{1}{2} &\left\{ \frac{\partial^2 h^{\sigma}{}_{\nu}}{\partial x^{\mu} \partial x^{\sigma}} - \eta^{\sigma\beta} \frac{\partial^2 h_{\nu\mu}}{\partial x^{\beta} \partial x^{\sigma}} - \frac{\partial^2 h^{\sigma}{}_{\sigma}}{\partial x^{\mu} \partial x^{\nu}} + \frac{\partial^2 h^{\sigma}{}_{\mu}}{\partial x^{\sigma} \partial x^{\nu}} \right\} \\ &- \frac{1}{2} (\eta_{\mu\nu} + h_{\mu\nu}) \left( \frac{\partial^2 h^{\mu\nu}}{\partial x^{\mu} \partial x^{\nu}} - \eta^{\mu\nu} \frac{\partial^2 h}{\partial x^{\mu} \partial x^{\nu}} \right). \end{aligned} \tag{2.41}$$

In its current form, the significance of Eq. 2.41 is obfuscated by redundant gauge degrees of freedom. To simplify, we define the the trace-reversed metric perturbation

$$\bar{h}_{\mu\nu} = h_{\mu\nu} - \frac{1}{2} \eta_{\mu\nu} h^{\sigma}{}_{\sigma}, \tag{2.42}$$

and partially fix the gauge according to the Lorenz condition

$$\partial_{\mu} \bar{h}^{\mu\nu} = 0 \tag{2.43}$$

in which the Einstein Field Equations reduce to

$$-\eta^{\alpha\beta} \frac{\partial^2 \bar{h}_{\mu\nu}}{\partial x^{\alpha} \partial x^{\beta}} \approx \frac{16\pi G}{c^4} T_{\mu\nu}. \tag{2.44}$$

We recognize $\eta^{\alpha\beta}\frac{\partial^2}{\partial x^\alpha \partial x^\beta} \equiv \Box$ as the d'Alembertian operator. Thus, for a small perturbation to a flat Minkowski metric, the Einstein Field Equations take the form of a wave equation sourced by $T_{\mu\nu}$:

$$-\Box \bar{h}_{\mu\nu} \approx \frac{16\pi G}{c^4} T_{\mu\nu}, \tag{2.45}$$

which describe gravitational wave solutions. For illustrative purposes let us consider the special case of a vacuum in which $T_{\mu\nu}$ vanishes, which should hold for cases in which the GWs are propagating far from their source:

$$-\Box \bar{h}_{\mu\nu} \approx 0. \tag{2.46}$$

Aligning the direction of propagation with one of our basis vectors, such as the $x^3$ (or $\hat{z}$) direction, the only surviving components of $\bar{h}_{\mu\nu}$ are $\bar{h}_{22} = -\bar{h}_{11}$, and $\bar{h}_{12} = \bar{h}_{21}$, the first of which is a consequence of the tracelessness of $\bar{h}_{\mu\nu}$, and the second is required to preserve the symmetry of the metric. All of these conditions amount to the Transverse-Traceless (TT) gauge. Only two unique metric perturbations exist under these conditions in the TT-gauge, corresponding to the diagonal elements and the off-diagonal elements of $\bar{h}_{\mu\nu}$. Defining the two remaining degrees of freedom

$$\bar{h}_{11}(x^0, x^3) \equiv h_+(x^0, x^3) \tag{2.47}$$

$$\bar{h}_{12}(x^0, x^3) \equiv h_\times(x^0, x^3) \tag{2.48}$$

the perturbed metric takes the form

$$g_{\mu\nu} + \bar{h}_{\mu\nu} = \begin{pmatrix} -1 & 0 & 0 & 0 \\ 0 & 1 + h_+(x^0, x^3) & h_\times(x^0, x^3) & 0 \\ 0 & h_\times(x^0, x^3) & 1 - h_+(x^0, x^3) & 0 \\ 0 & 0 & 0 & 1 \end{pmatrix}. \tag{2.49}$$

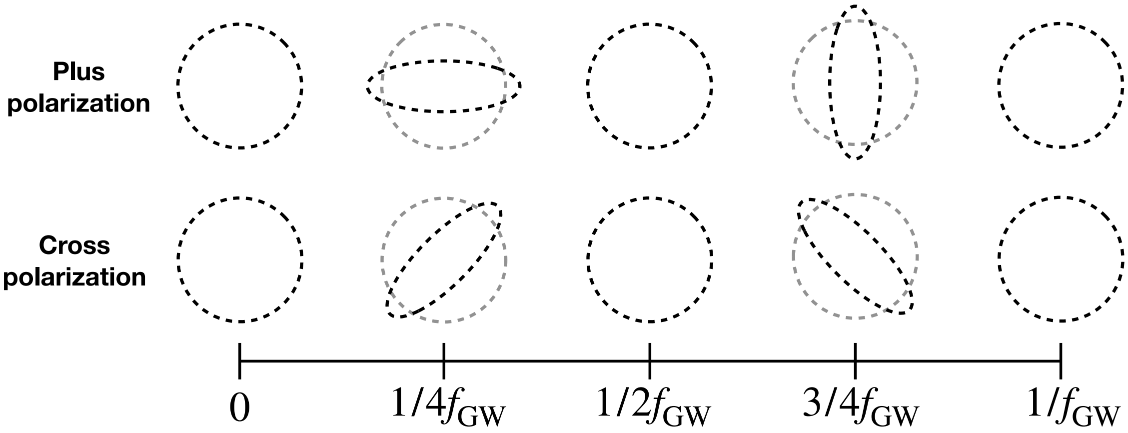

Figure 2.1: The effect of a plus-polarized (top) and cross-polarized (bottom) gravitational wave on a ring of otherwise undisturbed test particles as a function of the GW period $\tau_{\mathrm{GW}} \equiv 1/f_{\mathrm{GW}}$. In GR, these two polarizations form a basis for the set of all possible gravitational-wave strains.

Fig. 2.1 illustrates the two distinct ways in which the *plus* and *cross* polarizations of the gravitational wave alter physical distances. Note that despite restricting propagation of the GWs to the $x^3$ direction, the plus and cross polarizations still form a complete basis for GW propagation in GR. In reality any GWs detected by a GW observatory will not always be aligned orthogonally to the detector axis, but regardless of its orientation relative to the detector, the GWs can always be decomposed into a linear combination of plus and cross polarizations. The mathematical treatment for disentangling GWs into their plus and cross polarizations involves taking into account the detector geometry and orientation relative to the GWs known as an "antenna function", which we will discuss later on.

## 2.2 Sourcing Gravitational Waves[2]

GW signals encountered in this thesis are necessarily produced by some source with an associated non-zero stress-energy tensor. Modeling their signals therefore requires solving Eq. 2.45 and may even be inaccurate when terms $\mathcal{O}(h^2)$ are ignored. A popular

---

[2] This section very closely follows reference [2]

remedy is to define an effective stress-energy tensor which treats higher order perturbations as additional effective sources,

$$\Box\bar{h}_{\mu\nu} = -\frac{16\pi G}{c^4}\tau_{\mu\nu} \tag{2.50}$$

where the effective stress-energy tensor is defined as

$$\tau_{\mu\nu} = T_{\mu\nu} + \frac{c^4}{16\pi G}\Lambda_{\mu\nu}(h, \partial h, \partial^2 h), \tag{2.51}$$

with $\Lambda_{\mu\nu}$ being the source term for higher-order perturbations. Note that we've restored the equality here as we've reintroduced the higher-order terms. Eq. 2.50 can be solved with a Green's function method

$$\bar{h}_{\mu\nu}(x^\mu) = \frac{4G}{c^4}\int d^3x \frac{\tau_{\mu\nu}(x^0 - |\vec{x} - \vec{x}'|/c, \vec{x})}{|\vec{x} - \vec{x}'|} \tag{2.52}$$

Ultimately, we're interested in a model for the signal as it appears in a GW observatory on Earth, i.e. far from the source. We can therefore safely relax some of our assumptions in order to simplify calculation. The relevant scales of the system are $R$, the characteristic length scale of the GW source, $\lambda$, the wavelength of the produced gravitational wave, and $r$, the distance from the source to the observer. In this context "far from the source" implies $R \ll \lambda \ll r$. [3] Under these conditions assuming $|\vec{x} - \vec{x}'| \simeq r$ will not introduce any significant errors.

Additionally, we're interested only in the metric perturbations in the TT-gauge of which the only non-vanishing components are spatial, $h_{ij}^{\mathrm{TT}}$. Fortunately, we can leverage the following identity which is a consequence from conservation of the effective stress-

---

[3] We'll see later on that GWs produced from inspirally compact object binaries have a characteristically non-trivial frequency (and thus wavelength) evolution. Thankfully the range over which the wavelengths vary for all sources we will consider still fall under the far-field limit.

energy tensor $\partial^\mu \tau^{\mu\nu} = 0$:

$$\tau^{ij} = \frac{1}{2}\frac{\partial^2}{\partial(x^0)^2}(x^i x^j \tau^{00}) + \frac{\partial}{\partial x^k}\left(x^i \tau^{jk} + x^j \tau^{ki}\right) - \frac{1}{2}\frac{\partial^2}{\partial x^k \partial x^l}\left(x^i x^j \tau^{kl}\right), \tag{2.53}$$

which can be substituted into Eq. 2.52. The only surviving term under the integral will be the $\tau_{00}$ term since the remaining terms contain spatial derivatives which will vanish on a boundary taken to be far from the source where spacetime is approximately Minkowski. Finally, we're left with

$$\bar{h}_{ij}(x^\mu) \simeq \frac{2G}{c^4 r}\frac{\partial^2}{\partial(x^0)^2} I_{ij}(x^0 - r/c) \tag{2.54}$$

where

$$I(x^0 - r/c) = \int d^3x' x'_i x'_j \tau_{00}(x^0 - r/c, \vec{x}') \tag{2.55}$$

is the quadrupole tensor. We can write our final solution even more succinctly if we denote derivatives with respect to $x^0$ with an $\dot{}\ \equiv \partial/\partial(x^0)$:

$$\bar{h}_{ij}(x^\mu) =\simeq \frac{2G}{c^4 r}\ddot{I}_{ij}(x^0 - r/c) \tag{2.56}$$

Defining the normal vector transverse to the plane of propagation $\hat{n}^i = x^i/r$ and its associated projection operator $P_{ij} = \delta_{ij} - \hat{n}_i \hat{n}_j$, we can project our solution onto the direction transverse to the plane of propagation and remove the trace of $I_{ij}$:

$$I_{ij}^{\mathrm{TT}} = P_{ik} I^{kl} P_{lj} - \frac{1}{2} P_{ij} P_{kl} I^{kl}. \tag{2.57}$$

The sourced transverse-traceless metric perturbation in the far-field limit is thus

$$h_{ij}^{\mathrm{TT}}(x^0) \simeq \frac{2G}{c^4 r}\ddot{I}_{ij}^{\mathrm{TT}}(x^0 - r/c). \tag{2.58}$$

### Compact Binary Waveform in Newtonian Limit

Gravitational waves can be produced by many astrophysical (and even cosmological) systems corresponding to different stress-energy tensors. The principle source of interest for this work are mergers of compact objects such as black holes and neutron stars, diagrammed in Fig. 2.2. In this case, the quadrupole tensor can be approximated as the quadrupole tensor for two point particles[4].

At low velocities, the rest frame reduced mass $\mu = \frac{m_1 m_2}{m_1+m_2} = \frac{m_1 m_2}{M}$, where $M \equiv m_1 + m_2$ is the total mass, dominates the quadrupole's mass dependence, meaning a Newtonian approximation for the early stages of the inspiral is sufficient. When the orbital plane of the binary is aligned with the $x^1 - x^2$ plane of a Cartesian coordinate system, the Newtonian quadrupole moment is

$$I_{ij} = \sum_{l=1}^{2} \mu(x_{il} x_{jl}), \tag{2.59}$$

where the sum goes only over the $x^1$ and $x^2$ coordinates since the quadrupole moment does not change with $x^3$. The four non-zero components are

$$I_{11} = \mu a^2 \left( \frac{1 + \cos(2\varphi)}{2} \right) \tag{2.60}$$

$$I_{12} = I_{21} = \mu a^2 \cos\varphi \sin\varphi \tag{2.61}$$

$$I_{22} = \mu a^2 \left( \frac{1 - \cos(2\varphi)}{2} \right), \tag{2.62}$$

where $a = r_1 + r_2$ is the orbital separation and $\varphi = \omega(t - D/c) \equiv \omega t_r$ is the phase in terms of the retarded time. Note since $r_i$ is natural notation for radial coordinates of the binary objects, we have changed the notation of the distance from the source to observer

---

[4] This is exactly true in the case of two uncharged, non-spinning black holes. Neutron stars on the other hand have non-negligible waveform corrections from tidal deformation of their matter content, but for demonstrative purposes this approximation will suffice.

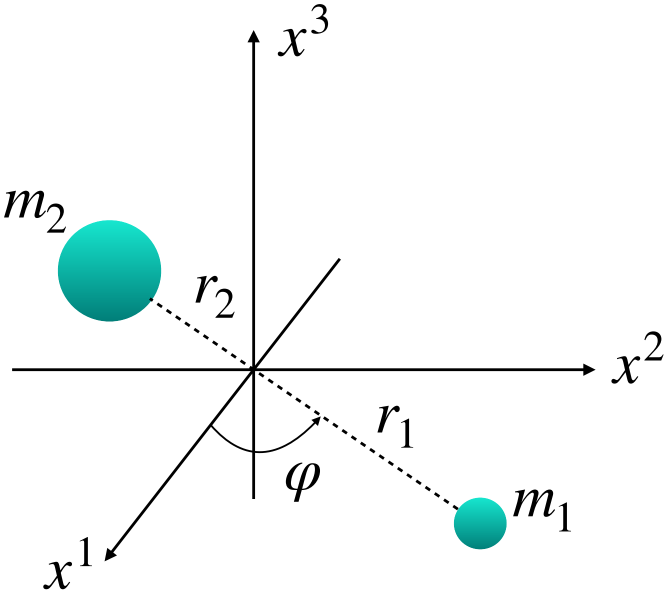

Figure 2.2: Coordinate system for a binary of compact objects with masses $m_1$ and $m_2$ whose orbital axis is aligned with the $x^1 - x^2$ plane. The quantities $r_1$ and $r_2$ represent the distances from the first and second component objects from the origin respectively. The orbital phase of the binary is given by $\varphi$.

$r \to D$. Substituting the compact binary quadrupole moment into Eq. 2.58 yields

$$\bar{h}_{ij} = -\frac{4G\omega^2\mu a^2}{c^4 D}\begin{pmatrix} \cos(2\varphi) & \sin(2\varphi) & 0 \\ \sin(2\varphi) & -\cos(2\varphi) & 0 \\ 0 & 0 & 0 \end{pmatrix} \tag{2.63}$$

$$= -\frac{4\mu}{c^2 D}\left(\frac{v}{c}\right)^2 \begin{pmatrix} \cos(2\varphi) & \sin(2\varphi(v,t)) & 0 \\ \sin(2\varphi) & -\cos(2\varphi(v,t)) & 0 \\ 0 & 0 & 0 \end{pmatrix}, \tag{2.64}$$

where we've recast in terms of $v = a\omega$. Additionally, we've made explicit the dependence of $\varphi$ on $v$ and $t$ since

$$\varphi = \omega t = \left(\frac{v}{c}\right)^3 \frac{c^3 t}{GM} \tag{2.65}$$

where $\omega = v^3/GM$ as a consequence of Kepler's third law $GM = a^3\omega^2$. The above waveform has no frequency evolution. However, we know that as the orbital separation between the two objects decreases, energy is lost in the form of gravitational waves. This energy loss is responsible for the frequency evolution that produces the familiar gravitational wave "chirp". The Newtonian energy and luminosity for a binary of point particles are given by [2]

$$E(v) = -\frac{1}{2}c^2 M\eta \left(\frac{v}{c}\right)^2 \tag{2.66}$$

$$L(v) = \frac{32}{5}\frac{c^5}{G}\eta^2 \left(\frac{v}{c}\right)^{10}, \tag{2.67}$$

where we've introduced the symmetric mass ratio $\eta = \mu/(m_1 + m_2)$. Leveraging the relationship between the radiation's luminosity and energy, $L = -dE/dt$, a differential equation governing the relationship between the linear velocity and time:

$$\frac{dt}{dv} = \frac{dt}{dE}\frac{dE}{dv} = -\frac{1}{L}\frac{dE}{dv}. \tag{2.68}$$

which also yields the analogous equation for $\varphi$,

$$\frac{d\varphi}{dv} = \frac{d\varphi}{dt}\frac{dt}{dv} = -\frac{v^3}{GM}\frac{1}{L}\frac{dE}{dv}, \tag{2.69}$$

where in the second equality we've invoked Eq. 2.68.

We now have total derivatives for $t(v)$ and $\varphi(v)$ in terms of known analytic expressions for $E$ and $L$ in terms of $v$. Thus, $t(v)$ and $\phi(v)$ can be obtained via direct integration of Eq. 2.68 and 2.69 from $v$ to the time and phase at coalescence,

$$t(v) = t_{\rm c} + \int_v^{v_{\rm c}} \frac{1}{L(v')}\frac{dE}{dv'}dv' \tag{2.70}$$

$$\varphi(v) = \varphi_{\rm c} + \int_v^{v_{\rm c}} \frac{v'^3}{GM}\frac{1}{L(v')}\frac{dE}{dv'}dv'. \tag{2.71}$$

Using Eqs. 2.66 and 2.67 for the energy and luminosity and integrating directly,

$$t = t_{\rm c} + \int_v^{v_{\rm c}} \left(-\frac{5}{32}\frac{GM}{\eta c^3}\frac{v'^{-9}}{c^{-8}}\right) dv \tag{2.72}$$

$$= t_{\rm c} + \frac{5}{256}\frac{GM}{\eta c^3}\left(\frac{v'}{c}\right)^{-8}\Bigg|_v^{v_{\rm c}} \tag{2.73}$$

$$= t_{\rm c} + \frac{5}{256}\frac{GM}{\eta c^3}\left[\left(\frac{v_{\rm c}}{c}\right)^{-8} - \left(\frac{v}{c}\right)^{-8}\right]. \tag{2.74}$$

taking $v_{\rm c} \to \infty^5$,

$$t(v) = t_{\rm c} - \frac{5}{256}\frac{GM}{\eta c^3}\left(\frac{v}{c}\right)^{-8}. \tag{2.75}$$

---

[5] This reflects the fact that this waveform only covers the *inspiral* phase during which the orbit is approximately circular. In reality, at the closure of the inspiral the binary enters the *merger* phase where the point-particle picture of the binary components breaks down after which the *ringdown* begins and continues until the post-merger remnant reaches spherical symmetry.

The integration for $\varphi(v)$ yields

$$\varphi = \varphi_{\mathrm{c}} + \int_{v}^{v_{\mathrm{c}}} \left( -\frac{5}{32}\frac{1}{\eta}\frac{v'^{-6}}{c^{-5}} \right) dv' \tag{2.76}$$

$$= \varphi_{\mathrm{c}} + \frac{1}{32\eta} \left( \frac{v'}{c} \right)^{-5} \Bigg|_{v}^{v_{\mathrm{c}}} \tag{2.77}$$

$$\varphi(v) = \varphi_{\mathrm{c}} - \frac{1}{32\eta} \left( \frac{v}{c} \right)^{-5} . \tag{2.78}$$

$t(v)$ is then inverted to obtain $v(t)$ and $\varphi(v(t)) = \varphi(t)$ after which both are substituted into Eq. 2.64. For convenience, we define the *chirp mass* $\mathcal{M} = \eta^{3/5} M$. The resulting plus and cross polarization waveforms can be read off from the components of Eq. 2.64:

$$h_{+}(t) = -\frac{G\mathcal{M}}{c^2 D} \left[ \frac{c^3(t_{\mathrm{c}} - t)}{5G\mathcal{M}} \right]^{-1/4} \cos \left( 2\varphi_{\mathrm{c}} - 2 \left[ \frac{c^3(t_{\mathrm{c}} - t)}{5G\mathcal{M}} \right]^{5/8} \right) \tag{2.79}$$

$$h_{\times}(t) = -\frac{G\mathcal{M}}{c^2 D} \left[ \frac{c^3(t_{\mathrm{c}} - t)}{5G\mathcal{M}} \right]^{-1/4} \sin \left( 2\varphi_{\mathrm{c}} - 2 \left[ \frac{c^3(t_{\mathrm{c}} - t)}{5G\mathcal{M}} \right]^{5/8} \right) . \tag{2.80}$$

There are several important features of Eqs. 2.79 and 2.80 to note. First, this is strictly a model of the *inspiral* phase of the waveform, where the binary is still in a stable semi-circular orbit. This model does not describe the remaining two phases: the *merger* phase when the two component objects begin to coalesce, and the *ringdown* phase which describes the transition of the remnant object from the merger to spherical symmetry. Additionally in both polarizations both the the amplitude and frequency of waveform increase as $t \to t_c$. When the signal, depicted in Fig. 2.3, is mapped to acoustic frequencies in the audible range, the rising frequency and amplitude over time can be likened to a bird's "chirp", giving the signal its signature nickname. Lastly, the two polarizations have a constant one quarter cycle phase difference for the entirety of the signal.

For many of the analyses performed in this work, it is convenient to express the CBC

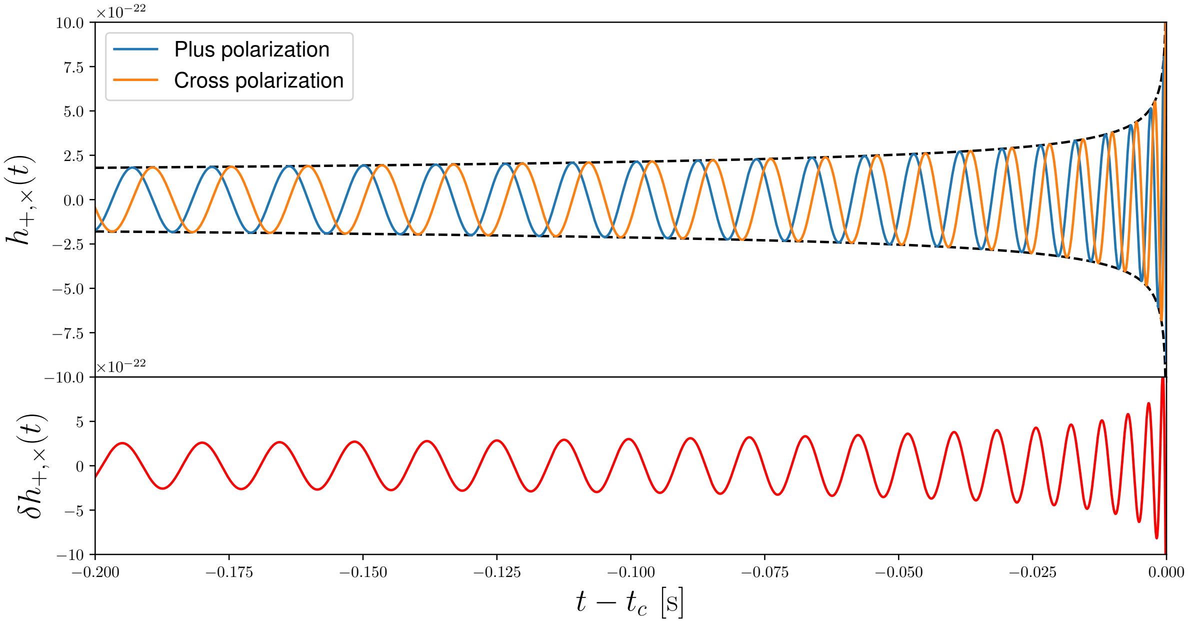

Figure 2.3: An example of a Newtonian-approximated gravitational-wave strain in the time domain decomposed onto "plus" and "cross" polarizations for an equal-mass 5 $\mathrm{M}_\odot$ binary at a distance of 500 Mpc. The difference between the two polarization strains $\delta h_{+,\times}(t) \equiv h_+(t) - h_\times(t)$ is shown below.

waveform in the frequency domain:

$$\tilde{h}(f) = \sqrt{\frac{5\pi}{24}} \frac{G^2\mathcal{M}^2}{c^5 D} \left[\frac{\pi \mathcal{M} G f}{c^3}\right]^{-7/6} \exp[-i\psi(f)], \tag{2.81}$$

where the phase is

$$\psi(f) = 2\pi f t_\mathrm{c} - 2\varphi_\mathrm{c} - \pi/4 + \frac{3}{128} \left[\frac{\pi \mathcal{M} G f}{c^3}\right]^{-5/3}. \tag{2.82}$$

It should be noted that the frequency $f = f_\mathrm{GW} = 2 f_\mathrm{orbital}$ is the gravitational waveform frequency which is twice the orbital frequency of the binary.

### Newtonian limitations and modern waveforms

The Newtonian approximate models discussed thus far act well as toy models for the radiation produced by compact binaries, but require several improvements before considered sufficient waveform models. These improvements fall into three categories:

| | | |
|---|---|---|
| Masses | $m_1$, $m_2$ | Intrinsic |
| Spins | $\chi_{1,x}$, $\chi_{1,y}$, $\chi_{1,z}$,<br>$\chi_{2,x}$, $\chi_{2,y}$, $\chi_{2,z}$ | |
| Tidal effects | $\lambda_1$, $\lambda_2$ | |
| Sky position | $\delta$, $\alpha$ | Extrinsic |
| Orientation | $\iota$, $\psi$ | |
| Distance | $D$ | |
| Phase and Time Offset | $\varphi_0$, $t_0$ | |

Figure 2.4: Many parameters affect the shape and evolution of a gravitational wave. The parameters can be intrinsic properties of the system or extrinsic, resulting from sky location, distance to the source, etc.

1. The signal derived here is dependent on four model parameters: the chirp mass $\mathcal{M}$, the distance to the source $D$, the coalescence time $t_c$, and the phase at coalescence $\varphi_c$. In actuality, the waveform is dependent on a much larger parameter space, including additional properties intrinsic to the system like the binary components' spins, eccentricity of the orbit, and sometimes others.

2. Eqs. 2.66 and 2.67 are the Newtonian expressions for the binary system's energy and luminosity, which break down at large $v/c$.

3. The inspiral phase of the waveform, though the longest in most cases[6], does not describe the entire signal. The remaining two phases, the merger and ringdown, cannot be accurately modeled with perturbative methods.

---

[6] For intermediate-mass black hole (IMBH) binaries with component masses $10^2 - 10^4 \mathrm{M}_\odot$, the merger occurs at very low frequencies meaning the inspiral phase has very few cycles in the detector band. Therefore it's particularly important to have accurate merger and ringdown models for this class of sources.

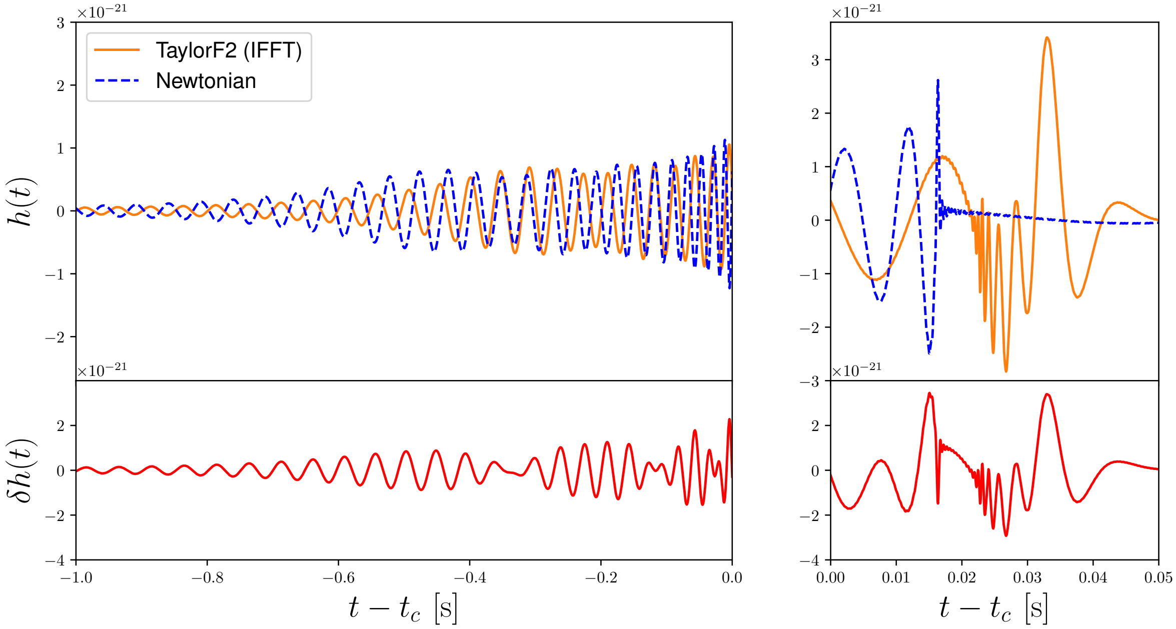

(a) Newtonian inspiral and phenomenological TaylorF2 waveform models as a function of time to coalescence.

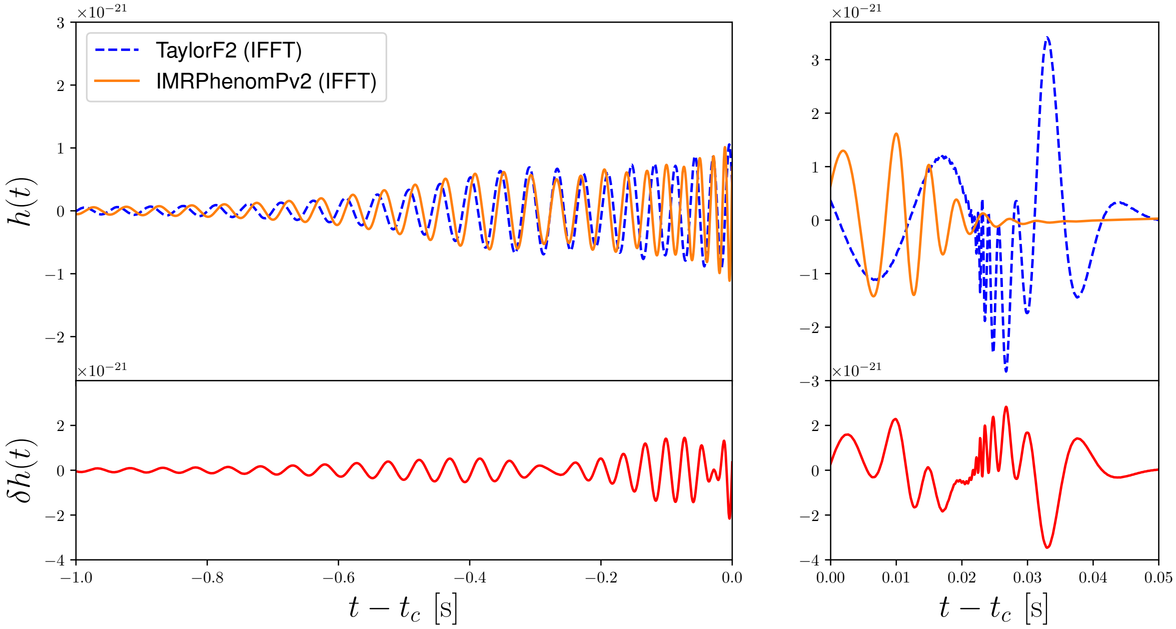

(b) TaylorF2 and phenomenological inspiral-merger-ringdown waveform models (IMRPhenomPv2) as a function of time to coalescence.

Figure 2.5: Comparison between detector response of phenomenological waveform IMRPhenomPv2, Newtonian-approximate, and TaylorF2 waveforms. Figures on the left show the inspiral phase up until coalescence time, while figures on the right show the merger and ringdown phases on a smaller timescale. The Newtonian amplitude in eqs. 2.79 and 2.80 goes to infinity at high $f_{\rm GW}$, causing the Newtonian waveform to break down at high $v/c$. Phenomenological waveforms such as IMRPhenomPv2 combine post-Newtonian inspirals with numerical-relativity calibrated merger and ringdown models.

An ideal resolution to the second item would be to solve the EFEs numerically without assuming the perturbations to the metric are small. This is both computationally expensive and unnecessary for describing signals observed so far from the source. A more appropriate solution is to add higher order corrections to the Newtonian expressions for energy and luminosity. Formally, the expressions for energy and luminosity distance become

$$E(x) = -\frac{1}{2}c^2 M\eta x[1 + \delta E_{\mathrm{PP}}] \tag{2.83}$$

$$L(x) = \frac{32}{5}\frac{c^5}{G}\eta^2 x^5[1 + \delta L_{\mathrm{PP}}]. \tag{2.84}$$

where, expanded in $x = (\pi G M f_{\mathrm{gw}}/c^3)^{2/3} = (v/c)^2$, the *post-Newtonian* (PN) corrections [3–5] that lead to the waveform improvements [6] are

$$\begin{aligned}\delta E_{\mathrm{PP}} = &-\left(\frac{3}{4} + \frac{1}{12}\eta\right)x - \left(\frac{27}{8} - \frac{19}{8}\eta + \frac{1}{24}\eta^2\right)x^2 \\ &- \left(\frac{675}{64} - \left(\frac{34445}{576} - \frac{205}{96}\pi^2\right)\eta + \frac{155}{96}\eta^2 + \frac{35}{5184}\eta^3\right)x^3\end{aligned} \tag{2.85}$$

$$\begin{aligned}\delta L_{\mathrm{PP}} = &-\left(\frac{1247}{336} + \frac{35}{12}\eta\right)x + 4\pi x^{3/2} \\ &- \left(\frac{44711}{9072} - \frac{9271}{504}\eta - \frac{65}{18}\eta^2\right)x^2 - \left(\frac{8191}{672} + \frac{583}{24}\eta\right)\pi x^{5/2} \\ &+ \left(\frac{6643739519}{69854400} + \frac{16}{3}\pi^2 - \frac{1712}{105}e - \frac{856}{105}\ln(16x)\right. \\ &\left. + \left(\frac{41}{48}\pi^2 - \frac{134543}{7776}\right)\eta - \frac{94403}{3024}\eta^2 - \frac{775}{324}\eta^3\right)x^3 \\ &- \left(\frac{16285}{504} - \frac{214745}{1728}\eta - \frac{193385}{3024}\eta^2\right)\pi x^{7/2}.\end{aligned} \tag{2.86}$$

The corrections here are of order 7/2, referred to as “3.5 PN”. Fig. 2.5a displays an example of a typical GW observatory’s detector response under the Newtonian approximation and a member of the post-Newtonian waveform family, `TaylorF2` [7].

The third item is significantly more tricky to tackle. One approach is to recast the system into an Effective One Body (EOB) formulation [8–11], which still require numerical integration of the EOB equations of motion, but are significantly simpler relative to the full EFEs. Ultimately, we would like to use these models in conjunction with Bayesian Markov-chain Monte Carlo (MCMC) and nested sampling algorithms to infer the source parameters of GW observations. This requires $\mathcal{O}(10^6)$ waveform generations, and thus EOB waveforms are sometime computationally disfavored.

Another, more resource-conservative solution involves combining post-Newtonian inspiral models and NR-calibrated phenomenological models of the merger and ringdown phases, known as "IMRPhenom" models [12–15]. This provides many of the benefits of the EOB waveform family while maintaining a waveform computation time suitable for parameter estimation. Fig. 2.5b shows a comparison between the `IMRPhenomPv2` and `TaylorF2` waveform models for a signal with the same model parameters as 2.5a.

# Chapter 3

# Gravitational Wave Astronomy

Looking at Fig. 2.5a, 2.5b, the magnitude of the GW strain is $\mathcal{O}(h) = 10^{-22}$. As we'll see later, strain measures the distortion of lengths relative to their undisturbed value. As an example, a gravitational wave with strain $h \sim 10^{-22}$ would alter the distance between Earth and our nearest exosolar star, Alpha Centauri (undisturbed  4 ly) by $4\mu$m–approximately the size of a typical red blood cell. With this in mind, it would be understandable to conclude the direct detection of GWs is an impossibility and indeed even Einstein himself resigned the prospect. Lo and behold, as of 2023, time series strain data is publicly available for more than 90 confident GW observations [16–18]. In this chapter, we'll cover the anatomy of the instruments that made these detections possible and practical limitations that will serve as crucial context for analysis of GW strain data.

## 3.1 The Michelson Interferometer

The objective of GW observatories is not only to identify when GWs have passed through them, but also to characterize the observed signal so that its source properties may be inferred. And while the source waveform models we have cover a sufficiently large

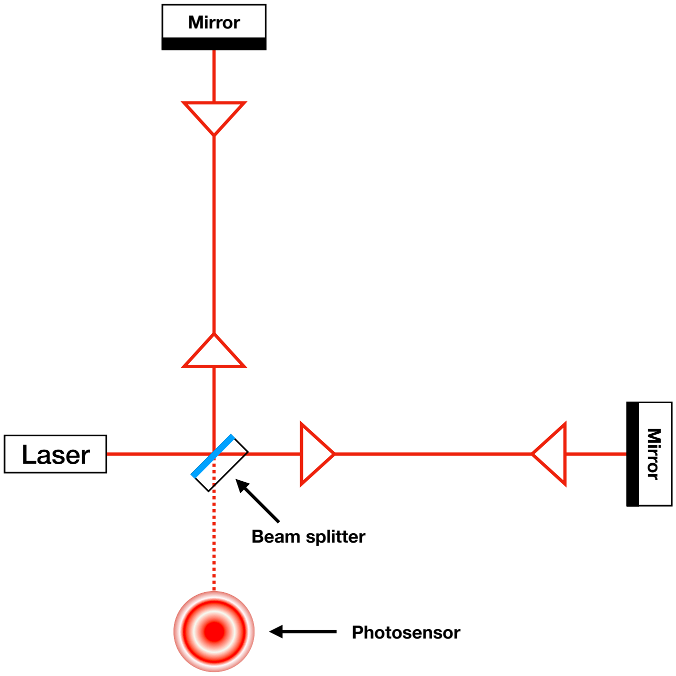

Figure 3.1: Length distortions in the arms of a Michelson interferometer result in optical path length differences that produce interference patterns captured by a photosensor.

parameter space of source characteristics[1], there are additional observer effects that will alter the signal received on Earth. GW observatories must therefore be designed to resolve GW signals from anywhere in the sky and for any relative orientation to the source binary.

Michelson interferometers satisfy these requirements by mimicking the ring of test particles shown in Fig. 2.1 through interference patterns of light [19]. These instruments are configured in an “L” shape (shown in Fig. 3.1) with equal-length arms such that any relative length change between the arms produces an interference pattern which depends on the magnitude of the length distortions. Schematically, they operate as follows:

1. Highly collimated light is emitted from a laser and shone onto a beam-splitter that

---

[1] There still exist some CBC configurations for which our most sophisticated waveform models break-down. Many of these cases–extreme mass ratios, high-spin and precessing CBCs–are the subject of current research.

divides into two orthogonal beams in a 50-50 intensity split.

2. Each beam travels down its respective arm at the end of which a mirror is situated perpendicular to the direction of propagation of the light.

3. After reflecting off of the mirror, each beam travels back towards the beam splitter.

4. As with their outgoing encounter with the beamsplitter, 1/2 of each beam (now 1/4 of the initial intensity) is reflected, while the other half is transmitted resulting in 1/2 of the initial intensity returning to laser and the other half traveling perpendicular and arriving at a photosensor.

The relative phase of returning beams depends on the difference between their travel distance. Thus for an undisturbed interferometer with equal-length arms, the two beams will be exactly in-phase resulting in the maximum intensity at the detector. Any non-conformal distortions in the physical lengths of the arms will therefore result in a reduction in intensity at the photosensor. Specifically the change in the intensity of light at the detector will be the difference in changes from the proper length of each arm $\Delta l = \Delta l_1 - \Delta l_2$.

Consider an interferometer with one arm aligned with the $x^1$ axis and the other aligned with the $x^2$ axis. A plus-polarized gravitational wave propagating in the $x^3$ direction has the associated line element

$$g_{\mu\nu} dx^\mu dx^\nu = -c^2 dt^2 + \left[1 + h_{11}(x^3, t)\right] d(x^1)^2 + \left[1 - h_{11}(x^3, t)\right] d(x^2)^2 + d(x^3)^2.$$

Integrating the line element gives the spacetime interval between two spacetime events:

$$l = \int \sqrt{g_{\mu\nu} dx^{\mu} dx^{\nu}}.$$

The proper distance between the $x^1$ mirror located at $l_0$ when unperturbed and the origin is

$$\begin{aligned} l_1 &= \int_0^{l_0} \sqrt{1 + h_{11}(x^3, t)} dx^1 \\ &= \sqrt{1 + h_{11}(x^3, t)} \int_0^{l_0} dx^1 \\ l_1 &= l_0 \sqrt{1 + h_{11}(x^3, t)}. \end{aligned}$$

Similarly, the proper length of the $x^2$-aligned detector arm is

$$l_2 = \frac{l_0}{2} \sqrt{1 - h_{11}(z, t)}.$$

Given $h \ll 1$, the changes in proper length can be estimated as

$$\begin{aligned} \Delta l_1 &= l_0 \sqrt{1 + h_{11}(x^3, t)} - l_0 \\ &\approx l_0 \left(1 + \frac{1}{2} h_{11}(x^3, t)\right) - l_0 \\ &= \frac{l_0}{2} h_{11}(x^3, t) \\ \Delta l_2 &= l_0 \sqrt{1 - h_{11}(x^3, t)} - l_0 \\ &\approx l_0 \left(1 - \frac{1}{2} h_{11}(x^3, t)\right) - l_0 \\ &= -\frac{l_0}{2} h_{11}(x^3, t) \end{aligned}$$

As discussed above, the relative phase difference at the photosensor is given by $\Delta l / l_0$

which in this case is

$$\begin{aligned}\frac{\Delta l}{l_0} &= \frac{1}{l_0}\left(\frac{l_0}{2}h_{11}(x^3,t) + \frac{l_0}{2}h_{11}(x^3,t)\right) \\ &= h_{11}(x^3,t)\end{aligned}$$

Here we've shown that for a plus-polarized wave aligned with the axes of a Michelson interferometer, the intensity change measured at the photodetector is precisely the strain of the GW signal. Later on, we will briefly discuss how to generalize the detector response to include effects due to extrinsic parameters such as sky location, inclination angle to the source binary, and generic polarization angle.

### 3.1.1 Detector sensitivity

The global GW observatory network consists of three ground-based Michelson interferometers, shown in Fig. 3.2. The two LIGO detectors, LIGO Livingston and LIGO Hanford, each have 4 km-long arms while Virgo has 3 km-long arms. The smallest detectable length change in these detectors would be of the order of the laser light. For an infrared laser of $\lambda = 10^{-6}$m in a detector with $\mathcal{O}(10^3\text{m})$ arm lengths would be sensitive to a strain of

$$\frac{\Delta l}{l} \sim \frac{10^{-6}\text{m}}{10^{3}\text{m}} \sim 10^{-9} \equiv h.$$

As we found in the previous chapter, for GWs produced in distant mergers of compact objects, the signal strain when it reaches Earth will be $\mathcal{O}(10^{-22})$, many orders of magnitude smaller than the estimated sensitivity for a detector with kilometer-long arms. Modern GW observatories can improve their sensitivity significantly while avoiding the practical limitations of increasing the physical arm lengths of the detector by increasing its *effective* arm length. This is done by inserting reflective cavities between the beamsplitter and mirrors of each arm which trap the light as it travels back and forth in the chamber. These Fabry-Perot cavities radically increase the effective arm length of the detector and thus its sensitivity. The only limitation arises when the effective arm length is comparable to the GW wavelength, in which case the evolution of the GW signal becomes non-negligible over the course of a photon's trip from the laser, through cavity, and arrival at the photosensor. This improvement achieves a strain sensitivity of $\sim 10^{-12}$, which is still several orders of magnitude away from the required sensitivity. In order to further improve sensitivity, a purely wave-picture of light does not suffice. Specifically, shot noise becomes an important consideration. The arrival rate of photons at the photosensor follows a Poisson distribution meaning the observed number of photons will fluctuate with time as $\Delta N_{\text{photons}} \sim N_{\text{photons}}^{1/2}$. In order to distinguish between changes in the light caused by natural Poisson fluctuations and changes induced by GWs, we need the optical path length to change by

$$\Delta l \sim \Delta N_{\text{photons}} \lambda_{\text{laser}}.$$

In order to resolve individual cycles of the GW signal, the maximum amount of time allowed for photon collection is $1/f_{\text{GW}}$. The number of photons collected on that timescale is

$$\begin{aligned} N_{\text{photons}} = E_\gamma / f_{\text{GW}} &\sim \frac{P_{\text{laser}} \lambda_{\text{laser}}}{h c f_{\text{GW}}} \\ &= 5.4 \times 10^{16}, \end{aligned}$$

for a laser with power $P_{\text{laser}}$. With $P_{\text{laser}} = 4$ W, $\lambda_{\text{laser}} = 808$ nm. The smallest optical path detectable is therefore

$$\begin{aligned} h \equiv \frac{\Delta l}{l_{\text{eff}}} &= N_{\text{photons}}^{-1/2} \frac{\lambda_{\text{laser}}}{\lambda_{\text{GW}}} \\ &= 3.5 \times 10^{-21}, \end{aligned}$$

(a) LIGO Livingston, Livingston, LA, USA

(b) LIGO Hanford, Hanford, WA, USA

(c) Virgo, Santo Stefano a Macerata, Cascina, Italy

Figure 3.2: The three instruments comprising the LVC GW observatory network. Each observatory has two perpendicular arms 4km in length with the exception of Virgo which has 3km-long arms. Image credit: Refs. [23–25]

which is nearly the expected strain magnitude of a CBC waveform. The remaining sensitivity improvements involve advanced techniques such as signal recycling [20, 21] and quantum squeezing [22], but extend beyond the necessary context for this thesis.

### 3.1.2 Detector response

GWs passing through a Michelson interferometer will in general not be propagating perfectly perpendicular to the detector axis. Additionally, the instrument is not immune from other effects that can cause changes in the photosensor interference patter, any and all of which we categorize as noise. Assuming a single signal present, the detector response is therefore a combination of GW strain data masked by orientation effects and time-varying noise,

$$d(t) = F_+(\alpha,\delta,\psi)\left(\frac{1+\cos^2\iota}{2}\right)h_+(t;\vec{\theta}) + F_\times(\alpha,\delta,\psi)(\cos\iota)h_\times(t;\vec{\theta}) + n(t), \tag{3.1}$$

where $h_{\mathrm{GW}}(t;\vec{\theta})$ is the strain contribution from the gravitational wave, $n(t)$ is the noise contaminating the strain data, $\iota$ is the inclination angle between the orbital plane of the binary and the observer, and the antenna function [26], $F_{\{+,\times\}}$,

$$F_+(\alpha,\delta,\psi) = \frac{1}{2}(1+\sin\delta)\cos 2\alpha\cos 2\psi - \sin\delta\sin 2\alpha\sin 2\psi \tag{3.2}$$

$$F_+(\alpha,\delta,\psi) = \frac{1}{2}(1+\sin\delta)\cos 2\alpha\sin 2\psi + \sin\delta\sin 2\alpha\cos 2\psi, \tag{3.3}$$

encode observer effects due to the source's sky location and relative orientation to the detector for each polarization. The right ascension, $\alpha$, and declination, $\delta$, parameterize the celestial sphere, and $\psi$ is the polarization angle counter-clockwise about the direction of propagation. The dependence of the antenna function on the sky location parameters for both plus- and cross-polarized GWs is shown in Fig. 3.3.

The sensitivity of a GW is empirically quantified by the power spectral density (PSD) of the detector data in the absence of a gravitational wave, i.e. the PSD of the noise, $S_n(f)$:

$$S_n(|f|)\frac{1}{2}\delta(f-f') = \langle \tilde{n}^*(f')\tilde{n}(f)\rangle, \tag{3.4}$$

where $\tilde{n}(f)$ are the Fourier modes of the time-series noise and $\langle\cdot\rangle$ denotes an ensemble average. The amplitude spectral density (ASD) $ASD(f) = \sqrt{S_n(f)}$ is often used for direct comparison of detector noise level and GW strain amplitude.

Fig. 3.4 shows the ASDs of LIGO Livingston, LIGO Hanford, and Virgo estimated from strain data surrounding GW200322[2], the last confident event detected in the LVC's

---

[2] Strain data used to estimate the detector PSDs can be found at `https://gwosc.org/eventapi/html/GWTC-3-confident/GW200322_091133/v1`

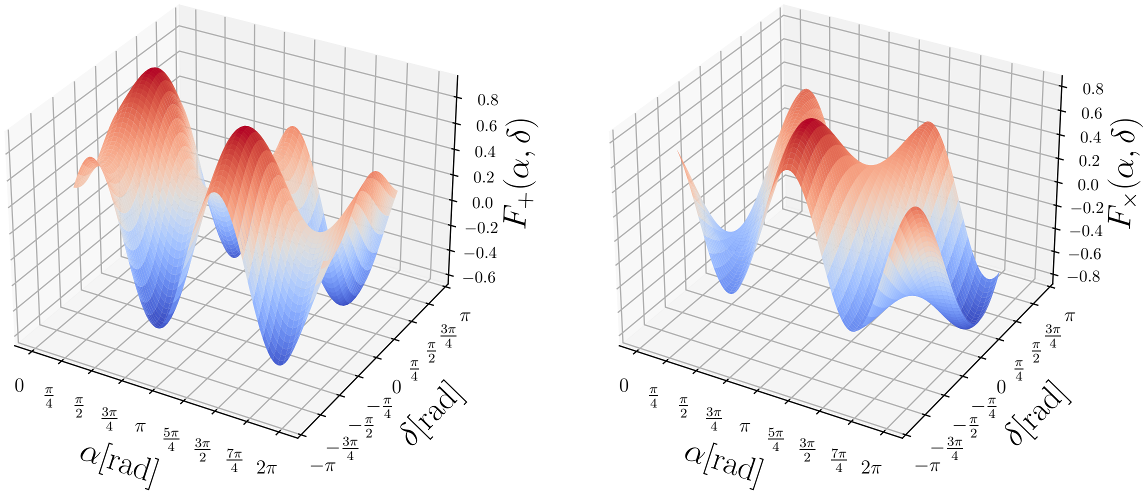

Figure 3.3: Dependence of the antenna functions on right ascension $\alpha$ and declination $\delta$ for $\psi = 0$.

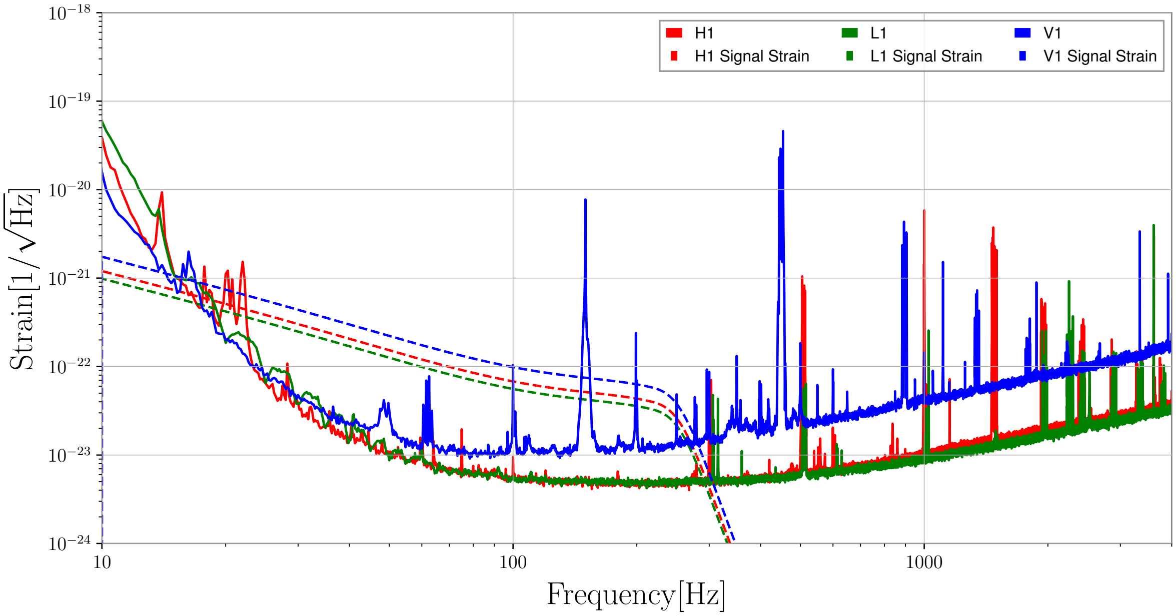

Figure 3.4: Amplitude spectral densities from L1, H1, and V1 estimated from a 1000s data segment around GW200322, the most recent public event from O3b. Seismic activity dominates the noise ASDs for all three detectors at frequencies below 10 Hz, while Brownian motion in the mirror suspension lines and shot noise dominate at mid-to-high range frequencies (100 Hz - 10 kHz). Dashed lines are detector responses for a signal with $\mathcal{M}_{\mathrm{chirp}} \approx 31M_\odot$ at $d_L \approx 45\mathrm{Mpc}$. A CBC with such a chirp mass is unrealistic at such a close distance, and is displayed for comparison and visual clarity.

most recent observing run, O3b. Below 10 Hz, the noise ASD is heavily dominated by seismic activity such as nearby pedestrian activity and even distant earthquakes. This noise wall effectively defines the in-band signal time for most GW targets and is a fundamental limitation of all ground-based GW observatories. Despite the quadruple pendulum systems suspending each of the end station mirrors, Brownian motion in the suspension wires still dominates the mid-to-high-frequency range (100 Hz to 10 kHz), as well as shot noise limitations discussed earlier. Additionally, the suspension system harmonics introduce spectral peaks in the ASD, though the seismic noise reduction they provide is well worth the trade-off.

# Chapter 4

# Parameter Estimation

## 4.1 Bayesian Statistics

Estimation of GW source parameters is not conducive to frequentist methods. Typically, repeated measurements of a randomly distributed variable can be used to reconstruct its probability distribution from which statements can be made about the likelihood of the variable's true value. In the case of GW observations, only one signal is produced by each binary merger and therefore only one measurement can be made by each detector per one source.

Bayesian statistics recasts the notion of probability as a degree of belief rather than an expected outcome from many repeated experiments. Bayes' theorem,

$$P(A|B) = \frac{P(B|A)P(A)}{P(B)}, \tag{4.1}$$

which is derived purely from classical conditional probability, relates the *posterior* probability $P(A|B)$ to the product of the *likelihood* and *prior* $P(B|A)P(A)$ divided by the *evidence* $P(B)$. The quantities in Eq. 4.1 can be promoted to apply to probability densities as well. This is particularly applicable to GW parameter estimation. Given some strain data $d(t)$ containing a GW signal, we're interested in the joint posterior density distribution (PDF) $p(\vec{\theta}|d,m)$ on the parameters $\vec{\theta}$ describing model $m$. Applying Eq. 4.1, the PDF on $\vec{\theta}$ can be computed from

$$p(\vec{\theta}|d,m) = \frac{p(d|\vec{\theta},m)p(\vec{\theta}|m)}{\mathcal{Z}}, \tag{4.2}$$

where again $p(d|\vec{\theta},m)$ is the likelihood distribution, $p(\vec{\theta}|m)$ is the prior distribution, and the denominator

$$\mathcal{Z} \equiv p(d|m) = \int p(d|\vec{\theta},m)p(\vec{\theta}|m)d\vec{\theta} \tag{4.3}$$

is the Bayesian evidence. The likelihood function quantifies how well a given set of model parameters matches the signal data. A robust choice of likelihood function for GW analysis [27, 28] is proportional to the integrated square of the difference between the frequency domain data and model weighted by the PSD of the noise,

$$p(d|\vec{\theta},m) \equiv \mathcal{L} \propto \exp\left[-2\int_0^\infty \frac{|d(f)-\tilde{h}(f;\vec{\theta})|^2}{S_n(f)}df\right], \tag{4.4}$$

where $S_n(f)$ is the one-sided power spectral density of the noise. The likelihood has a maximum when $d(f)-\tilde{h}(f;\vec{\theta})=0$, i.e. when the model exactly matches the data for a set of specific set of parameters.

The posterior distribution is the $n$-dimensional joint probability density function on the entire model parameter space, where $n = \dim(\vec{\theta})$. It's often useful to look at the 1-dimensional marginal PDFs on individual parameters, accomplished by integrating out all other parameters:

$$p(\theta_i|d,m) = \int p(\vec{\theta}|d,m)\left(\prod_{k\neq i} d\theta_k\right). \tag{4.5}$$

The evidence, which is calculated by integration of the posterior over the entire parameter space, contains no dependence on the model parameters but changes depending on the model used. This makes it desirable for model selection since it represents the overall probability that the data $d$ is described by the chosen model $m$. Therefore, a useful way to evaluate how well two models describe the data relative to one another is to compare their evidences:

$$\mathcal{B} \equiv \frac{\int p(d|\vec{\theta}_1, m_1) p(\vec{\theta}_1|m_1) d\vec{\theta}_1}{\int p(d|\vec{\theta}_2, m_2) p(\vec{\theta}_2|m_2) d\vec{\theta}_2} = \frac{\mathcal{Z}_1}{\mathcal{Z}_2}, \tag{4.6}$$

known as the *Bayes factor*.

Direct computation of the posterior from eq. 4.1 is computationally intractable when estimating the full GW model parameter space. As a conservative estimate, suppose we computed the posterior for just 10 samples $\{\vec{\theta}_1, \ldots, \vec{\theta}_{10}\}$ where each sample $\vec{\theta}_i$ is $n$-dimensional. After computing the prior and likelihood for the sample points, computation of the evidence would require numerical integration over $10^n$ points, where $n$ is between 12 and 15 for most GW models. Faithful reconstruction of the posterior requires far more than 10 sample points, and thus direct computation becomes prohibitively resource-intensive very quickly. In the following sections, we'll discuss two independent methods, Markov-chain Monte Carlo (MCMC) and nested sampling (NS), which while still computationally expensive in many cases, makes computation of the posterior and evidence distributions feasible.

## 4.2 Markov-chain Monte Carlo Methods

MCMC methods [29–34] offer a way to draw samples from the posterior distribution without requiring computation of the evidence. This is accomplished by generating a set of prior points sometimes known as "walkers" that traverse the posterior distribution. The direction each walker takes is determined by the relative improvement in posterior between adjacent points in the Markov-chain. The core loop of the routine is summarized in Fig. 4.1 and can be described as follows:

1. A starting sample $\vec{\theta}_0$ is drawn from the prior distribution.

2. As defined in eq. 4.1, the posterior, $p(\vec{\theta}_0|d, m)$ for the resulting waveform is calculated.

3. A new sample $\vec{\theta}_1$ is proposed by drawing new parameters from a chosen distribution $q(\vec{\theta}|\vec{\theta}_0)$ centered around the previous sample $\vec{\theta}_0$

4. The posterior $p(\vec{\theta}_1|d, m)$ is calculated for the new sample.

5. The Metropolis-Hastings (MH) ratio [35, 36] given by

$$\frac{p(\vec{\theta}_{i+1}|d, m)}{p(\vec{\theta}_i|d, m)} = \frac{p(d|\vec{\theta}_{i+1}, m)p(\vec{\theta}_{i+1}|m)}{p(d|\vec{\theta}_i, m)p(\vec{\theta}_i|m)} \frac{q(\vec{\theta}_i|\vec{\theta}_{i+1})}{q(\vec{\theta}_{i+1}|\vec{\theta}_i)}, \tag{4.7}$$

   is calculated between the posterior values for points $\vec{\theta}_0$ and $\vec{\theta}_1$ (i=0), weighted by the ratio of jump proposal probabilities which becomes important when the chosen jump proposals are asymmetric.

6. The value of the MH ratio is compared to a random number $r$ between 0 and 1. If greater than $r$, the point is "accepted" and added to the Markov chain. Otherwise, the point is rejected and the algorithm restarts from step 3.

Steps 3-6 repeat until a termination condition is reached. As there is no natural stopping condition for the MCMC algorithm, typically termination occurs when the total number of accepted points reaches a user-defined value.

Note that comparison of Eq. 6 to a random number implies that points with *lower* posterior values will sometimes be accepted as well. This may seem unintuitive at first, but upon closer inspection this is a crucial choice. If our initial sample is chosen near a maximum, only accepting points of greater posterior value would trend towards the maximum posterior sample after which point no new samples could be accepted. Since our objective is to produce a representative array of posterior samples, sometimes allowing lower posterior-valued points to be accepted ensures the sampler can continue producing posterior samples even once it's found the maximum. Moreover, if the posterior distribution sampled is multi-modal, only accepting points of higher posterior may not even yield the true maximum posterior point and instead stall on a local maximum. Many implementations of MCMC samplers also dynamically adjust the scale of the proposal distribution to allow for more distant points to be proposed. Adjustments typically widen the distribution upon sample acceptance and narrow upon rejection. This is a fairly tricky tuning problem as too narrow a proposal distribution can result in high correlation between samples while too wide a distribution results in a very low acceptance rate, increasing simulation times. All of these subtleties prove crucial to efficiently producing a representative set of posterior samples.

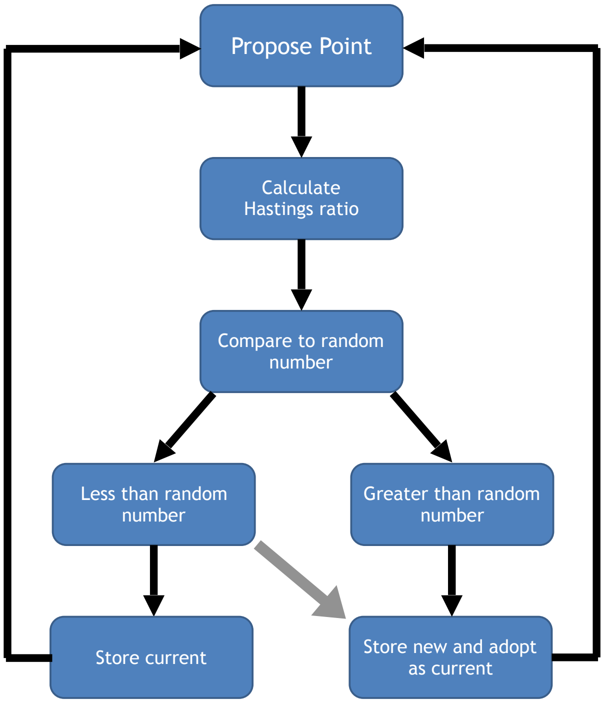

Figure 4.1: Diagrammatic representation of Bayesian MCMC algorithm.

### 4.2.1 Parallel Tempering

The inherent sequential nature of Markov-chains makes a MCMC routines a poor candidate for parallelization. However, a modification known as parallel tempering [37], can be used to generate more complete reconstructed posteriors and is naturally conducive to parallelization. Parallel tempering introduces the notion of the “temperature” of the

MCMC chain, which modifies the weighting of the likelihood function in Eq. 6,

$$p_T(\vec{\theta}|d,m) \propto p(\vec{\theta},m)p(d|\vec{\theta},m)^{1/T},$$

where $T$ is the aforementioned temperature. For $T = 1$, the true posterior is sampled while higher temperature values sample distributions that approach the prior. While an individual MCMC with $T \neq 1$ will not produce valid samples for the true posterior, the value of tempered MCMCs arises when many chains with different temperatures are evolved simultaneously and allowed to communicate. Specifically, adjacent chains occasionally swap current parameter locations at a rate of

$$r_{\mathrm{swap}} = \min\left[1, \left(\frac{\mathcal{L}(\vec{\theta}_i)}{\mathcal{L}(\vec{\theta}_j)}\right)^{\frac{1}{T_i}-\frac{1}{T_j}}\right]. \tag{4.8}$$

for $T_i < T_j$. This ultimately allows the $T = 1$ chain to occasionally swap places with chains that have identified high-posterior regions. In the absence of parallel tempering, the scale of the jump proposal would need to be significantly widened to sufficiently sample the posterior, which comes at the heavy cost of a significant reduction in sample acceptance ratio which drastically increases the amount of time required to achieve a given number of posterior samples.

As direct integration of the posterior is extremely computationally inefficient [38], the most widely used method for estimating the evidence from MCMC posterior samples, thermodynamic integration [39], relies on samples from higher temperature chains. However, nested sampling routines, discussed in the following section, designed to compute the evidence can also be used to produce posterior samples and thus are often preferred when the Bayesian evidence is desired in addition to posterior samples.

## 4.3 Nested Sampling

Nested sampling algorithms [40, 41] are another class of techniques aimed at sampling Bayesian probability density functions. MCMC methods sample the Bayesian posterior directly and use additional techniques, such as thermodynamic integration, to integrate over the joint posterior leaving the evidence. Nested sampling routines, on the other hand, specialize in computing the Bayesian evidence, from which the posterior can be sampled. The evidence is the integral of the posterior over $\Omega_\theta$, the entire parameter domain,

$$\mathcal{Z} = \int_{\Omega_\theta} p(\vec{\theta}|d, m) d\vec{\theta} = \int_{\Omega_\theta} p(d|\vec{\theta}, m) p(\vec{\theta}|m) d\vec{\theta}, \tag{4.9}$$

where we've invoked Bayes' theorem in the second equality. For the rest of this derivation, we'll suppress the dependence on the model $m$ for conciseness. Rather than integrating the product of the likelihood and prior, both functions of the parameters, the above expression can be recast into an integral over prior volumes defined by a region which is in turn defined by a likelihood constraint,

$$\mathcal{Z} = \int_{\Omega_\theta} p(d|\vec{\theta}, m) p(\vec{\theta}|m) d\vec{\theta} = \int_0^1 \mathcal{L}(X) dX, \tag{4.10}$$

where $X$ is a prior volume defined by the region $\Omega_\lambda = \{\vec{\theta} : \mathcal{L}(\vec{\theta}) \geq \lambda\}$,

$$X = \int_{\Omega_\lambda} p(\vec{\theta}) d\vec{\theta}. \tag{4.11}$$

Since the prior distribution is normalized, $X = 1$ represents integration over the entire prior space, which therefore corresponds to $\lambda = 0$, since all points in parameter space will satisfy $\mathcal{L}(\vec{\theta}) \geq 0$. Likewise, when $X = 0$ the infinitesimally small prior volume which is achieved when $\lambda \to \infty$, which implies the empty set of points $\{\vec{\theta} \geq \infty\}$. Thus Eq. 4.10 can be interpreted as a likelihood integration over smaller and smaller prior volumes defined by larger and larger values of $\lambda$.

### 4.3.1 Generation of samples

The core challenge of NS algorithms is drawing samples from the prior volume subject to the likelihood restriction $\Omega_\lambda = \{\vec{\theta} : \mathcal{L}(\vec{\theta}) \geq \lambda\}$. Simply drawing from the full prior space and rejecting points not satisfying this criterion is extremely inefficient. Thus, a method for producing samples already satisfying this requirement is highly preferred. While many exist, we will focus on the approach adopted in the `dynesty` [42] implementation of NS since this is the sampler used to perform all of the NS routines in this work. In the `dynesty` approach the constrained prior

$$p_\lambda(\vec{\theta}) = \begin{cases} p(\vec{\theta})/X(\lambda) & \mathcal{L}(\vec{\theta}) \geq \lambda \\ 0 & \mathcal{L}(\vec{\theta}) < \lambda, \end{cases} \tag{4.12}$$

is replaced by a transformed prior uniform in its parameter space:

$$p_\lambda^{\mathcal{T}}(\vec{\Phi}) = \begin{cases} 1/X(\lambda) & \mathcal{L}(\vec{\theta} \equiv \mathcal{T}(\vec{\Phi})) \geq \lambda \\ 0 & \text{otherwise}, \end{cases} \tag{4.13}$$

where $\mathcal{T}(\vec{\theta})$ maps the original parameter space (which $p(\vec{\theta})$ is not necessarily uniform in) to a space in which $p_\lambda^{\mathcal{T}}(\vec{\Phi})$ is uniform in $\vec{\Phi}$. Once this transformation function has been determined, the problem of sampling $p_\lambda(\vec{\theta})$ has been reduced to producing samples from the uniform distribution $p_\lambda^{\mathcal{T}}(\vec{\Phi})$.

Step-by-step, the basic nested sampling routine can be summarized as follows:

1. Draw $K$ live points $\{\vec{\theta}_1, \dots, \vec{\theta}_K\}$ from the prior distribution.

2. Among the current set of live points find $\vec{\theta}_{\min}$ such that $\mathcal{L}_{\min} \equiv \mathcal{L}(\vec{\theta}_{\min}) < \mathcal{L}(\vec{\theta} \in \{\vec{\theta}_1, \dots, \vec{\theta}_K\})$.

3. Add $\vec{\theta}_{\min}$ to the set of dead points.

4. Draw a new point $\vec{\Phi}$ from the uniform transformed prior $p_{\lambda}^{\mathcal{T}}(\vec{\Phi})$, which satisfies $\mathcal{L}(\vec{\theta}' \equiv \mathcal{T}(\vec{\Phi})) \leq \mathcal{L}_{\min}$

5. Add $\vec{\theta}'$ to the set of live points.

This repeats until a stopping condition is met at which point the final set of live points is converted into dead points. This process is nearly identical to the algorithm above except that once $\vec{\theta}_{\min}$ has been added to the set of dead points and removed from the set of live points, no new point is drawn from the transformed prior. Instead, this removal process continues until no live points remain.

The nested sampling routine is typically considered to be complete when the estimated remaining evidence to be integrated over will contribute a negligible amount to the total evidence estimate. Mathematically, the sampling terminates when

$$\Delta \ln \hat{\mathcal{Z}}_i < \epsilon, \tag{4.14}$$

where $\Delta \ln \hat{\mathcal{Z}}_i$ is the estimated remaining evidence contribution and $\epsilon$ quantifies our tolerance for what is considered a "negligible" contribution. Since $\Delta \ln \hat{\mathcal{Z}}_i$ cannot be known exactly, it is typically estimated from the rough upper bound $\Delta \ln \hat{\mathcal{Z}}_i < \mathcal{L}_i^{\max} \hat{X}_i$ where $\mathcal{L}_i^{\max}$ is the maximum likelihood value among the set of live points at iteration $i$ and $\hat{X}_i$ is the estimate for the remaining prior volume.

The result is a set of $N$ dead points and the final set of $K$ live points from which we can numerically integrate Eq. 4.10 using the trapezoid rule:

$$\begin{aligned} \mathcal{Z} &= \int_0^1 \mathcal{L}(X) dX \qquad (4.15) \\ &\approx \sum_{i=1}^{N+K} \frac{1}{2} \left[ \mathcal{L}(\vec{\theta}_{i-1}) + \mathcal{L}(\vec{\theta}_i) \right] \times \left[ \hat{X}_{i-1} - \hat{X}_i \right] \equiv \hat{\mathcal{Z}}, \qquad (4.16) \end{aligned}$$

where the quantity being summed over are the *importance weights*,

$$\hat{p}_i(\vec{\theta}_i) \equiv \frac{1}{2}\left[\mathcal{L}(\vec{\theta}_{i-1}) + \mathcal{L}(\vec{\theta}_i)\right] \times \left[\hat{X}_{i-1} - \hat{X}_i\right]. \tag{4.17}$$

The posterior can then be estimated from the importance weights and the evidence estimate:

$$p(\vec{\theta}|d,m) \approx \frac{\sum_{i=1}^{N+K} \hat{p}_i(\vec{\theta}_i)\delta(\vec{\theta} - \vec{\theta}_i)}{\hat{\mathcal{Z}}}. \tag{4.18}$$

What's been described here is not precisely the procedure used in `dynesty`. During each loop of the sampler, the number of live points remains constant. As the name suggests, *dynamic* nested sampling allows for the number of live points to vary over the course of the analysis. Variation of the number of active live points allows for finer sampling of regions of higher posterior mass as quantified by a posterior "importance function", effectively prioritizing posterior estimation over expedited integration of the evidence. A more detailed description of dynamic nested sampling can be found in Ref. [42], but crudely the standard NS algorithm is modified as follows:

1. A standard "static" nested sampling routine is performed to produce a baseline distribution.
2. An importance function is evaluated on the samples produced which identifies regions of high posterior mass.
3. Additional live points with parameter values restricted to the identified areas of interest are allocated.
4. The new samples produced from the added live points are then "merged" with the previous sample set according to [42].

Fig. 4.2 shows the results of two Bayesian parameter estimation routines–one MCMC and one dynamic NS–applied to simulated GW data containing a signal produced with

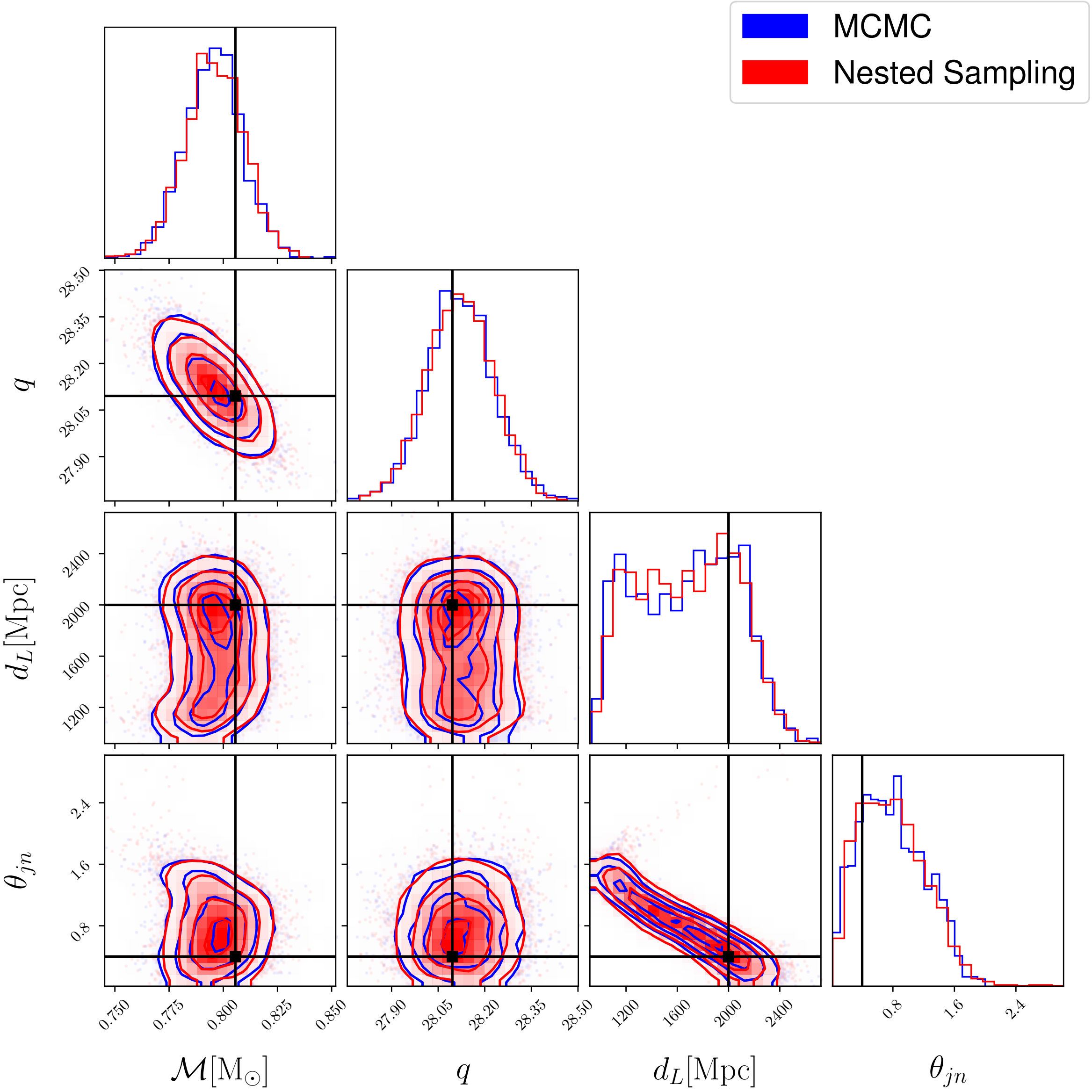

Figure 4.2: Comparison of Bayesian MCMC and Nested Sampling routines applied to a simulated GW signal with restricted model parameters using the `bilby` Bayesian inference software package. Black lines indicate the injected values for each of the parameters.

waveform model `IMRPhenomPv2`, discussed in Chapter 2.

# Chapter 5

# Gravitational Glint

The search for “new physics” typically implies looking for evidence of inadequacies in our current models of natural phenomena. Often times such searches are motivated by observations that are ostensibly inconsistent with existing models of physics however this is not always the case. Theories don’t always advertise their consequences, and sometimes it takes anomalous data to encourage their reexamination to reveal fascinating subtleties. In this chapter, we’ll explore on subtlety of GWs that has the potential to provide us with valuable insight into the astrophysical objects that generate them, and even perhaps uncover the existence of more exotic objects.

## 5.1 Theory review

In GR, GWs are thought to propagate at the speed of light, i.e. on the null cone. While this is true in Minkowski geometry, it’s less commonly known that when propagating through curved spacetime, GWs have a component that propagates on the interior of the lightcone [43]. Because this additional signal contribution arrives after the nullcone contribution, it is referred to as the GW “tail”. In this work we consider tail-producing spacetime inhomogeneities from massive perturbers. There are three distinct epochs of the GW tail: an early and late-time tail which correspond to the first and last times the null cone signal could travel from the source to the perturber to the observer, and the middle-time tail, which depends on interactions between the null cone signal and the curved geometry introduced by the mass distribution of the perturber. It's been shown [44] that the middle-time tail (MTT) is significantly stronger than both the early and late time tails and under certain circumstances, an optimistic candidate for detection. Shown in Fig. 5.1 is a diagrammatic representation of a tail- or "glint"-producing system.

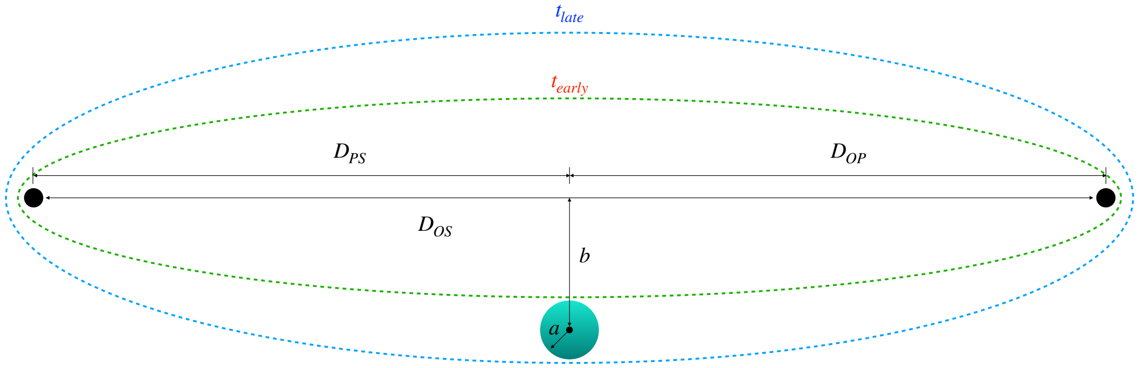

Figure 5.1: A source distance $D_{OS}$ from an observer with a perturber a distance $b \gg a$ from the midpoint of the line-of sight axis between GW source and observer. The presence of a perturber causes propagation of GW on the interior of the null cone producing a GW "tail". Contributions to the tail can be divided into early-, middle-, and late-time with the middle-time tail providing a significantly stronger contribution.

GWs are emitted from a source a distance $D_{OS}$ from an observer. A massive perturber of radius $a$ is situated some distance $b$ from the line of sight (LOS) between the primary GW source and the observer. Assuming a perturber with spherically symmetric density profile

$$\rho(r) = \begin{cases} \rho_{\text{central}} \left(1 - \frac{r^2}{a^2}\right)^p, & r \leq a \\ 0, & r > a \end{cases} \tag{5.1}$$

the MTT GW strain can be calculated under the following assumptions:

1. The density profile of the perturber is sufficiently smooth ($p \geq 4$).

2. The perturber is sufficiently diffuse, i.e. the Schwarzschild radius of the perturber is much less than its radius $r_S = 2G_N M_P/c^2 \ll a$.

3. The distance to the perturber along the LOS to be $\ell \equiv D_{\rm OS}/2$.

4. The distance of the perturber to the LOS $b \ll \ell$.

5. The GWs are long-wavelength, $f_{\rm GW}^{-1} \gg \tau_{\rm middle} \equiv (t_{\rm late} - t_{\rm early})$.

Let's briefly discuss the reasoning for each of these assumptions. The first assumption is required to ensure the calculation of the strain of the MTT yields meaningful results. The spacetime geometries of overly compact perturbers are too extreme to produce interesting scattering which necessitates the second item. While the third assumption is not necessarily a firm requirement[1], we will adopt it to ensure validity of results. As we'll see later, the relative amplitude of the MTT to the primary signal scales with $\ell/b^2$ which implies if $b \gg \ell$, the effect will be too small to observe. And finally, long-wavelength GWs ensure the MTT retains the spectral morphology of the primary GW waveform.

These assumptions permit an analytic expression for the amplitude of the MTT,

$$|\ddot{h}_{ij}^{\rm TT;middle}| = \frac{32 G_N^2 m_{\rm b} M_P f_P R_{\rm b}^2 \Omega_{\rm b}^4}{b^2 c^2}, \tag{5.2}$$

where $m_b$ are the component masses of the equal-mass binary that produces the primary signal, $R_b$ is the orbital radius, $\Omega_b = \sqrt{2G_N m_b/R_b^3}$ is the angular frequency of the binary, $M_P$ is the mass of the perturber, and $f_P$ is a parameter describing the density profile of the perturber ($f_P = 1$ for $p = 4$ in Eq. 5.1). The perturber must also be a few factors of the Einstein radius $x_E$ away from the LOS between the source and observer:

$$n_E \equiv \frac{b}{\sqrt{\frac{4G_N M_P}{c^2}\frac{D_{\rm OP}D_{\rm PS}}{D_{\rm OS}}}} = \frac{b}{\sqrt{\frac{2G_N M_P \ell}{c^2}}} \gtrsim \mathcal{O}(1). \tag{5.3}$$

---

[1] Cursory investigations into the robustness of results with respect to this assumption indicate validity to leading order in $\Delta\ell/\ell$, but a careful analysis has not yet been performed.

Finally the ratio of the null cone signal strain,

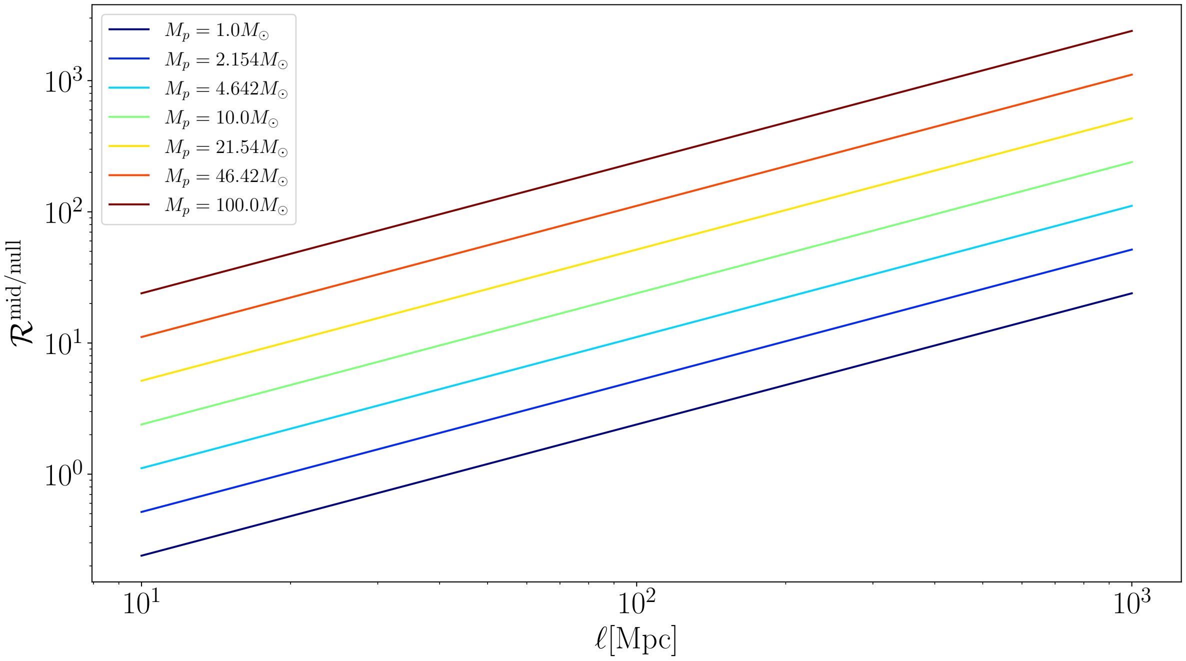

Figure 5.2: Dependence of relative amplitude of glint signal to the null cone signal as a function of line-of-sight distance between the source and observer for different perturber masses.

$$|\ddot{h}_{ij}^{\text{TT;null}}| = \frac{32 G_N m_{\text{b}} R_{\text{b}}^2 \Omega_{\text{b}}^4}{\ell c^2}, \tag{5.4}$$

to the MTT signal reduces to

$$|\mathcal{R}^{\text{mid/null}}| \equiv \frac{|\ddot{h}_{ij}^{\text{TT;middle}}|}{|\ddot{h}_{ij}^{\text{TT;null}}|} = \frac{G_N M_P f_P \ell}{b^2 c^2} = \frac{f_P}{n_E^2}. \tag{5.5}$$

The MTT arrives after the primary signal with a time delay of $\Delta t_{\text{early}}$ given by

$$f_{\text{GW}} \Delta t_{\text{early}} \simeq 10^{-3} n_E^2 \frac{M_P}{\text{M}_\odot} \frac{f_{\text{GW}}}{100\text{Hz}}. \tag{5.6}$$

In the long wavelength regime, the MTT has minimal spectral distortion with respect to the primary signal and is therefore its near-perfect echo described by just two parameters: $\{\Delta t_{\text{early}}, \mathcal{R}^{\text{mid/null}}\}$. As a rough estimate, we can assume the perturbers are uniformly

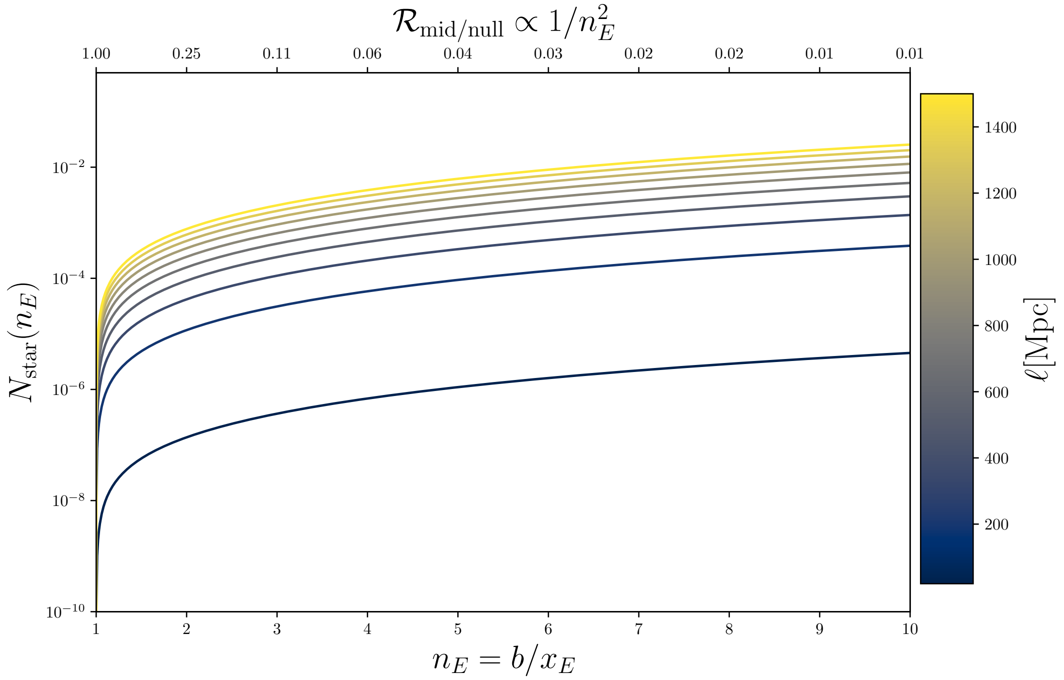

(a) Stellar perturbers with $\Omega_{\rm P} = \Omega_{\rm star} = 0.003$

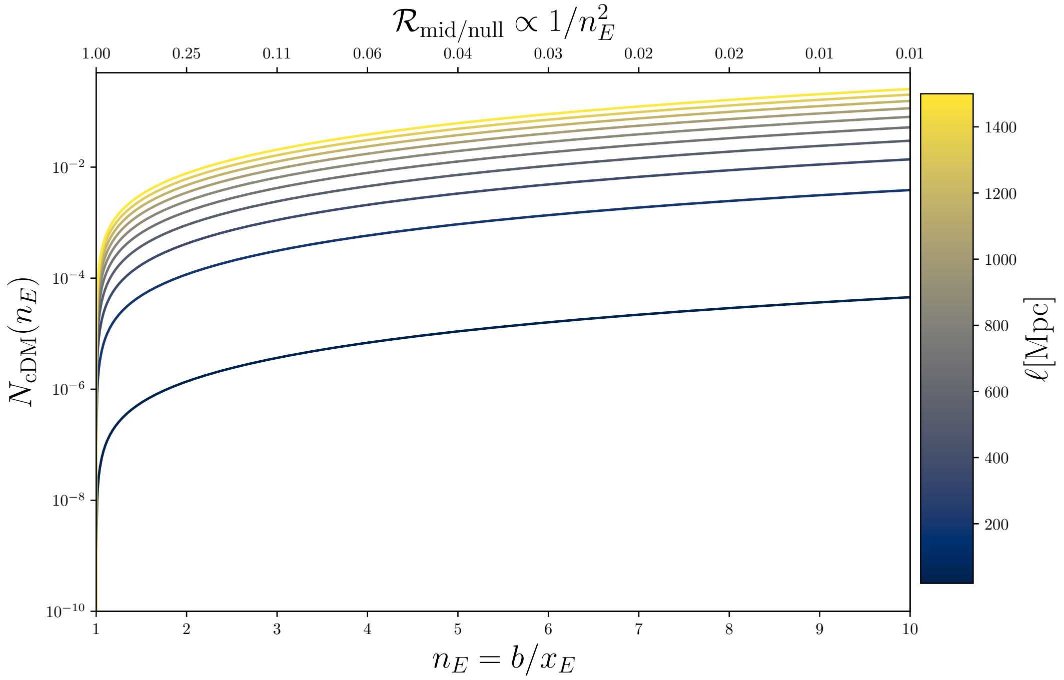

(b) Compact dark matter perturbers with $\Omega_{\rm P} = \Omega_{\rm cDM} = 0.03$

Figure 5.3: Number of uniformly distributed perturbers found within $n_E > 1$ Einstein radii from the LOS axis between an observer and a source at distance $\ell$.

distributed between the observer and the source. The expected number of perturbers of mass $M_P$ positioned within $n_E > 1$ Einstein radii of the LOS between the source and observer can be estimated as

$$N_P(n_E) = \frac{3}{4}\Omega_P(H_0\ell/c)^2\frac{\Delta\ell}{\ell}(n_E^2 - 1) \tag{5.7}$$

$$= \frac{3}{4}\Omega_P(H_0\ell/c)^2\frac{\Delta\ell}{\ell}\left(\frac{f_P}{\mathcal{R}^{\text{mid/null}}} - 1\right), \tag{5.8}$$

where $\Omega_P$ is the fractional energy density of the Universe made up by perturbers, $H_0$ is the value of the Hubble parameter today, $\Delta\ell/\ell$ quantifies the perturber's deviation along the LOS from the midpoint, and we've used Eq. 5.5 to relate $n_E^2$ and $\mathcal{R}^{\text{mid/null}}$. Applying our assumptions earlier, we set $\Delta\ell/\ell = 1.$. Therefore, the rate at which we expect glints of a given relative amplitude is largely determined by the abundance of glint-producing perturbers in the Universe and the distance between the source and observer $d_L = 2\ell$. Fig. 5.3 shows the dependence of $N_P(n_E)$ on the source-observer separation for two cases of perturbers: standard stellar objects which have $\Omega_{\text{star}} \gtrsim 0.003$ and sub-solar-mass compact dark matter objects with masses between $M_P \in [10^{-11}, 1]\text{M}_\odot$, whose fractional energy density has been constrained to $\Omega_{\text{cDM}} \lesssim 0.03$. Figs. 5.3a and 5.3b should be interpreted as lower and upper bounds on $N_P(n_E)$, respectively.

### Phenomenological parameterization

Gravitational-wave tails result in a relatively simple alteration to existing models for GW's from mergers of compact binaries. For a given GW with associated strain $h_s(t)$ and Fourier transform $\mathcal{F}\{h_s(t)\} \equiv \tilde{h}_s(f)$, the primary signal will be modified simply by the addition of an attenuated, spectrally equivalent copy, arriving at some time $\Delta t$ after the primary signal

$$h(t) = h_s(t) + \varepsilon h_s(t - \Delta t), \tag{5.9}$$

where $\varepsilon$ is the fractional amplitude of the primary signal, and $\Delta t$ is the arrival time difference between the primary signal and the tail. and its Fourier modes will be altered by

$$\tilde{h}(f) = \tilde{h}_s(f)[1 + \varepsilon \exp(2\pi i \Delta t)]. \tag{5.10}$$

Note that the correction is frequency-independent, which implies in turn that the addition of GW tails does not depend on the specific waveform model chosen for the primary signal. While this is a parameterization is phenomenological, it can be mapped back to the geometric and physical parameters of the system.

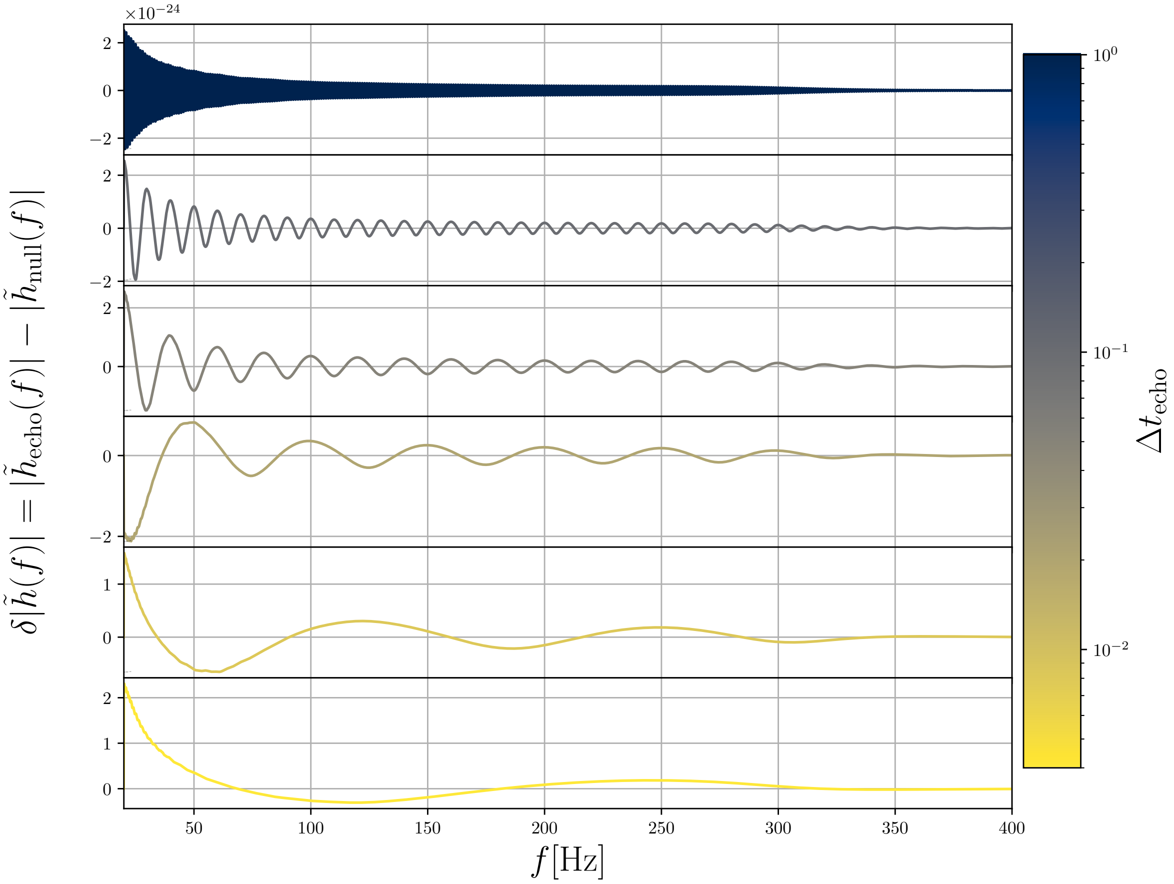

Figure 5.4: Glint-induced frequency domain alteration to the null cone signal as a function of $\Delta t_{\rm glint}$. From bottom to top the glint time delays shown are $\Delta t_{\rm glint}\ in\{0.004, 0.008, 0.02, 0.05, 0.1, 1\}$ s.

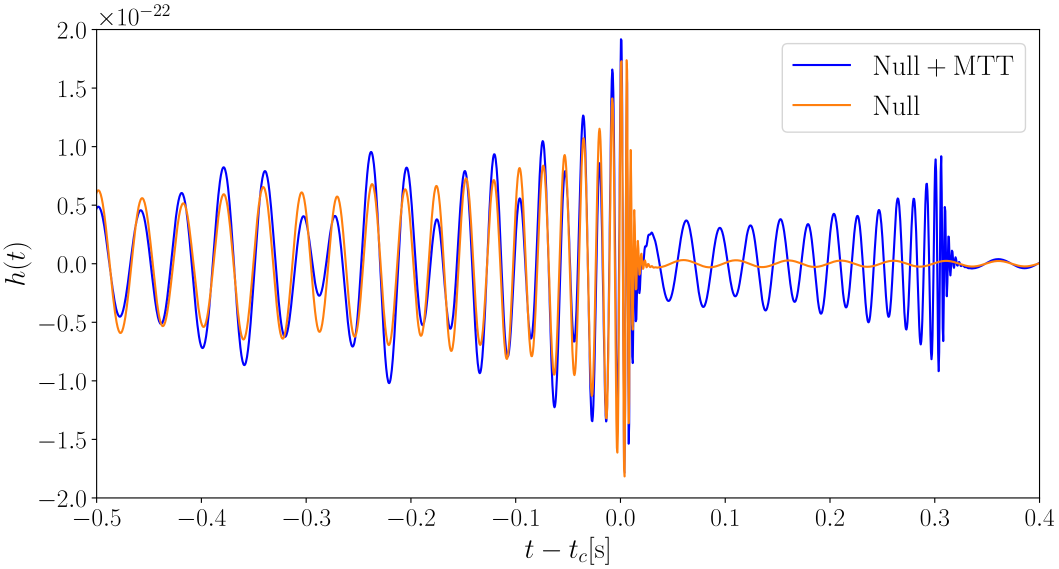

(a) Alteration to time domain detector response of $26-36\mathrm{M}_\odot$ BBH at a distance of $d_L = 2000$ Mpc accompanied by a glint with $\varepsilon_{\text{glint}} = 0.5$ and $\Delta t_{\text{glint}} = 0.3$s. Waveform shown was generated with the `IMRPhenomXPHM` using `bilby` and `lalsimulation`.

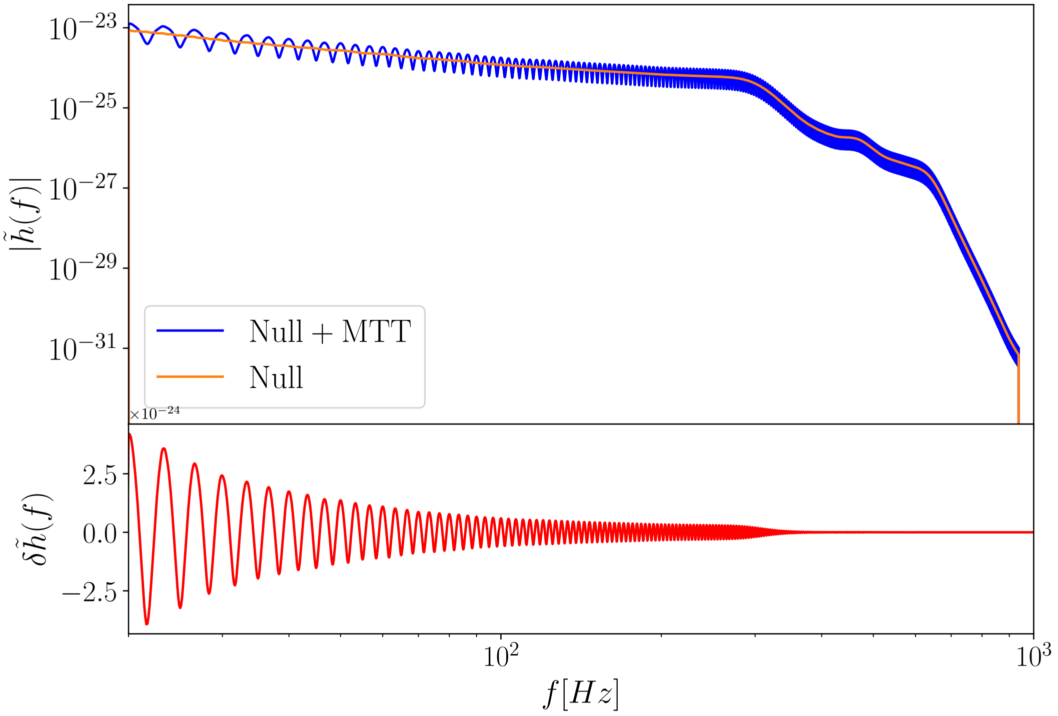

(b) Alteration to frequency domain detector response of standard BBH waveform model in the presence of a glint with $\varepsilon_{\text{glint}} = 0.5$ and $\Delta t_{\text{glint}} = 0.3$s.

Figure 5.5: Time and frequency domain alterations to BBH null cone GW as observed in the LIGO Livingston detector. The glint signal shown has parameters $\varepsilon_{\text{glint}} = 0.5$ and $\Delta t_{\text{glint}} = 0.3$s.

It should be mentioned that strong lensing of GWs produces a similar time-delayed echo of GWs which may raise concerns of the distinguishability of these two effects. Thankfully, however, secondary images produced from strong lensing and echoes produced from glint effects described above predict vastly different time delays. Images from strong lensing are expected to appear between hours to weeks after the primary signal is detected, while time delays for glints are expected to arrive between just milliseconds to at most several seconds after the primary signal arrives [45].

Moving forward, we will also operate under the assumption that any GW signals accompanied by a glint will have only one glint appearing after the primary signal. If multiple perturbers appear just off of the line of sight between the source and observer, this may not strictly be true. However, multiple perturbers placed at different locations off of the LOS will produce glints with different time delays from the primary signal. As we'll see later, even when signals are separated by very small time delays (i.e. fractions of a GW cycle at its highest frequency), we are still able to resolve the individual signals with high precision.

Finally, while this model is agnostic to the frequency range of the primary GW signal, and therefore glints could be observable in GW observatories that target signals in any frequency band. However, observatories like LISA will be sensitive only to the inspiral phase of CBC events, which introduce challenges when detecting glints. In particular, the frequency of a GW during the inspiral phase evolves significantly slower than the last few seconds to merger. This means that a primary signal accompanied by a glint detected in LISA data would resemble two identical near-monochromatic signals with a small phase shift introduced. While this may well be detectible, it would be much more difficult to confirm its origin as a glint without the merger or any remarkable frequency evolution present in the data. Other techniques for GW observation such as pulsar timing arrays (PTA) have the same issue when considering glint detection from continuous-wave sources.

## 5.2 Injection Study

Typically, detection of GWs is characterized by a search pipeline in which some search algorithm is applied to GW strain data which identifies areas of interest. For example, matched filter searches compare GW model templates of various parameters to data segments, effectively filtering the data over each template. When a signal is present, a template will match the data segment, indicating the presence of a signal. The nature of gravitational glints however, motivate a different method for detection[2].

Gravitational glint signals will always have an amplitude strictly less than the primary signal. This makes a scenario in which a glint signal is identified by a GW search pipeline without an accompanied primary signal highly unlikely, meaning only data segments containing preexisting confirmed GW signals need to be reanalyzed for the presence of a glint. We therefore define our detection criterion based on the ratio of Bayesian evidences between the two models. More specifically, given a model describing the detector response for only the null cone signal, $\mathcal{H}_0$ and a second model $\mathcal{H}_{\text{glint}}$ including the modifications from the MTT signal as described above, we evaluate the probability of the presence of a glint by the Bayes factor between the two models:

$$K = \ln \mathcal{B} = \ln \frac{\mathcal{Z}_{\text{glint}}}{\mathcal{Z}_0}, \tag{5.11}$$

where $\mathcal{Z}_i$ is the Bayesian evidence associated with model $\mathcal{H}_i$. We adopt Ref. [46]'s interpretation of the Bayes factor, displayed in Table 5.1, with the sign of $K$ indicated which model is preferred.

We begin with an injection study to forecast the prospect of glint detection using this model selection-inspired detection definition and characterize its dependence on the glint parameter space $\{\varepsilon_{\text{glint}}, \Delta t_{\text{glint}}\}$. The Bayesian evidences and posteriors are estimated

---

[2] If a gravitational glint is present in LVC data, there is a possibility that matched filter searches would fail to identify it if glint-modified waveforms are not included in the bank of templates used in the search. Characterizing the effect of glint models on matched-filter searches is actively being researched by collaborators and will be published alongside the work presented in this chapter.

| $\|K\|$ | Strength of evidence |
|---|---|
| $0 < \|K\| < 1$ | Weak |
| $1 < \|K\| < 3$ | Positive |
| $3 < \|K\| < 5$ | Strong |
| $\|K\| > 5$ | Very strong |

Table 5.1: Interpretation of Bayes factor as strength of preference for one model over another. Bayes factor between MTT+Null and Null signal models are used to evaluate detection confidence.

for a total of 46 injected signals using the `dynesty`[3] implementation of dynamic nested sampling within the `Bilby` software package[4], a Bayesian inference software designed for GW parameter estimation. By "injected", we mean a waveform was produced according to a specific waveform model with some set of model parameters, and then "injected" into GW strain data simulated according to a PSD estimated from a long ($\mathcal{O}(10^3)$ s) segment of LIGO strain data known to be absent of any GW signal. All waveform models are generated using `IMRPhenomPv2` (discussed in Chapter 2) waveform model through the `lalsimulation` code[5].

The standard null cone GW signal parameters are held fixed, chosen to represent a typical BBH signal[6] of SNR $\sim 12$, while the glint signal parameters are varied in the ranges $\varepsilon_{\text{glint}} \in [0.01, 1]$ and $\Delta t_{\text{glint}} \in [1/4f_{\text{GW}}, 1]$ s. A summary of all injection parameters and their values is shown in Table. 5.2. Each simulated signal is analyzed twice: once using the standard null cone GW waveform which does *not* include glint effects, and once again with the glint modifications included producing posterior samples and the evidences for each. The priors used are as follows:

- Masses: Uniform in $\{\mathcal{M}, q\} \in [25, 100]\text{M}_\odot$.
- Luminosity distance: Uniform in source frame distance $d_L \in [100, 5000]$ Mpc assuming ΛCDM cosmology with Planck 2015 cosmological parameters [47].

---

[3] `https://github.com/joshspeagle/dynesty`

[4] `https://git.ligo.org/lscsoft/bilby`

[5] `https://git.ligo.org/lscsoft/lalsuite/-/tree/master/lalsimulation`

[6] The null cone signals will all have the same SNR. However, since the addition of the glint signal adds additional signal power, the SNR does vary with $\varepsilon_{\text{glint}}$.

- The angle between the total angular momentum of the binary and line of site vector: $\theta_{jn}$ is sampled sinusoidally in the range $[0, \pi]$.

- The remaining parameters $\{\alpha, \delta, \phi_c, \psi, a_1, a_2, \theta_1, \theta_2, \phi_{12}, \phi_{jl}\}$ are all fixed to their injection values.

The fixed parameters describe the sky location, orientation of the binary relative to the detector, and the spins of the binary components. We performed several additional simulations to ensure that fixing the above parameters and sampling in the restricted parameter space did not significantly affect the results of the injection study.

Signals were injected into zero-noise strain data, though the PSD used in the likelihood evaluation (Eq. 4.4) was estimated from public detector data for L1 and H1. This is equivalent to averaging over repeated analyses for different noise realizations drawn from the PSD. We performed several more simulations investigating the effect of injecting into specific noise realizations and found results consistent with a zero-noise injection. Finally, the evidences for the two analyses are used to compute the Bayes factor according to Eq. 5.11.

The first 36 simulations served as a course sampling over the entire glint parameter space to identify key transition points in the dependence of the Bayes factors on the glint parameters:

$$
\begin{aligned}
\varepsilon_{\mathrm{glint}} &\in \{0.01, 0.2, 0.4, 0.6, 0.8, 1\} \\
\Delta t_{\mathrm{glint}} &\in \{1/4f_{\mathrm{GW}}, 1/3f_{\mathrm{GW}}, 1/2f_{\mathrm{GW}}, 1/2f_{\mathrm{GW}}, 1/f_{\mathrm{GW}}, 0.5, 1\}\ \mathrm{s}
\end{aligned}
$$

The relative glint amplitude has natural upper and lower limits: the glint signal can at most be equal in amplitude to the primary signal and at minimum have 0 amplitude (non-existent). The time delay from the primary signal however, is slightly less straight forward. We postulate the $\Delta t_{\mathrm{glint}}$ parameter space can be divided into three regimes:

| Parameter | Injected value | Parameter | Injected value |
|---|---|---|---|
| $m_1$ | 36 $M_\odot$ | $\delta$ | -1.211 |
| $m_2$ | 29 $M_\odot$ | $\theta_1$ | 0.5 |
| $d_L$ | 2000 Mpc | $\theta_2$ | 1.0 |
| $a_1$ | 0.4 | $\phi_{12}$ | 1.7 |
| $a_2$ | 0.3 | $\phi_{jl}$ | 0.3 |
| $\varepsilon_{\text{glint}}$ | [0.01, 1] | $\theta_{jn}$ | 0.4 |
| $\Delta t_{\text{glint}}$ | $[1/4f_{\text{GW}}, 1]$ s | $\psi$ | 2.659 |
| $\alpha$ | 1.375 | | |

Table 5.2: Parameters for the injected signals analyzed for characterization of detection using the Bayes factor model selection method. All parameters null cone signal parameters are constant for all injected signals while $\varepsilon_{\text{glint}}$ and $\Delta t_{\text{glint}}$ are varied for each injection. The frequency used to determine the time delay from the primary signal is taken to be $f_{\text{GW}} \approx 66$ Hz.

1. The glint is well separated from the primary signal $\Delta t_{\text{glint}} \sim \mathcal{O}(1)$ s.

2. The glint is overlapping, but separated by several GW periods.

3. The glint is separated by within one GW cycle $\Delta t_{\text{glint}} \sim \tau_{\text{GW}} \equiv 1/f_{\text{GW}}$, where we take $f_{\text{GW}} \approx 66$Hz.

As we anticipated the two signals would be most difficult to resolve in the third case, $\Delta t_{\text{glint}}$ is more finely tested in this region, making up four of the 6 injections. $\Delta t_{\text{glint}} = 0.5$s and $\Delta t_{\text{glint}} = 1$s cover cases 2) and 1) respectively. The Bayes factors for each of the 36 $\varepsilon_{\text{glint}}$-$\Delta t_{\text{glint}}$ pairs are reported in Table 5.3 and an example comparison between recovery with and without glint parameters is shown in Fig. 5.6 for a time delay of $\Delta t_{\text{glint}} = \tau_{\text{GW}} \approx 0.015$s and relative amplitude $\varepsilon_{\text{glint}} = 0.6$. The natural log Bayes factors are largely independent of the time delay between the primary and glint signals, even in the case of $\Delta t_{\text{glint}} \leq \tau_{\text{GW}}$. As expected, the primary dependence is on the relative amplitude to the primary signal. While it's clear from Table 5.3 that for the injection parameters chosen, the glint-supplemented model becomes preferred somewhere between $\varepsilon_{\text{glint}} = 0.2$ and $\varepsilon_{\text{glint}} = 0.4$, it cannot be determined where precisely this transition happens at this resolution in $\varepsilon_{\text{glint}}$. To do so, we perform a follow-up "fine-combed" analysis of an additional 10 injections with evenly spaced $\varepsilon_{\text{glint}} \in [0.218, 0.381]$

|  | 0.01 | 0.2 | 0.4 | 0.6 | 0.8 | 1.0 |
|---|---|---|---|---|---|---|
| $1/4f_{\mathrm{merger}}$ | -2.64 | -2.83 | 2.01 | 21.49 | 47.98 | 80.56 |
| $1/3f_{\mathrm{merger}}$ | -2.59 | -2.65 | 2.96 | 20.60 | 46.60 | 79.18 |
| $1/2f_{\mathrm{merger}}$ | -2.48 | -2.56 | 2.76 | 21.22 | 46.69 | 82.01 |
| $1/f_{\mathrm{merger}}$ | -2.68 | -2.51 | 5.56 | 27.36 | 57.23 | 89.40 |
| 0.5s | -2.56 | -2.30 | 6.77 | 27.63 | 60.51 | 100.07 |
| 1.0s | -2.79 | -2.74 | 7.11 | 28.40 | 60.62 | 100.19 |

Table 5.3: Natural logarithm of the Bayes factors between Null cone model and Null+MTT model as a function of glint amplitude relative to the primary signal amplitude (rows) and time delay from primary signal (columns). Analyses were performed for reduced model space in standard GW parameters. Results were verified to not change significantly when sampling in the full parameter space. See Table 5.1.

at a fixed separation from the primary signal $\Delta t_{\mathrm{glint}} = 1/f_{\mathrm{GW}}$. The dependence of the Bayes factor on the glint amplitude in this range is shown in Fig. 5.7. We find the logarithm of the evidence ratio turns positive just after $\varepsilon_{\mathrm{glint}} \approx 0.3$, reaches "positive" preference around $\varepsilon_{\mathrm{glint}} \approx 0.33$, and finally produces "strong" preference for the glint model at $\varepsilon_{\mathrm{glint}} \approx 0.355$. We emphasize that since $\varepsilon_{\mathrm{glint}}$ is defined as the *relative* amplitude of the glint waveform, the is not general to all GWs of all SNRs. This serves simply as verification that a typical GW of unremarkable SNR does indeed have an identifiable point at which the glint model becomes preferred. Additionally, these results confirm that, assuming a sufficiently loud signal, the presence of a glint has a significant effect on the Bayesian evidence even for closely overlapping signals of $\Delta t_{\mathrm{glint}} \leq \tau_{\mathrm{GW}}$.

## 5.3 Analysis of O1-O3 GW Events

### 5.3.1 Overview of events analyzed

We analyze strain data for 47 events from the first, second, and third Gravitational-Wave Transient Catalogs (GWTC) [16–18] subject to the constraint $\mathrm{SNR}_{\mathrm{Null}} \geq 12$ containing 44 with component masses consistent with black holes, two, GW170817 [48] and GW190425 [49], with component masses consistent with neutron stars, and one, GW190814 [50], with component masses consistent with a neutron-star black-hole

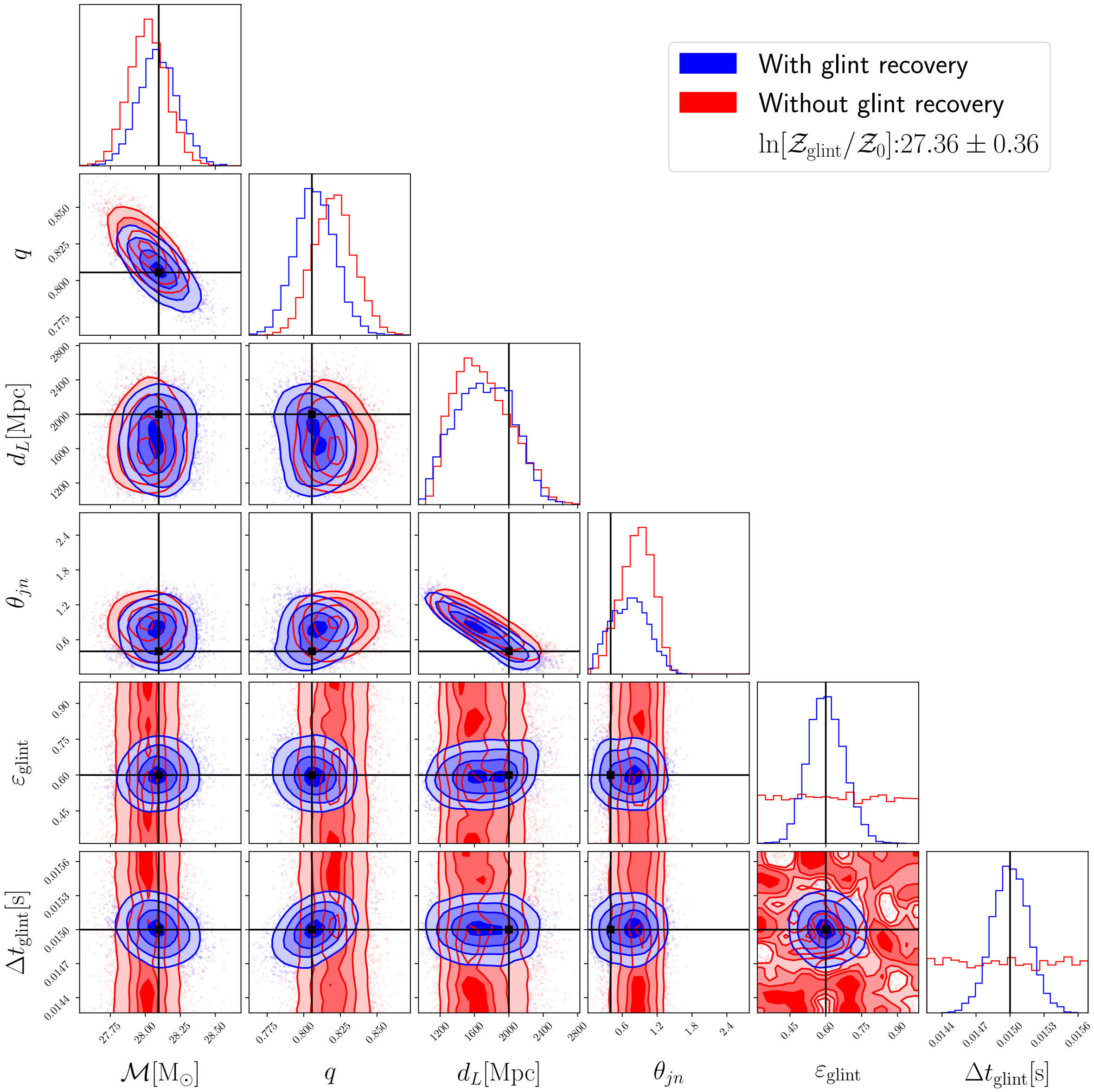

Figure 5.6: Gravitational Glint recovery for a simulated BBH event separated by one GW cycle $\Delta t_{\rm glint} = \tau_{\rm GW} \approx 0.015$s and relative amplitude $\varepsilon_{\rm glint} = 0.6$ with BBH injection parameters outlined in Table 5.2. True parameter values are indicated with black lines.

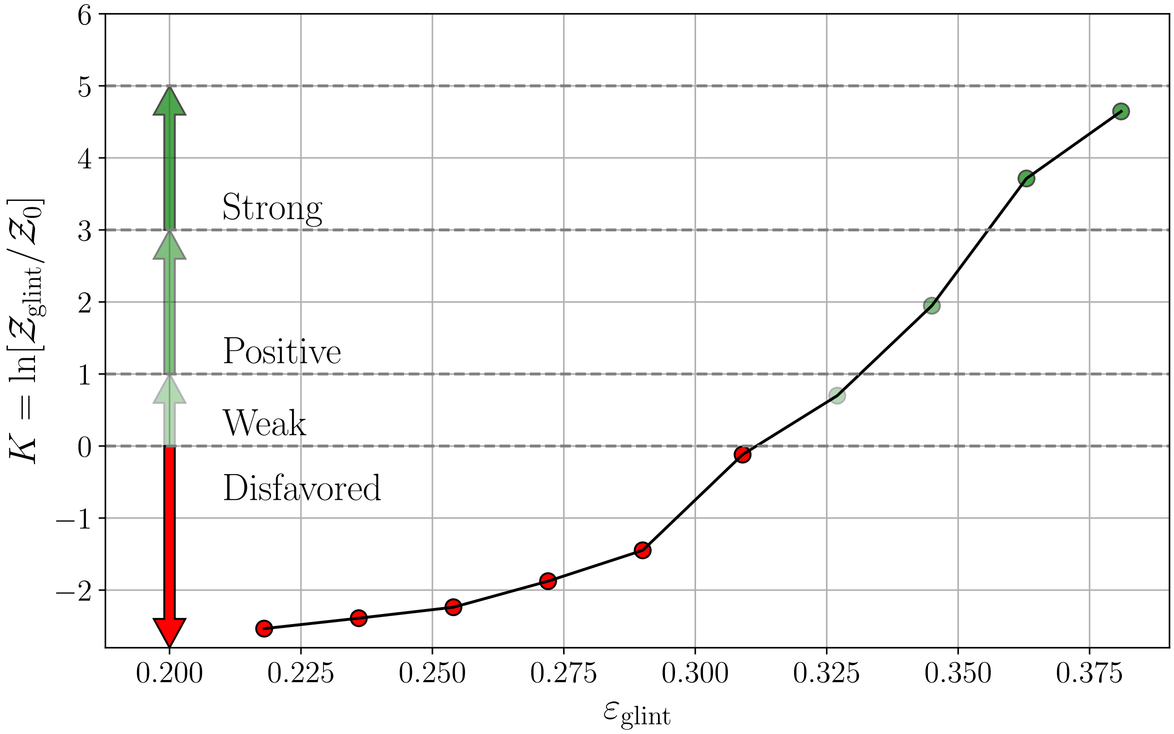

Figure 5.7: Dependence of Bayes factor on glint amplitude relative to the primary signal for $\Delta t_{\rm glint} = \tau_{\rm GW} \approx 0.015$s. Null cone signal parameters can be found in Table 5.2.

(NSBH) merger. Of the two BNS events, GW170817 was accompanied by a coincident gamma-ray burst (GRB), GRB170817A, and there is thus strong consensus that GW170817 and GRB170817A originated from the same merger of two neutron stars. Waveform corrections due to tidal deformation in neutron star matter were also detected in GW170817, further solidifying its classification as a BNS merger. GW190425, on the other hand, had no observed electromagnetic (EM) counterpart and very little information tidal information was recovered, making the recovered component masses the primary evidence for its origin as a BNS merger.

The remaining 44 BBH events have masses ranging from $5.9\mathrm{M}_\odot$ to $95.3\mathrm{M}_\odot$ at distances ranging between 240Mpc and 4420Mpc, summarized in Fig. 5.8. Four of the these 44 events are "marginal" candidates, meaning they do not meet the threshold on the LVC's criterion for probability of astrophysical origin, $p_{\rm astro}$, however these events are still included in our analysis in case the absence of glint effects in the computation of $p_{\mathrm{astro}}$ introduce a bias that lowers its value below the threshold. For more detailed discussion of $p_{\mathrm{astro}}$ and all existing GW detections, defer to Refs. [16–18].

The last remaining event, GW190814 [50], has a roughly 23 $\mathrm{M}_\odot$ black hole primary component, however the nature of the 2.6 $\mathrm{M}_\odot$ secondary component is unclear. The maximum stable mass a neutron star can support has been constrained to $M_{\mathrm{max}} = (1.20^{+0.02}_{-0.05})M_{\mathrm{TOV}}$ where $M_{\mathrm{TOV}}$ has in turn been constrained to the range $2.01^{+0.04}_{-0.04} \leq M_{\mathrm{TOV}}/M_\odot \lesssim 2.16^{+0.17}_{-0.15}$ [51]. Thus while the secondary mass is still consistent with the bounds placed on the maximum sustainable neutron star mass, current estimates of the mass distribution on GW-producing BNS systems [52] place it solidly as an outlier.

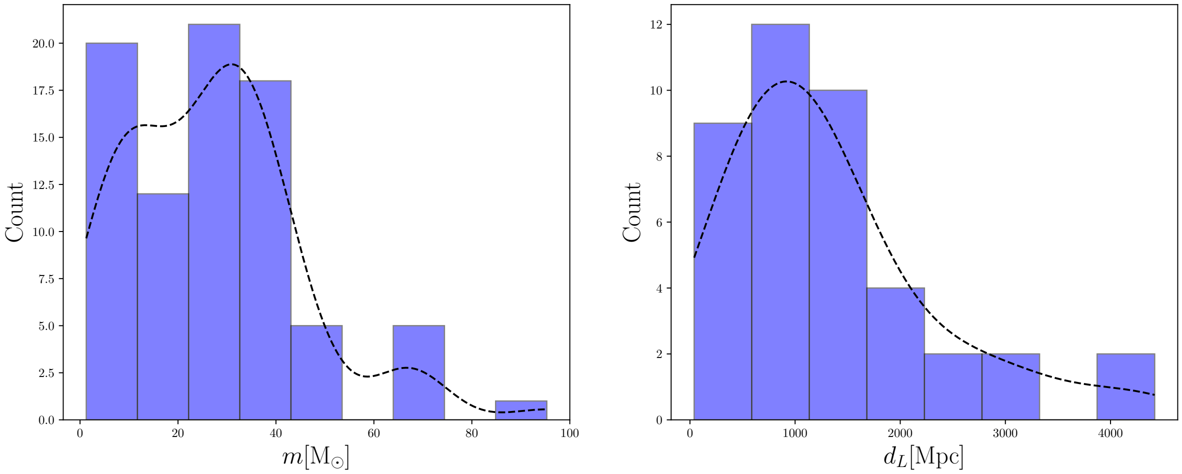

Figure 5.8: Histogram of source component masses and luminosity distances for GWTC1-3 events with SNR> 12.

### 5.3.2 Analysis details

As in the injection study, we use the `bilby` software package to perform integration of the evidence integral and estimation of the posterior, choosing the `dynesty` package to do so. Events are analyzed using public strain data from the Gravitational Wave Open Science Center[7] which is additionally used to estimate the PSD of the noise around the GW event when officially published event PSDs are not explicitly available. As listing

---

[7] `https://gwosc.org/eventapi/html/GWTC/`

all prior choices for all events would be cumbersome, we summarize our prior choices as follows: officially published priors are used when available. When official priors are unavailable, they are chosen to be either uniform in naturally bounded variables (sky location parameters, etc.) or else match injection study parameters with ranges adjusted to match the publicly available parameter estimates. Glint parameter priors match those used in the injection study.

We use the `IMRPhenomXPHM` [53] waveform for most events in order to capture higher-mode contributions to the waveform for events with high mass symmetry. We also use this waveform for near equal-mass binaries as well for consistency. For the two BNS candidate events, we use the `IMRPhenomPv2_NRTidalv2` waveform to capture the effects of tidal deformations on the waveform. We sample not in the component tidal deformabilities, $\Lambda_1$ and $\Lambda_2$, but instead in the leading-order, $\tilde{\Lambda}$ [54], and next-to-leading order, $\delta\tilde{\Lambda}$ [55], tidal contributions to the waveform in the post-Newtonian expansion [56, 57]. These are sampled uniformly in the ranges $\tilde{\Lambda} \in [0, 1000]$ and $\delta\tilde{\Lambda} \in [-5000, 5000]$ respectively. Care is also taken when choosing the prior on the dimensionless spin magnitudes, $a_i \equiv c|\vec{S}_i|/(Gm_i^2)$, for event GW170817. Neutron stars with higher spins can support higher masses while maintaining hydrostatic equilibrium due to neutron degeneracy pressure, and thus restricting the spin prior to low spin values can have significant effects on the recovered tidal and component mass posteriors. While artificially restricting the spin prior may seem like introducing an unnecessary bias into the resulting posterior, there are several considerations that motivate this decision. First, accuracy of existing waveforms, including the ones used in this analysis, is known to degrade at high spins [55]. Moreover, most models for the equation of state for neutron matter only admit stable configurations with $a < 0.7$ [58]. Observational constraints of neutron star spin are even more restrictive, with the fastest-spinning known neutron star having a dimensionless spin constrained to $a \lesssim 0.4$ [59], and the fastest-spinning neutron star that will merge within a Hubble time, PSR J0737-3039A [60], with a dimensionless spin that will be $a \lesssim 0.04$ when it eventually merges. We therefore perform analysis of GW170817 with two spin priors: a *low spin* prior with the component dimensionless spins restricted to $a_i \in [0, 0.05]$, and a *high spin* prior with $a_i \in [0, 0.89]$, consistent with Ref. [48].

The sole event with masses consistent with a neutron star-black hole (NSBH) merger, GW190814 [50], is also analyzed with the `IMRPhenomPv2_NRTidalv2` waveform however we sample tidal deformability only in the secondary mass $\Lambda_2 \in [0, 5000]$ and fix the primary mass tidal deformability to be $\Lambda_1 = 0$, though little tidal information is recovered for the secondary mass [50].

### 5.3.3 Results

All Bayes factors for analyzed events are listed in Table 5.5 and are shown in histogram form in Fig. 5.10. We find $K < 0$ for all but one event analyzed, with the sole positive evidence ratio belonging to GW170817 under the high-spin prior. Table 5.4 lists the Bayes factors for GW170817 between spin prior assumptions and whether or not glint parameters were sampled. The glint model is preferred relative to the null cone model when assuming the high spin prior with $K = 0.63 \pm 0.57$ and the glint model with high spins allowed is preferred over the glint model with restricted spins as well. However, the high spin model is disfavored in all other cases, included comparison between the null cone models.

Fig. 5.9 shows the joint and marginal posteriors on spin, tidal, and echo parameters for GW170817. Three comparisons are shown: one comparison between the null cone and glint models with the high spin prior, another between the null cone and glint models with the low spin prior, and finally a comparison of the glint model under the two spin prior assumptions. Aside from a slightly higher peak in the posterior for the echo amplitude under the high spin prior, Fig. 5.9c shows a high degree of consistency in the parameter posteriors between the two spin priors. The time delay posterior contains a major and minor peak in both cases at the same locations, $\Delta t_{\text{glint}} \approx 0.015, 0.045$ s.

For both spin prior choices, the non-glint signal parameter posteriors largely match

|  | LS | LS+Glint | HS | HS+Glint |
|---|---|---|---|---|
| LS | - | $-2.38 \pm 0.56$ | $-2.8 \pm 0.54$ | $-2.17 \pm 0.56$ |
| LS+Glint | $2.38 \pm 0.56$ | - | $-0.41 \pm 0.57$ | $0.22 \pm 0.59$ |
| HS | $2.8 \pm 0.54$ | $0.41 \pm 0.57$ | - | $0.63 \pm 0.57$ |
| HS+Glint | $2.17 \pm 0.56$ | $-0.22 \pm 0.59$ | $-0.63 \pm 0.57$ | - |

Table 5.4: Natural logarithm of evidence ratios for GW170817 under two spin priors and when recovering with glint parameters and without. Values are listed as the ratio of evidences with the column label in the numerator.

those when recovering without glint parameters. However, we find that when sampling in glint parameters, the dimensionless spin magnitude of the secondary component has slightly less support for 0 spin for both choices of spin prior. The most noticeable discrepancy from the non-glint posteriors arises in the PDF for $\delta\tilde{\Lambda}$ under the high spin prior assumption. The glint model posterior pulls to higher values, while in the low spin case, the posteriors are consistent with the prior, regardless of whether or not glint parameters are sampled. However, official analyses of GW170817 have shown significantly more structure in the posterior of $\tilde{\Lambda}$, while $\delta\tilde{\Lambda}$ remains effectively unmeasured (see Fig. 12 of Ref. [61]). This indicates further investigation into our results for GW170817 is required before they can be completely trusted.

The "best" BBH Bayes factor of $K = -0.05 \pm 0.43$ belongs to event GW190708_232457, a roughly 17+13 $\mathrm{M}_\odot$ BBH merger with a network matched filter SNR of $\approx 13$. Though the error on the log Bayes factor values do include positive values, they do not extend into the "positive" or higher evidence strength levels.

The published analyses of several of the events analyzed had component masses consistent with intermediate mass black holes (IMBH). IMBH events with component masses between $10^2 - 10^3$ $\mathrm{M}_\odot$ have significantly fewer cycles in-band as they merge at significantly lower frequencies. We found that the Bayes factors for certain IMBH events such as 200114_020818 were highly dependent on the minimum frequency at which the waveform is generated during analysis. The standard choice of $f_{\min} = 20$ Hz for IMBH-scale component masses in many cases results in only the merger and post-merger ringdown phases of the signal being in-band. When performing parameter

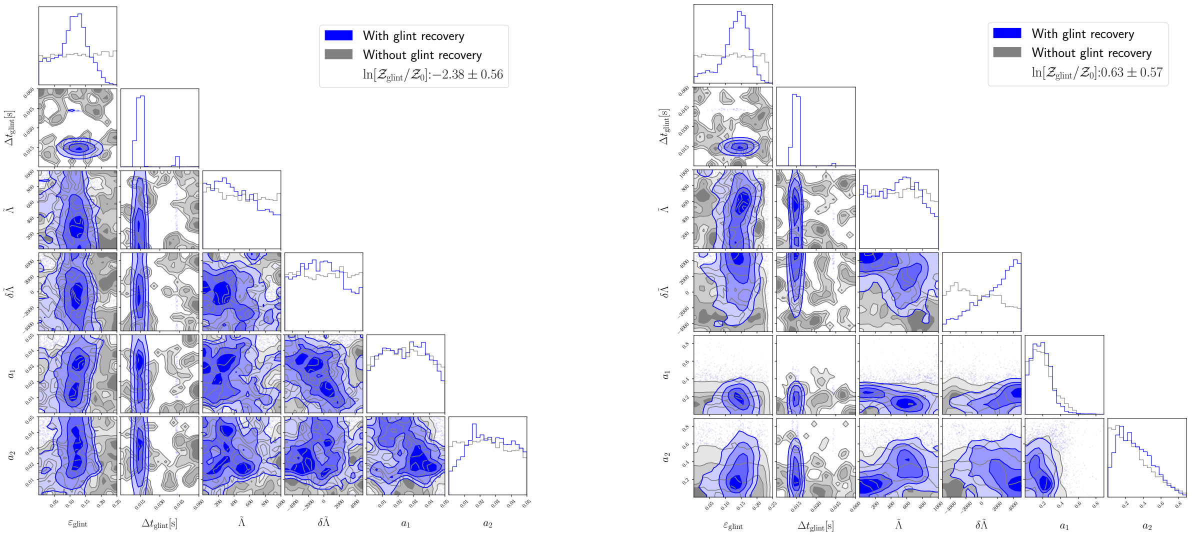

(a) Dimensionless spin magnitudes restricted to $a_i \in [0, 0.05]$.

(b) Dimensionless spin magnitudes restricted to $a_i \in [0, 0.89]$.

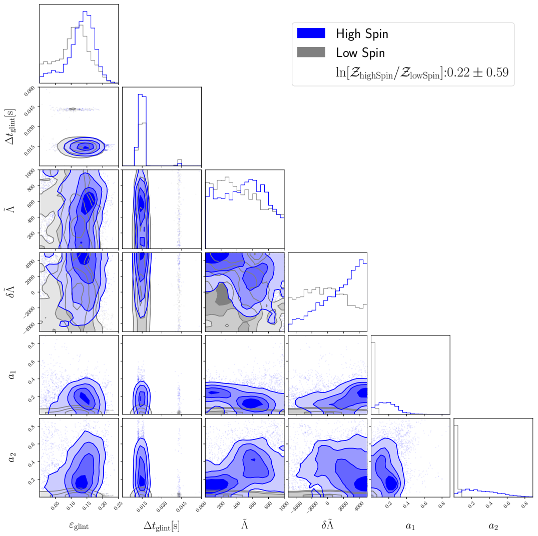

(c) Comparison of glint recovery between both spin priors.

Figure 5.9: Comparison of echo amplitude ($\varepsilon_{\rm glint}$) and time delay ($\Delta t_{\rm glint}$), dimensionless tidal parameters', and dimensionless spin parameters' $a_i \equiv c|\vec{S}_i|/(Gm_i^2)$ PDFs for event GW170817 under two spin priors.

| Event ID | PE SNR | ln[$\mathcal{Z}_{\rm glint}/\mathcal{Z}_0$] | Event ID | PE SNR | ln[$\mathcal{B}_{\rm glint}/\mathcal{B}_0$] |
|---|---|---|---|---|---|
| GW170817 | 33 | -2.38, 0.63$^\dagger$ | GW200105_162426 | 13.7 | - |
| GW200129 | 26.7 | -0.9 | GW190728_064510 | 13.6 | -1.3 |
| GW190814 | 24.9 | -47.9 | GW190708_232457 | 13.4 | -0.05 |
| 191225_215715 | 20.5 | -1.9 | GW190706_222641 | 13.4 | - |
| GW200224_222234 | 20 | -2.0 | 190924_232654 | 13.3 | - |
| GW190412 | 19.8 | -1.5 | GW190924_021846 | 13.2 | - |
| GW191226_213338 | 18.6 | -0.2 | GW190602_175927 | 13.2 | -0.85 |
| GW200311_115853 | 17.8 | - | GW151226 | 13.1 | - |
| GW170814_103043 | 17.7 | -1.2 | GW190915_235702 | 13.1 | - |
| GW191204_171526 | 17.5 | - | GW190707_093326 | 13.1 | - |
| GW191109_010717 | 17.2 | -1.4 | GW191129_134029 | 13.1 | - |
| GW190828_063405 | 16.6 | -0.18 | 200214_224526 | 13.1 | - |
| GW190519_153544 | 15.9 | - | GW170720 | 13 | - |
| GW190630_185205 | 15.6 | -1.1 | GW170809 | 12.8 | - |
| GW170608 | 15.4 | -1.3 | GW190512_180714 | 12.7 | - |
| GW190408_181802 | 14.8 | -0.59 | GW190513_205428 | 12.5 | - |
| GW190910_112807 | 14.5 | -1.4 | GW200225_060421 | 12.5 | -0.55 |
| 200114_020818 | 14.5 | -1.71 | GW191222_033537 | 12.5 | -0.69 |
| GW190521 | 14.2 | -2.23 | GW190727_060333 | 12.3 | - |
| GW190519_153544 | 14 | -1.3 | GW190503_185404 | 12.2 | - |
| - | - | - | GW170823_131358 | 12.1 | -0.76 |
| - | - | - | GW190620_030421 | 12.1 | - |
| - | - | - | GW170818_022509 | 12 | -1.1 |

Table 5.5: Table of analyzed events and ratios of their Bayesian evidences, otherwise known as a Bayes factor. Events with the prefix "GW" are high-significance events included in GWTCs. Those that lack the "GW" prefix are marginal events. The analysis for GW170817 is dependent on the choice of spin prior and thus two evidence ratios are reported for that event. Dashes indicate pending results.

estimation with this choice for $f_{\rm min}$, we do in fact find a very slightly positive log Bayes factor of $K = 0.012$, but this is highly unreliable given the in-band signal duration. When lowering the minimum frequency to 10 Hz, the evidence ratio is significantly lowered to $K = -1.7$.

### 5.3.4 Conclusions

In this work, we've forecasted the viability for detection of secondary GW signals from the MTT produced by off-axis massive perturbers, a potential new probe of compact

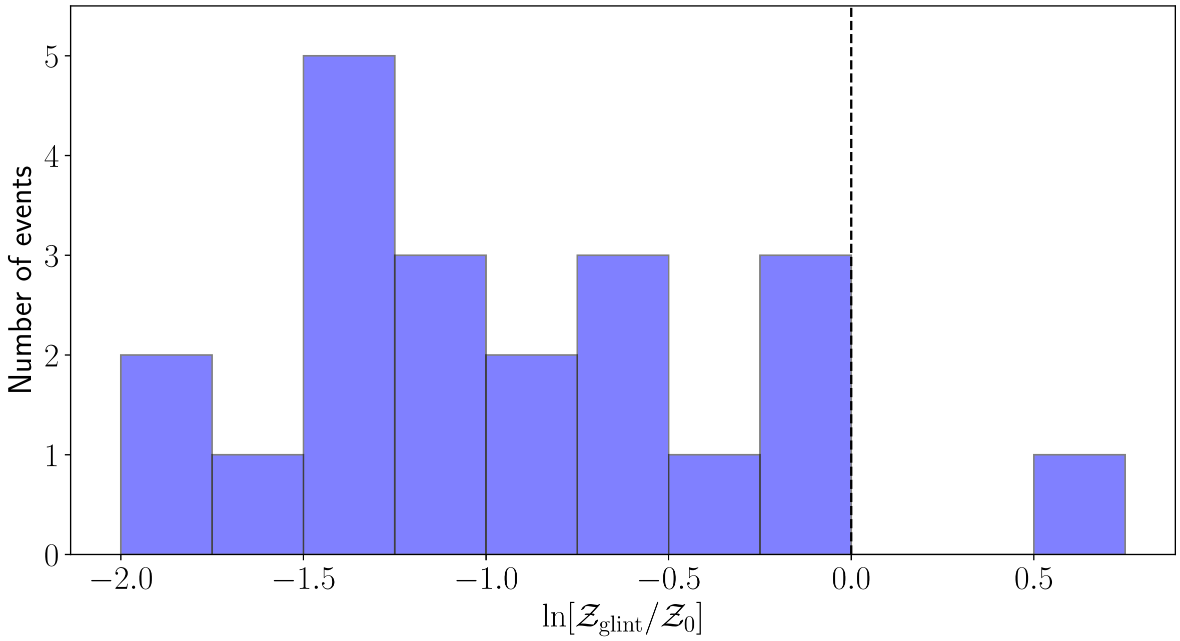

Figure 5.10: Distribution of Bayes factors between recovery with glint model and recovery with standard BBH/BNS waveform. Dashed line indicates where the glint model becomes preferred. The sole positive value of $K = \ln[\mathcal{Z}_{\rm glint}/\mathcal{Z}_0] = 0.63$ belongs to the BNS event GW170817 under the high spin prior. The highest BBH value belongs to the event GW190708_232457 with $\ln[\mathcal{Z}_{\rm glint}/\mathcal{Z}_0] = -0.05$.

dark matter objects and stellar populations. Using a Bayes factor detection criterion, we confirm that for a typical BBH merger signal of SNR $\approx 13$ accompanied by a glint, inclusion of the glint model improves the Bayesian model evidence by a factor of $e^3$, corresponding to strong model preference, at a relative glint amplitude of $\varepsilon_{\rm glint} \approx 3.55$. Importantly, even in signals where the glint has high overlap with the primary signal, $\Delta t_{\rm glint} \lesssim \tau_{\rm GW}$, the glint-supplemented model is still strongly preferred provided the glint amplitude satisfies the previous requirement.

We perform the first search for the presence of glints in existing GW strain data for 47 events belonging to the first three Gravitational Wave Transient Catalogs, GWTC1-3, all with SNR$> 12$ and compute Bayes factors for each. We find no substantial evidence for the presence of glints in any of the events analyzed with the highest measured Bayes factor belonging to event GW170817 under the assumption all spin values are equally likely. While the upper BF errors for some of the remaining events do include positive values, none included the possibility of strong preference for the glint model.

Currently, work is being done to use the computed Bayes' factors to estimate the rate at which glint-producing events can be expected given our null detection. This involves determining the lowest glint amplitude which could be confidently detected for each event analyzed. Knowledge of this cutoff on $\varepsilon_{\mathrm{glint}}$ can then be used to determine whether or not a glint could have been observed in each signal given its null cone signal parameters.

Our results are still consistent with the estimate of one glint with amplitude $\varepsilon_{\mathrm{glint}} = 0.3$ for every 225 sources observed [44] when the perturbers are taken to be stars with $\Omega_{\mathrm{star}} \gtrsim 0.003$. With next-generation GW detectors such as Einstein Telescope and Cosmic Explorer expected to produce $\mathcal{O}(10^3)$ BBH merger signals with SNR$\geq 100$ by 2050, glint detection may be inevitable, and prove an invaluable tool for constraining the abundance of compact dark matter or other exotic compact objects.

# Chapter 6

# Polymer Gravity

Inspired by loop quantum gravity, the polymer quantization scheme is an alternative representation of the canonical commutation relations and has already been explored as a possible alternative to the Schroëdinger quantization of the electromagnetic field [62]. In polymer-quantized EM radiation, pulses resembling short gamma-ray bursts (sGRB) incur a reduction of propagation speed dependent on the characteristic scale of the polymer quantization, the pulse amplitude, pulse width, and the pulse frequency. The authors of Ref. [62] use constraints on the traveling time differences between different frequencies of GRB090510 [63] to place bounds on the polymer scale describing quantization of the EM sector. However, their results indicate that polymer quantization is a poor alternative for quantization of the EM sector.

It is important to note that polymer EM theory and polymer GWs have different foundations and the resulting constraints on the corresponding characteristic scales therefore have different interpretations. In Ref. [62], the polymer quantization scheme is applied to the electromagnetic four-potential in an exclusively Minkowski spacetime. The characteristic polymer scale, $\mu$, quantifies the discreteness of the electromagnetic polymer fields. As we'll discuss later on, when polymer quantization is applied to metric perturbations, the quantity $\mu$ quantifies the discreteness of the metric perturbations with the assumption that the background spacetime evolves classically.

While unlikely to be a replacement for quantum EM effects, possible connection with Planck-scale physics has made the polymer quantization scheme an attractive candidate for describe quantum gravitational effects [64–67]. Polymer corrections have been found to violate the strong equivalence principle (SEP) under both quantization choices, however these violations have been estimated to be too small to measure with present-day experiments [68]. More recently, its capacity to describe quantum effects of GW propagation on a classical background [69, 70] have yielded other potentially observable effects that will be the subject of this chapter.

## 6.1 Theory of polymer gravity

The derivation of polymer effects on GWs is subtle and involved, but serve only as context (crucial context, but context nonetheless) for the work presented here. We will briefly review the procedure for deriving polymer quantum corrections to GWs, but for more detailed treatments of polymer gravity please see Refs. [69, 70].

In chapter II, we added a small perturbation to a Minkowski metric and demonstrated that in the linear regime, the EFEs for those perturbations reduced to the familiar wave equation. The EFEs are obtained by varying the Einstein-Hilbert action to obtain the equations of motion (and constraint equation) for the dynamics of the spacetime metric. An equally valid approach to obtaining the EOMs describing the metric perturbations is to formulate a Hamiltonian describing the system to determine its dynamical equations.

Recall from chapter II, the Ricci scalar for the linear metric perturbations is

$$R = \partial_\mu \partial_\nu h^{\mu\nu} - \partial^\mu \partial_\mu h.$$

In terms of the transverse-traceless metric perturbation, $h_{\mu\nu} = h_{\mu\nu} - \frac{1}{2}\eta_{\mu\nu} h$, this simplifies to

$$R = \partial_\mu \partial_\nu \bar{h}^{\mu\nu} = \Box.$$

Substituting this into the Einstein-Hilbert action, we arrive at

$$S_{\mathrm{GW}} \simeq \frac{1}{8\kappa^2} \int d^4x \sqrt{-\eta}\, \bar{h}_{ij} \Box \bar{h}^{ij} \tag{6.1}$$

$$\tag{6.2}$$

From here, we can read off that the Lagrangian density at linear order for GWs is

$$\mathcal{L} = \frac{1}{8\kappa^2} \bar{h}_{ij} \Box \bar{h}^{ij}. \tag{6.3}$$

As a reminder, the transverse traceless perturbations in the Lorenz gauge propagating in a given direction such as $x^3$ can be decomposed into plus and cross polarizations,

$$\bar{h}_{ij}(x^0, x^3) = \bar{h}_+(x^0, x^3) e^+_{ij} + \bar{h}_\times(x^0, x^3) e^\times_{ij}. \tag{6.4}$$

The Lagrangian density can then be rewritten as a sum over polarizations of the TT perturbations:

$$\mathcal{L} = \frac{1}{2} \sum_{\lambda \in \{+, \times\}} \check{h}_\lambda \Box \check{h}_\lambda, \tag{6.5}$$

where we've rescaled the metric perturbations $\check{h}_\lambda \equiv \bar{h}_\lambda / 2\kappa$. The conjugate momentum for each polarization can be determined from 6.5:

$$\check{\pi}_\lambda \equiv \frac{\partial \mathcal{L}}{\partial \check{h}_\lambda} = \frac{1}{2} \sum_\lambda \Box \check{h}_\lambda \tag{6.6}$$

The metric perturbation and its conjugate momentum can be expressed in terms of its spatial Fourier modes and its conjugate momentum:

$$\check{h}_\lambda(x^0, \vec{x}) = \frac{1}{\ell^{3/2}} \sum_{\vec{k}\in\mathscr{L}} \mathfrak{h}_{\lambda,\vec{k}}(x^0) e^{i\vec{k}\cdot\vec{x}} \tag{6.7}$$

$$\check{\pi}_\lambda(x^0, \vec{x}) = \frac{1}{\ell^{3/2}} \sum_{\vec{k}\in\mathscr{L}} \Pi_{\lambda,\vec{k}}(x^0) e^{i\vec{k}\cdot\vec{x}}. \tag{6.8}$$

Here, the allowed values of the wavevector are assumed to be $\vec{k} = (k_1, k_2, k_3) \in (2\pi\mathbb{Z}/\ell)^3$ which span the discrete lattice space $\mathscr{L}$, where $\ell$ is the characteristic length scale of the corresponding configuration space.

As $\check{h}_\lambda$ and $\check{\pi}_\lambda$ are canonically conjugate, their Fourier modes are as well, and satisfy the standard commutation relations $\{\mathfrak{h}_{\lambda,\vec{k}}, \Pi_{\lambda,\vec{k}}\} = \delta_{\vec{k},-\vec{k}}$. Additionally, since the metric perturbation field must be real-valued, its Fourier coefficients must satisfy

$$\begin{aligned} \left( \frac{1}{\ell^{3/2}} \sum_{\vec{k}\in\mathscr{L}} \mathfrak{h}_{\lambda,\vec{k}}(x^0) e^{i\vec{k}\cdot\vec{x}} \right)^* &= \frac{1}{\ell^{3/2}} \sum_{\vec{k}\in\mathscr{L}} \mathfrak{h}_{\lambda,\vec{k}}(x^0) e^{i\vec{k}\cdot\vec{x}} \\ \Rightarrow \mathfrak{h}^*_{\lambda,\vec{k}}(x^0) e^{-i\vec{k}\cdot\vec{x}} &= \mathfrak{h}_{\lambda,\vec{k}}(x^0) e^{i\vec{k}\cdot\vec{x}} \\ \Rightarrow \mathfrak{h}^*_{\lambda,\vec{k}}(x^0) &= \mathfrak{h}_{\lambda,-\vec{k}}(x^0), \end{aligned}$$

where the Fourier modes of the conjugate momentum satisfy the analogous relations $\Pi^*_{\lambda,\vec{k}} = \Pi_{\lambda,-\vec{k}}$. The reality condition of the field motivates the decomposition of the Fourier components in terms of their real and imaginary components,

$$\mathfrak{h}_{\lambda,\vec{k}} = \frac{1}{\sqrt{2}} (\mathfrak{h}^{(1)}_{\lambda,\vec{k}} + i\mathfrak{h}^{(2)}_{\lambda,\vec{k}}), \tag{6.9}$$

$$\Pi_{\lambda,\vec{k}} = \frac{1}{\sqrt{2}} (\Pi^{(1)}_{\lambda,\vec{k}} + i\Pi^{(2)}_{\lambda,\vec{k}}), \tag{6.10}$$

which naturally motivates the segmentation of the lattice $\mathscr{L}$ into positive and negative sectors $\mathscr{L}_+$ and $\mathscr{L}_-$ respectively. This effectively splits the summation over $\vec{k}$ in the field decomposition into two summations over the positive and negative sectors of the lattice. Leveraging the complex decomposition of the fields' Fourier modes and the reality conditions placed on them, we define new dynamical field variables

$$\mathcal{A}_{\lambda,\vec{k}} \equiv \begin{cases} \mathfrak{h}^{(1)}_{\lambda,\vec{k}} & \text{for} \quad \vec{k} \in \mathscr{L}_+ \\ \mathfrak{h}^{(2)}_{\lambda,-\vec{k}} & \text{for} \quad \vec{k} \in \mathscr{L}_-, \end{cases} \tag{6.11a}$$

$$\mathcal{E}_{\lambda,\vec{k}} \equiv \begin{cases} \Pi^{(1)}_{\lambda,\vec{k}} & \text{for} \quad \vec{k} \in \mathscr{L}_+ \\ \Pi^{(2)}_{\lambda,-\vec{k}} & \text{for} \quad \vec{k} \in \mathscr{L}_-, \end{cases} \tag{6.11b}$$

which also satisfy canonical commutation relations $\{\mathcal{A}_{\lambda,\vec{k}}, \mathcal{E}_{\lambda',\vec{k}'}\} = \delta_{\lambda\lambda'}\delta_{\vec{k}\vec{k}'}$. With these definitions and Eqs. 6.5 and 6.9, the time-dependent Hamiltonian for the dynamical variables $\mathcal{A}_{\lambda,\vec{k}}$ and $\mathcal{E}_{\lambda,\vec{k}}$ are

$$H(x^0) = \frac{1}{2} \sum_{\lambda \in \{+,\times\}} \sum_{k \in \mathscr{L}} \left[ \mathcal{E}^2_{\lambda,\vec{k}} + k^2 \mathcal{A}^2_{\lambda,\vec{k}} \right]. \tag{6.12}$$

In order to introduce quantum mechanical effects into the dynamical variables $\mathcal{E}_{\lambda,\vec{k}}$ and $\mathcal{A}_{\lambda,\vec{k}}$, which represent the tensor metric perturbations and its conjugate momentum, we naturally promote them to operators and impose commutation relations on them. We consider two cases here, one in which $\mathcal{A}_{\lambda,\vec{k}}$ has discrete eigenvalues and $\mathcal{E}_{\lambda,\vec{k}}$ has no infinitesimal operator, and the reverse in which $\mathcal{E}_{\lambda,\vec{k}}$ has discrete eigenvalues and $\mathcal{A}_{\lambda,\vec{k}}$ has no infinitesimal operator. We will refer to these as "polymer $\mathcal{E}_{\lambda,\vec{k}}$" and "polymer $\mathcal{A}_{\lambda,\vec{k}}$" respectively. Each polymer quantization scheme obeys its own commutation relations:

$$\left[\hat{U}_{\lambda,\vec{k}}(\mu), \hat{\mathcal{A}}_{\lambda,\vec{k}}\right] = \hbar\mu\hat{U}_{\lambda,\vec{k}}(\mu) \qquad \text{(Polymer } \mathcal{E}_{\lambda,\vec{k}}\text{ )} \tag{6.13}$$

$$\left[\hat{V}_{\lambda,\vec{k}}(\nu), \hat{\mathcal{E}}_{\lambda,\vec{k}}\right] = -\hbar\nu\hat{V}_{\lambda,\vec{k}}(\nu), \qquad \text{(Polymer } \mathcal{A}_{\lambda,\vec{k}}\text{ )} \tag{6.14}$$

where $\hat{U}_{\lambda,\vec{k}}(\mu)$ is the generator of finite translations and $\hat{V}_{\lambda,\vec{k}}(\nu)$ is the generator for transformations in $\mathcal{E}_{\lambda,\vec{k}}$. The characteristic scales of each of the polymer quantizations $\mu$ and $\nu$ describe the discreteness of the observables $\mathcal{A}_{\lambda,\vec{k}}$ and $\mathcal{E}_{\lambda,\vec{k}}$ respectively. In the polymer $\mathcal{E}_{\lambda,\vec{k}}$ where $\mathcal{A}_{\lambda,\vec{k}}$–the dynamical variable for the spacetime perturbations–is the quantum observable, the characteristic scale $\mu$ can be interpreted as describing the quantum discreteness of spacetime. The Hamiltonians for the polymer fields now take the form

$$H^{(\mathcal{E})}_{\lambda,\vec{k}} = \frac{2}{\mu^2}\sin^2\left(\frac{\mu\mathcal{E}_{\lambda,\vec{k}}}{2}\right) + \frac{1}{2}\vec{k}^2\mathcal{A}^2_{\lambda,\vec{k}} \tag{6.15}$$

$$H^{(\mathcal{A})}_{\lambda,\vec{k}} = \frac{1}{2}\mathcal{E}^2_{\lambda,\vec{k}} + \frac{2}{\nu^2}\sin^2\left(\frac{\nu\mathcal{A}_{\lambda,\vec{k}}}{2}\right). \tag{6.16}$$

The corresponding equations of motion for these Hamiltonians are

$$\frac{d\mathcal{A}_{\lambda,\vec{k}}}{dt} = \mathcal{E}_{+,\vec{k}}, \qquad \frac{d\mathcal{E}_{\lambda,\vec{k}}}{dt} = -\frac{\hbar k^2}{\nu}\sin\left(\frac{\nu}{\hbar}\mathcal{A}_{\lambda,\vec{k}}\right) \qquad \text{(Polymer } \mathcal{A}\text{)}, \tag{6.17}$$

$$\frac{d\mathcal{A}_{\lambda,\vec{k}}}{dt} = \frac{\hbar}{\mu}\sin\left(\frac{\mu}{\hbar}\mathcal{E}_{\lambda,\vec{k}}\right), \qquad \frac{d\mathcal{E}_{\lambda,\vec{k}}}{dt} = -k^2\mathcal{A}_{\lambda,\vec{k}} \qquad \text{(Polymer } \mathcal{E}\text{)}. \tag{6.18}$$

To the leading order in both polymer $\mathcal{A}$ and polymer $\mathcal{E}$ cases, the plane-wave solutions to Eqs. 6.16 for plus-polarized metric perturbations [71] are

$$\begin{aligned}\bar{h}^{(\mathcal{A})}_{+,\mathbf{k}}(t) \;\approx\; \bar{h}_I \Bigg[&\left(1-\frac{\bar{h}_I^2\bar{\nu}^2}{96\,\hbar^2}\right)\cos\left(kc\sqrt{1-\frac{\bar{h}_I^2\bar{\nu}^2}{8\hbar^2}}\,t\right)\\ &-\frac{\bar{h}_I^2\bar{\nu}^2}{192\hbar^2}\cos\left(3kc\sqrt{1-\frac{\bar{h}_I^2\bar{\nu}^2}{8\hbar^2}}\,t\right)\Bigg].\end{aligned} \tag{6.19}$$

and

$$\begin{aligned}\bar{h}^{(\mathcal{E})}_{+,\mathbf{k}}(t) \approx \bar{h}_I \Bigg[&\left(1-\frac{\bar{h}_I^2\bar{\mu}^2k^2}{32\hbar^2}\right)\cos\left(kc\sqrt{1-\frac{\bar{h}_I^2\bar{\mu}^2k^2}{8\hbar^2}}\,t\right)\\ &-\frac{\bar{h}_I^2\bar{\mu}^2k^2}{64\hbar^2}\cos\left(3kc\sqrt{1-\frac{\bar{h}_I^2\bar{\mu}^2k^2}{8\hbar^2}}\,t\right)\Bigg],\end{aligned} \tag{6.20}$$

where we've introduced the reduced polymer scales

$$\bar{\nu} \equiv \frac{\nu\ell^{3/2}}{2\kappa} \qquad \text{(Polymer } \mathcal{A}\text{)} \tag{6.21}$$

$$\bar{\mu} \equiv \frac{\mu\ell^{3/2}}{2\kappa} \qquad \text{(Polymer } \mathcal{E}\text{)}. \tag{6.22}$$

In geometric units ($c = G = 1$), $\bar{\nu}$ is dimensionless and $\bar{\mu}$ has dimensions of length. As a reminder, $\ell$ is the length scale associated with the lattice $\mathcal{L}$. Also to linear order, the associated group velocities in each polymer case [71] are

$$v^{(\mathcal{A})} \approx v_{\mathrm{EM}} \left(1 - \frac{\bar{h}_I^2 \bar{\nu}^2}{16\hbar^2}\right), \tag{6.23}$$

$$v^{(\mathcal{E})} \approx v_{\mathrm{EM}} \left(1 - \frac{3\bar{h}_I^2 \bar{\mu}^2}{16\hbar^2} k^2\right). \tag{6.24}$$

Fascinatingly, under the polymer quantization, GWs have a reduced velocity relative to the propagation speed of the speed of light. Note that when examining travel times over a specific distance for GWs, this is an accumulated effect. For GWs traveling over a large distance, as is the case with all GW observations, even a small deviation in the propagation speed could yield observable travel time differences relative to those expected in the classically predicted case. This is a promising observable of polymer-corrected GWs. Methods for constraining the polymer-induced deviation in propagation speed of GWs will be the subject of the remainder of the chapter.

### 6.1.1 Constraining the polymer scale

In this section we outline the procedure for leveraging polymer scale dependent departures from the classical GW propagation speed to place constraints on the polymer scale. The deviation can be inferred from the equations for the group velocity Eqs. 6.23 and 6.24,

$$\Delta v^{\mathcal{A}} \approx -\frac{\bar{h}_I^2 \bar{\nu}^2}{16\hbar^2} \tag{6.25}$$

$$\Delta v^{\mathcal{E}} \approx -\frac{3\bar{h}_I^2 \bar{\mu}^2}{16\hbar^2} k^2. \tag{6.26}$$

Eqs. 6.25 and 6.26 imply any measurements of $\Delta v_g$ can be used to infer constraints on the polymer scale. While GWs produced from mergers of compact objects are not plane waves, this is an appropriate enough approximation by the time they reach a GW observatory on Earth.

Formally, the extracted probability distribution on the propagation speed is related to the distribution of polymer scales via a Jacobian transformation. Defining $U \in \{\bar{\nu}, \bar{\mu}\}$ The relationship between $p^{\{\mathcal{A},\mathcal{E}\}}(U)$ and $p(\Delta v_g)$ becomes

$$p^{\{\mathcal{A},\mathcal{E}\}}(U) = \left| \frac{\partial \Delta v_g}{\partial U^{\{\mathcal{A},\mathcal{E}\}}} \right| p(\Delta v_g). \tag{6.27}$$

Invoking Eqs. 6.25 and 6.26 to evaluate Eq. 6.27, we arrive at a set of simple relations between $p^{\{\mathcal{A},\mathcal{E}\}}$ and $p(\Delta v_g)$:

$$p^{\mathcal{A}}(\bar{\nu}) = \frac{\bar{h}_I^2 \bar{\nu}}{8\hbar^2}\, p(\Delta v_g), \qquad p^{\mathcal{E}}(\bar{\mu}) = \frac{3\bar{h}_I^2 \bar{\mu}}{8\hbar^2} k^2\, p(\Delta v_g) \tag{6.28}$$

for the probability distribution for two polymer quantization schemes.

In the following sections, we use constraints on $\Delta v_g$ from two independent approaches: The first relies on inter-detector arrival time differences for signals detected in multiple GW observatories, while the second compares the arrival time difference between multimessenger GW signals and their electromagntic counterpart. We apply this procedure to event GW170817 and its associated gamma ray burst (GRB), GRB170817A [72], as this is so far the only existing confident multimessenger detection.

### 6.1.2 Pure GW constraints

The constraints in this section rely on the posterior samples for $\Delta v_g$ generously provided by the authors of [73]. We will first briefly review the method used in their work to obtain the posterior samples on $\Delta v_g$ before discussing how these samples can be used to estimate $p^{\mathcal{A}}(\bar{\nu})$ and $p^{\mathcal{E}}(\bar{\mu})$.

Gravitational wave signals detected in multiple GW observatories separated from each other by some distance will appear in each observatory at different times. With precise knowledge of the distance between detectors and measurements of the signal arrival time in each detector, one can estimate the average propagation velocity of the GW between the detectors. As we've discussed, the Bayesian posterior of the coalescence time of the GW, along with that of all other model parameters, can be estimated using the techniques discussed in Chapters 4 and 5. Typically, $t_c$ samples are generated in the geocenter frame and then used to compute a detector-specific arrival time by assuming a fixed propagation speed of $v_g = v_{\mathrm{EM}}$. In [73], however, $v_g$ is incorporated as an additional sampled parameter. Analysis of the eleven events in GWTC1, which were all observed in at least two detectors, yield posterior samples representing 11 independent measurements of $v_g$, or equivalently $\Delta v_g \equiv v_g - v_{\mathrm{EM}}$. Assuming all GWs propagate at the same speed (which is not necessarily $v_{\mathrm{EM}}$, the PDFs can be combined according to

$$p(\Delta v_g|d_1, d_2, \ldots) \propto p(\Delta v_g|d_1)p(\Delta v_g|d_2)\ldots p(\Delta v_g|d_n), \tag{6.29}$$

where $d_i$ is the data associated with the $i^{\mathrm{th}}$ GW observation. From this point, the resulting PDFs on polymer scales $\bar{\nu}$ and $\bar{\mu}$ can be computed using Eqs. 6.28.

### Results

Fig. 6.1 shows the PDF for $\Delta v_g$ for all events in GWTC1 [16] composed of 10 BBH events as well as GW170817, the lone BNS event. We combine information constraining $\Delta v_g$ from all events and apply the methods outlined in section 6.1.1. The resulting combined as well as per-event constraints on the polymer scale for each of the two polymer quantization choices in Figs. 6.2, 6.3.

As the polymer scales in both cases must be real, a hard cut prior is placed on all $\Delta v_g$ samples greater than 0, and remove any events with too few posterior samples to produce reliable PDFs. While Eqs. 6.28 are general for any PDF $p(\Delta v_g)$, by only allowing for negative values of $\Delta v_g$, we estimate the conditional PDFs $p^{\mathcal{A}}(\bar{\nu}|\Delta v_g < 0)$ and $p^{\mathcal{E}}(\bar{\mu}|\Delta v_g < 0)$. We combine information from the kernel-density-estimated (KDE) PDFs on $\Delta v_g$ for each event using Eq. 6.29. The shape of the resulting combined PDF

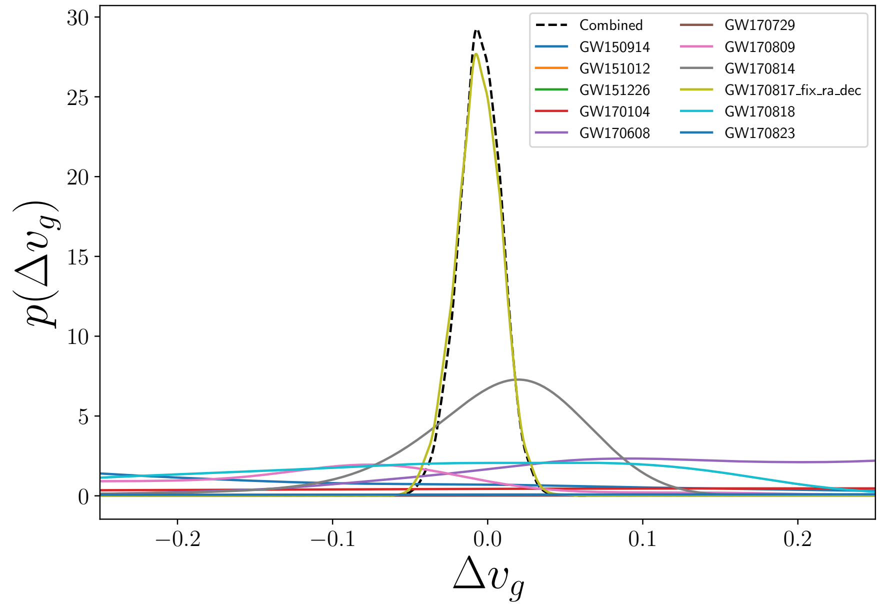

(a) Posterior density functions on parameter $v_g$ estimated for each event in GWTC1 as well as combined measurement from all events. Combined measurement assumes sky location for GW170817 is estimated without calibration from GRB170817A.

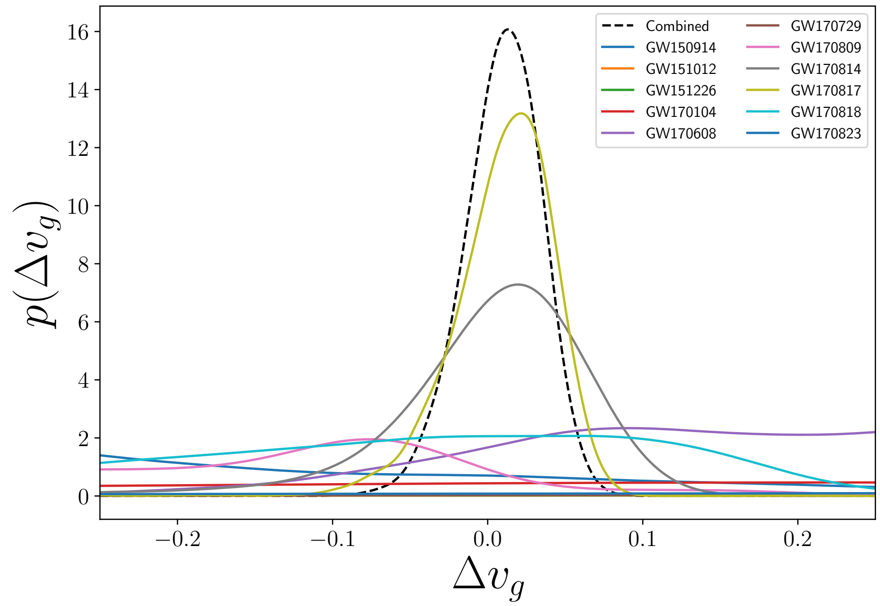

(b) Posterior density functions on parameter $v_g$ estimated for each event in GWTC1 as well as combined measurement from all events. Combined measurement assumes sky location for GW170817 is calibrated to its associated gamma-ray burst GRB170817A.

Figure 6.1: KDE-estimated combined and individual-event PDFs on $\Delta v_g$ from posterior samples for all GWTC1 events provided by Ref. [73]. Fig. 6.1a fixes the sky location parameters, $\alpha$ and $\delta$, to be those inferred from the associated gamma-ray burst GRB170817A while Fig. 6.1b relies on information from the GW signal only.

on $\Delta v_g$ is highly dependent on the most informative event, GW170817, whose PDF is in turn also dependent on what sky localization information is assumed. The sky location of GRB170817A, the gamma-ray burst associated with GW170817, is much more precisely measured than the sky location inferred purely from the GW signal and has a significant effect on the shape of the PDF of $\Delta v_g$ for that event. We therefore show the combined $\Delta v_g$ posterior for two cases: one in which the sky location for GW170817 is fixed to the GRB170817A-inferred values during analysis of the GW signal (Fig. 6.1a), and one in which the right ascension and declination, $\alpha$ and $\delta$, are allowed to vary and are inferred purely from information contained in the GW signal. The probability that $\Delta v_g$ is less than 0 as measured from the combined PDF under each of these two assumptions are as follows:

$$P_{\text{fix}}(\Delta v_g < 0) = \int_{-\infty}^{0} d\Delta v_g \;\; p_{\text{fix}}(\Delta v_g) = 0.63 \qquad \text{(GW170817} \;\; \alpha, \delta \;\; \text{fixed)} \tag{6.30}$$

$$P_{\text{vary}}(\Delta v_g < 0) = \int_{-\infty}^{0} d\Delta v_g \;\; p_{\text{vary}}(\Delta v_g) = 0.33 \qquad \text{(GW170817} \;\; \alpha, \delta \;\; \text{varied).} \tag{6.31}$$

Therefore when the sky location parameters for GW170817 are fixed to more precise values, it becomes nearly twice as likely that GWs travel slower than speed of light.

Eqs. 6.28 require as inputs the initial GW amplitude, $\bar{h}_I$ for both cases and the gravitational wavenumber $k$ for polymer $\mathcal{E}$. While the dependence of $\Delta v_g$ on the wavenumber is fascinating and could potentially improve constraints when spectral information is taken into account, we leave this to future work. For now, we take $k$ to be the wavenumber at merger.

To estimate the quantities $\bar{h}_I$ and $k$, we take the maximum posterior point associated with each model parameter, evaluate the waveform model `IMRPhenomPv2` at these points, and inject the signal into simulated GW detectors with PSDs estimated from public strain data near the coalescence time of–but not overlapping with–each GW event. We then record the maximum strain value at merger and estimate the frequency at merger from the last waveform cycle before merger. The wavenumber is then calculated from the

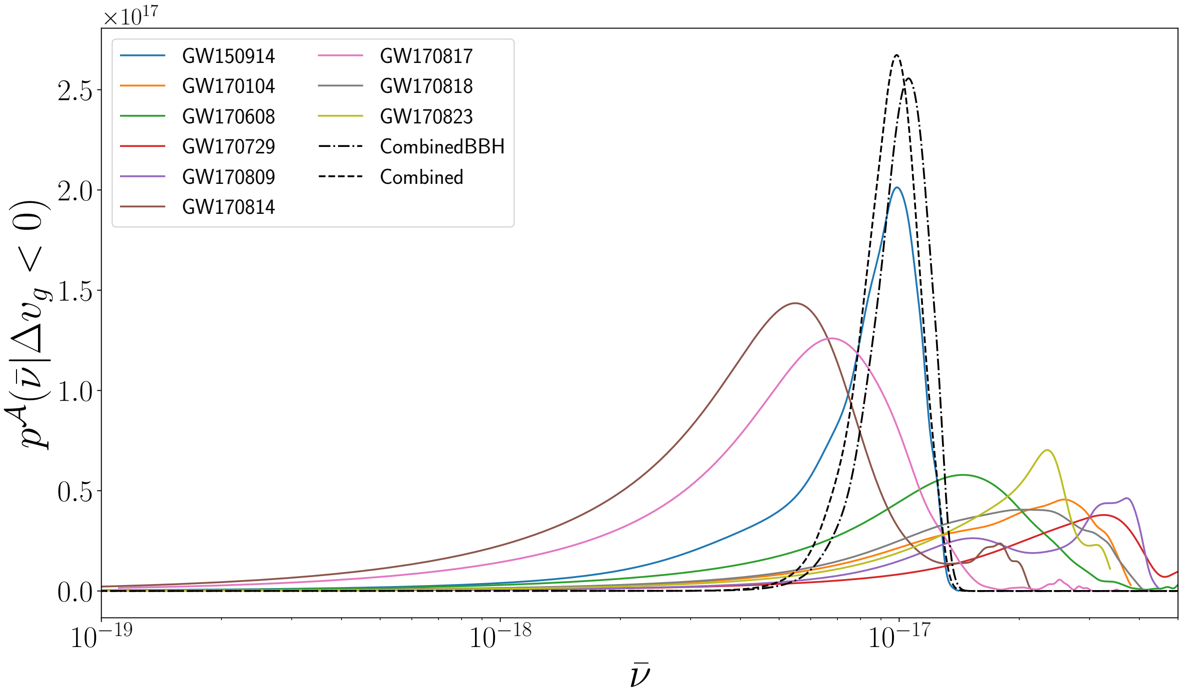

(a) Constraints on polymer scale $\bar{\nu}$ from gravitational-wave detections from LIGO's first and second observing runs.

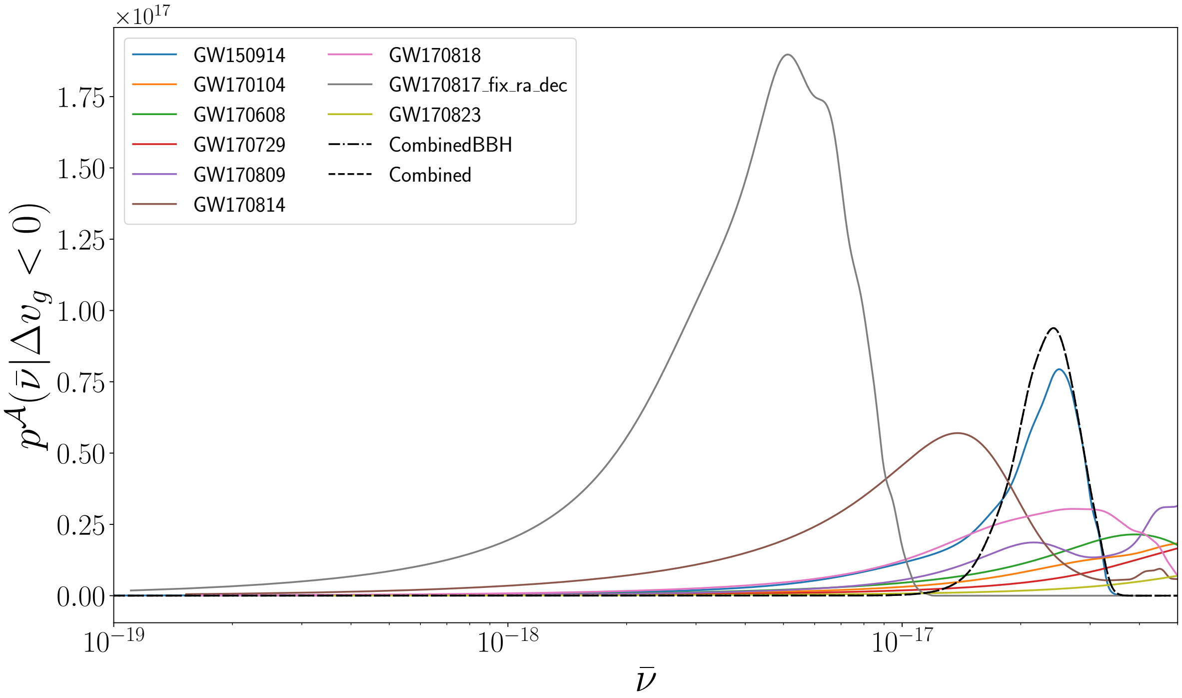

(b) Constraints on polymer scale $\bar{\nu}$ from gravitational-wave detections from LIGO's first and second observing runs. Sky localization parameters were fixed to the GRB170817A-inferred values during parameter inference of GW170817.

Figure 6.2: Posterior probability density functions on polymer parameter $\bar{\mu}$. All events used for analysis are from the LVC's first gravitational-wave transient catalog paper (GWTC1). In Fig. 6.3b the sky localization parameters for event GW170817 were fixed to the GRB170817A-inferred values during parameter inference.

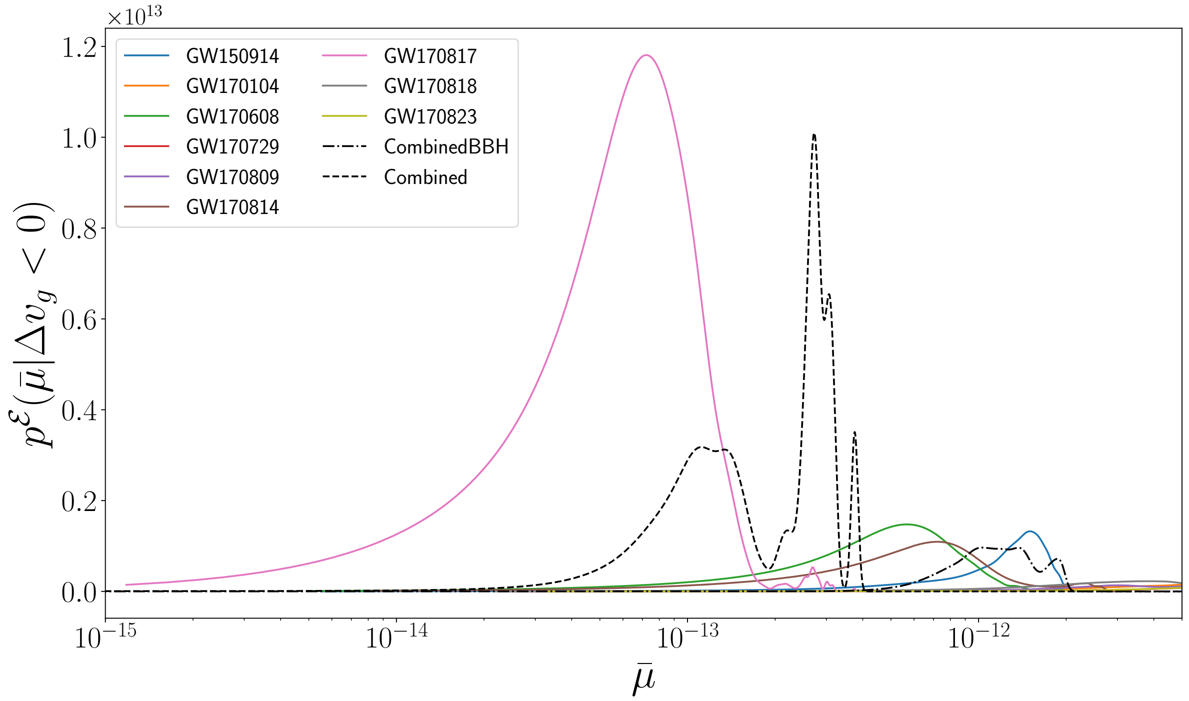

(a) Constraints on polymer scale $\bar{\mu}$ from gravitational-wave detections from LIGO's first and second observing runs.

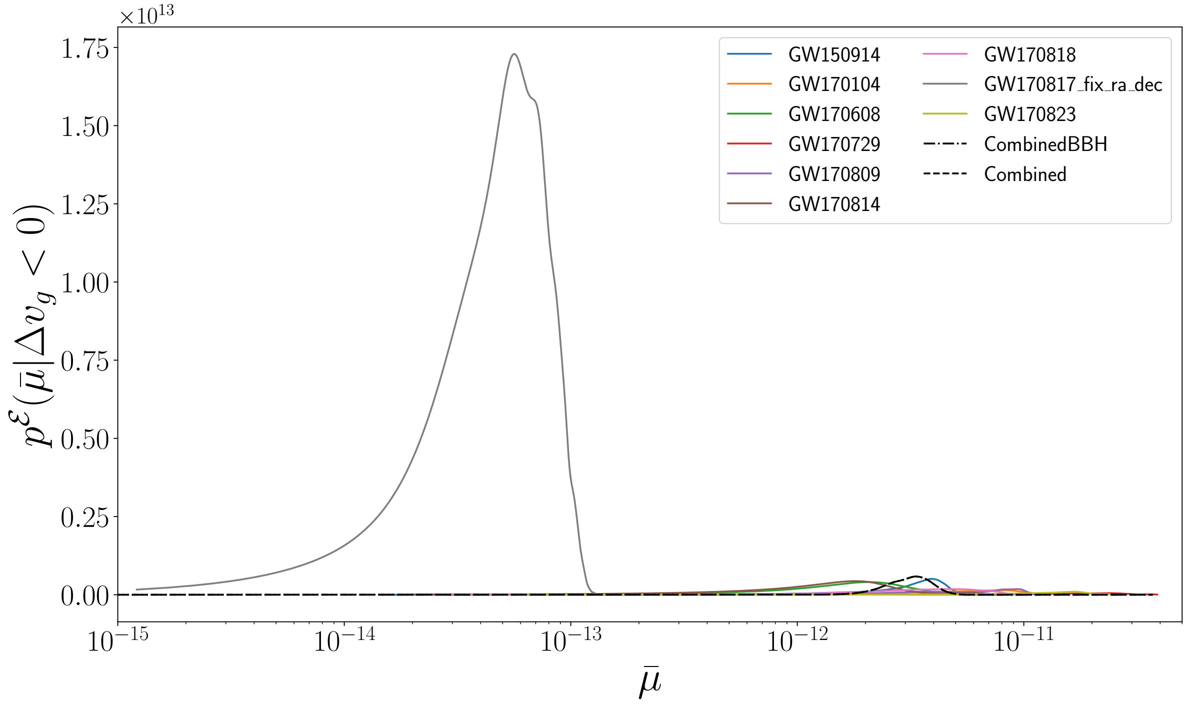

(b) Constraints on polymer scale $\bar{\mu}$ from gravitational-wave detections from LIGO's first and second observing runs. Sky localization parameters were fixed to the GRB170817A-inferred values during parameter inference of GW170817.

Figure 6.3: Posterior probability density functions on polymer parameter $\bar{\mu}$. All events used for analysis are from the LVC's first gravitational-wave transient catalog paper (GWTC1). In Fig. 6.3b the sky localization parameters for event GW170817 were fixed to the GRB170817A-inferred values during parameter inference.

| Events | $\max(\Delta v_g)$ | $\bar{\nu}(/10^{-17})$ $\mathrm{kg \cdot m^2/s}$ | $\nu(/10^{-53})$ $\mathrm{kg^{1/2}}$ | $\bar{\mu}(/10^{-12})$ $\mathrm{kg \cdot m^2}$ | $\mu(/10^{-48})$ $\mathrm{kg^{1/2} \cdot s}$ | GW strain at Peak | frequency at peak Hz | SNR |
|---|---|---|---|---|---|---|---|---|
| GW150914 | $-0.39^{+0.48}_{-0.16}$ | $0.99^{+0.16}_{-0.45}$ | $0.9^{+0.15}_{-0.41}$ | $1.50^{+0.25}_{-0.68}$ | $1.37^{+0.23}_{-0.62}$ | $1.6\times10^{-21}$ | 181 | 24.4 |
| GW170104 | $0.23^{+1.90}_{-0.54}$ | $2.60^{+0.64}_{-1.56}$ | $2.37^{+0.58}_{-1.42}$ | $6.63^{+1.63}_{-0.40}$ | $6.05^{+1.49}_{-3.63}$ | $5.9\times10^{-22}$ | 108 | 13.0 |
| GW170608 | $0.88^{+2.40}_{-1.50} \times 10^{-1}$ | $1.45^{+1.19}_{-0.70}$ | $1.32^{+1.09}_{-0.63}$ | $0.57^{+0.47}_{-0.27}$ | $0.52^{+0.43}_{-0.25}$ | $4.4\times10^{-22}$ | 702 | 14.9 |
| GW170729 | $3.13^{+1.35}_{-2.00}$ | $3.26^{+1.05}_{-1.73}$ | $2.97^{+0.96}_{-1.58}$ | $8.95^{+2.89}_{-4.76}$ | $8.15^{+2.64}_{-4.34}$ | $4.1\times10^{-22}$ | 100 | 10.8 |
| GW170809 | $-0.79^{+0.45}_{-5.61}\times10^{-1}$ | $3.72^{+0.17}_{-2.47}$ | $3.39^{+0.16}_{-2.24}$ | $7.28^{+0.34}_{-4.85}$ | $6.64^{+0.31}_{-4.42}$ | $5.0\times10^{-22}$ | 141 | 12.4 |
| GW170814 | $0.17^{+0.51}_{-1.25} \times 10^{-1}$ | $0.55^{+0.99}_{-0.26}$ | $0.50^{+0.90}_{-0.24}$ | $0.72^{+1.30}_{-0.35}$ | $0.66^{+1.17}_{-0.32}$ | $9.6\times10^{-22}$ | 210 | 15.9 |
| GW170817 | $1.88^{+2.68}_{-5.53} \times 10^{-2}$ | $0.68^{+0.0.53}_{-0.33}$ | $0.62^{+0.48}_{-0.30}$ | $0.07^{+0.06}_{-0.03}$ | $0.07^{+0.05}_{-0.03}$ | $5.3\times10^{-22}$ | 2582 | 33.0 |
| GW170818 | $0.51^{+0.89}_{-4.20} \times 10^{-1}$ | $2.04^{+1.23}_{-1.06}$ | $1.86^{+1.12}_{-0.96}$ | $3.69^{+2.22}_{-1.91}$ | $3.36^{+2.03}_{-1.74}$ | $4.9\times10^{-22}$ | 152 | 11.3 |
| GW170823 | $1.96^{+8.73}_{-1.41}$ | $2.35^{+0.54}_{-1.24}$ | $2.14^{+0.50}_{-1.13}$ | $8.76^{+2.02}_{-4.64}$ | $7.99^{+1.84}_{-4.23}$ | $6.6\times10^{-22}$ | 74 | 11.5 |
| Combined (BBH) | $0.09^{+5.73}_{-5.45} \times 10^{-2}$ | $1.06^{+0.17}_{-0.23}$ | $0.96^{+0.15}_{-0.21}$ | $1.03^{+0.82}_{-0.21}$ | $0.94^{+0.75}_{-0.20}$ | | | |
| Combined | $1.30^{+2.76}_{-3.63} \times 10^{-2}$ | $0.99^{+0.18}_{-0.22}$ | $0.90^{+0.16}_{-0.20}$ | $0.27^{+0.05}_{-0.17}$ | $0.25^{+0.05}_{-0.15}$ | | | |

Table 6.1: Locations of maximum a posteriori values of $\Delta v_g$, $\bar{\nu}$ and $\bar{\mu}$ for all the events and calculated corresponding polymer parameters in their reduced form $\nu$ and $\mu$. Uncertainties listed are calculated to the 90% credible level. To have a better upper bound estimates for the polymer parameters, we use the frequency and strain of the peak of inspiral phase. The required length scale $\ell$ for the binary system is set to $10^{10}m$, larger wavelengths are ignored and could be absorbed in the homogeneous background, because we assume our system is localized.

classical dispersion relation where any non-zero graviton mass is taken to be negligible. When evaluating Eq. 6.28, $\bar{h}_I$ and $k$ are averaged over the observatories in which the signals were detected. The values for $\bar{h}_I$ and $k$ for each of the events are listed in Table 6.1.

The posterior density functions on the polymer scales $\bar{\nu}$ and $\bar{\mu}$ for all events are displayed in Figs. 6.2 and 6.3. The combined posterior is computed for both GW170817 sky localization cases discussed above. In addition to the estimations for maximum strain and frequency at merger, the maximum posterior values for $\Delta v_g$, the reduced-form polymer scales $\bar{\nu}$, $\bar{\mu}$ and their standard forms $\nu$ and $\mu$, are listed in Table 6.1 along with upper and lower bounds at the 90% credible level. Virtually all PDFs of $\bar{\nu}$ differ from those of $\bar{\mu}$ by 3-4 orders of magnitude, reflecting the impact of Eq. 6.26's dependence on the wavenumber $k$ of the GW. As expected, we find the combined measurement is dominated by the contribution from GW170817 regardless of the choice of sky localization prior, especially so when the fixed $\alpha$, $\delta$ priors are chosen. In this case, the combined measurement on $\bar{\nu}$ and $\bar{\mu}$ were

$$\hat{\bar{\nu}}_{\Delta v_g<0} = 1.44^{+0.27}_{-0.30} \times 10^{-13} \tag{6.32}$$

$$\hat{\bar{\mu}}_{\Delta v_g<0} = 0.14^{+0.03}_{-0.06} \times 10^{-8}. \tag{6.33}$$

### 6.1.3 Multimessenger Constraints

The coincident detection of GWs produced by the merger of two neutron stars, GW170817, and its accompanied gamma-ray burst, GRB170817A, provide another opportunity to constrain the propagation speed of GWs relative to that of EM radiation. Any observed difference between the arrival times of the two signals, with knowledge of the distance to the common source, can be used to infer the average propagation speed over the distance traveled. Given previous discussion about the polymer-quantized EM sector, a natural question arises: If both EM and GW radiation are polymer-quantized, why should we expect a relative propagation speed difference between a GW and GRB emitted from the same source? Thankfully, the polymer-induced time delay is not the same in both cases, as reflected in Eqs. 6.23, 6.24 and Eq. 21 of Ref. [62]. While both have quadratic dependencies on the polymer scale at first order, their dependencies on the frequencies and amplitudes of the signals take on distinct forms.

Following the procedure of [72], deviations from the classically predicted group velocity of GWs can be derived from measurements of the time delay between coincident GW and electromagnetic signals,

$$\frac{\Delta v_g}{v_{\mathrm{EM}}} \approx v_{\mathrm{EM}} \frac{\Delta t}{d_L}, \tag{6.34}$$

where $\Delta t$ is the time delay between the two signals, and $d_L$ is the luminosity distance to the source.

For a typical BBH signal, $d_L$ is roughly 19 orders of magnitude larger than the distance between LIGO Livingston and LIGO Hanford. This means any discrepancy between the GW and EM propagation speeds has a significantly larger distance over which to accumulate a time delay $\Delta t$. The result is a significantly more precise measurement of $\Delta v_g$ than when considering only intra-network time delays, and thus a more precise measurement of the polymer scales. Unfortunately, it's currently unclear whether or not the GW and EM signals are emitted at the same time at the source. This means the observed time delay $\Delta t_{\text{obs}}$ is really a sum of the time delay associated with the polymer-induced propagation speed deviation and the "lag" time between the emission of the signals at source,

$$\begin{aligned}\Delta t_{\text{obs}} &= \Delta t_{\text{poly}} + \Delta t_{\text{lag}} && (6.35)\\ &= \frac{\Delta v_g}{v_{\text{EM}}} \frac{d_L}{v_{\text{EM}}} + \Delta t_{\text{lag}}, && (6.36)\end{aligned}$$

where we've used Eq. 6.34 in the second line, attributing the entire physical time delay to polymer effects.

The primary drawback of this approach is the model-dependence introduced by $\Delta t_{\text{lag}}$. For their lower bound estimate, Ref. [72] assumes a 10s lag between the emission of the source's gravitational radiation and its associated GRB, though other models suggest significantly longer lags [74, 75] that can extend out to $\sim$ 1000s. Therefore the precision gained by measuring over a larger distance is washed out by the systematic error introduced by $\Delta t_{\text{lag}}$. Initially, we assume $\Delta t_{\text{lag}}$ is perfectly known and adopt a specific value, however later on we will explore our results' dependence on this assumption.

We take both $d_L$ and $\Delta t_{\text{obs}}$ to be random variates, where $p(d_L)$ is approximated from the publicly available posterior samples produced from LIGO parameter estimation analysis. The distribution $p(\Delta t)$ is instead assumed to be normally distributed with expectation value $E[\Delta t] = 1.74$ s and standard deviation $\sigma = 0.05$ s in accordance with [72]. We adopt $\Delta t_{\text{lag}} = 3.48$ s , which is equivalent to simultaneous signal emission with polymer effects inducing a 1.74 s lag in the GW arrival time over the distance traveled by both signals. The resulting distribution on $\Delta v_g$ can then be computed by integrating over the joint probability density function on the two variables,

$$p\left(\Delta v_g\right) = \int_{-\infty}^{\infty} |d_L| p_{\Delta t}\left(\Delta v_g d_L\right) p_{d_L}(d_L) d(d_L), \tag{6.37}$$

where $v_{\text{EM}}$ has been set to 1, and $p_{\Delta t}(\Delta t_{\text{poly}})$ is the distribution describing a newly defined random variate $\Delta t_{\text{poly}} = \Delta t_{\text{obs}} - \Delta t_{\text{lag}}$. Since we take the lag to be known precisely, the distribution describing $\Delta t_{\text{poly}}$ is identical to that describing $\Delta t_{\text{obs}}$ shifted by a factor of $\Delta t_{\text{lag}}$. The polymer scale distribution is then calculated from $p(\Delta v_g)$ according to section 6.1.1.

### Results

The PDF on the luminosity distance to the source of GW170817 is estimated from posterior samples provided in the LVC's public data release[1]. Assuming a normally distributed $\Delta t_{\text{obs}}$ as described above with $\Delta t_{\text{lag}} = 3.48$ s, the posterior distribution on $\Delta v_g$ is computed from the ratio distribution according to Eq. 6.37 and is displayed in Fig. 6.4. It should be noted that for this event, the choice of spin prior is particularly important. Higher spin values allow for the component neutron stars to sustain higher masses, a parameter which is degenerate with luminosity distance at the level of the gravitational waveform. However, even the most highly spinning neutron stars detected have modest dimensionless spin magnitudes and those that will merge in a Hubble time will have dimensionless spin magnitudes $a \lesssim 0.04$. Consistent with the analysis presented in the previous chapter, we analyze GW170817 under two spin priors. Fig. 6.4 shows two posterior density functions on $\Delta v_g$, corresponding to two choices of spin prior: one which restricts the spin parameters to low values, and one which assumes all values of the spin parameters are equally likely. For more details on these prior choices, please see the previous chapter and Ref. [48]. Finally, the resulting PDF on the dimensionless polymer scale under the two polymer quantization schemes is computed following the

---

[1] Official posterior samples for all source parameters, including $d_L$, can be found on the GW170817 GWOSC page.

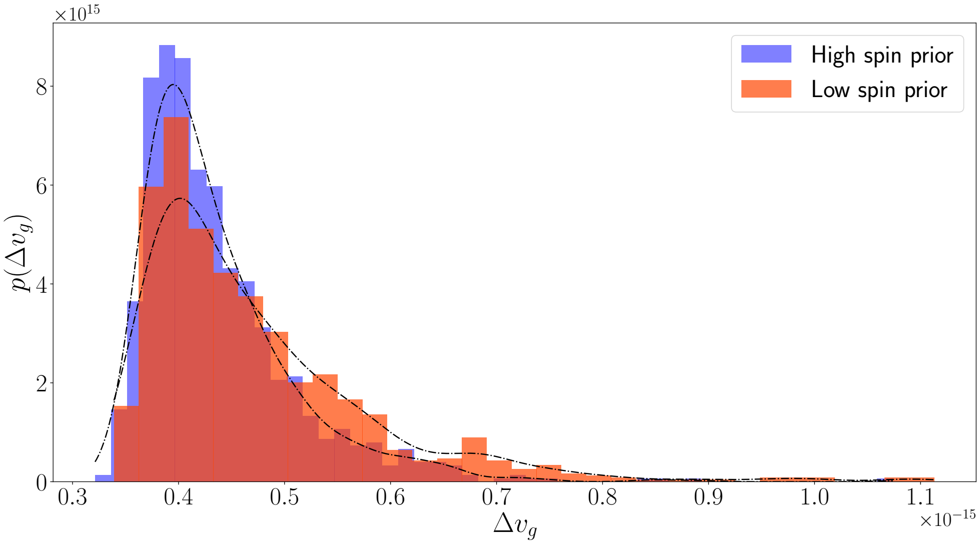

Figure 6.4: Constraints on departure from classically predicted propagation speed of gravitational waves. Calculated based on estimates of luminosity distance to the source and time delay between GW170817 and GRB170817A.

| Spin prior | $\Delta v_g(/10^{-16})$ | $\bar{\nu}(/10^{-13})$ | $\nu(/10^{-34})$ $m^{-1/2}$ | $\bar{\mu}(/10^{-8})$ | $\mu(/10^{-30})$ $m^{1/2}$ | GW strain at Peak | frequency at peak Hz | SNR |
|---|---|---|---|---|---|---|---|---|
| High spin | $3.93^{+1.53}_{-0.27}$ | $2.91^{+0.55}_{-0.10}$ | $2.92^{+0.52}_{-0.10}$ | $3.03^{+0.57}_{-0.11}$ | $3.03^{+0.54}_{-0.11}$ | $5.3\times10^{-22}$ | 2582 | 33 |
| Low spin | $4.02^{+2.20}_{-0.35}$ | $2.92^{+0.68}_{-0.11}$ | $2.94^{+0.73}_{-0.12}$ | $3.11^{+0.73}_{-0.11}$ | $3.13^{+0.77}_{-0.13}$ | $5.4\times10^{-22}$ | 2652 | 33 |

Table 6.2: Locations of maximum a posteriori values of $\Delta v_g$, $\bar{\nu}$ and $\bar{\mu}$ for GW170817 and corresponding polymer parameters in their reduced form $\nu$ and $\mu$. Uncertainties listed are calculated to the 90% credible level.

methods described in sections 6.1.1 and 6.1.3, displayed in Figs. 6.5. When converting from $\Delta v_g \to \{\bar{\nu}, \bar{\mu}\}$, we use the estimates for the merger strain and frequency at merger from the previous section for GW170817 without fixing the sky location parameters. For details on this process please see the previous section.

The dependence of polymer constraints on the assumption of time delay between GW signal emission and GRB emission is displayed in Figs. 6.6a, 6.6b for both polymer quantization schemes and both choices for the spin prior on $d_L$. The point statistic estimates for the $\Delta v_g$ and the polymer scales (analogous to Table 6.1 for multimessenger constraints) are listed in Table 6.2. As with Figs. 6.2 and 6.3, the measurement for $\bar{\mu}$ is roughly four orders of magnitude larger than that of $\bar{\nu}$, reflecting the dependence

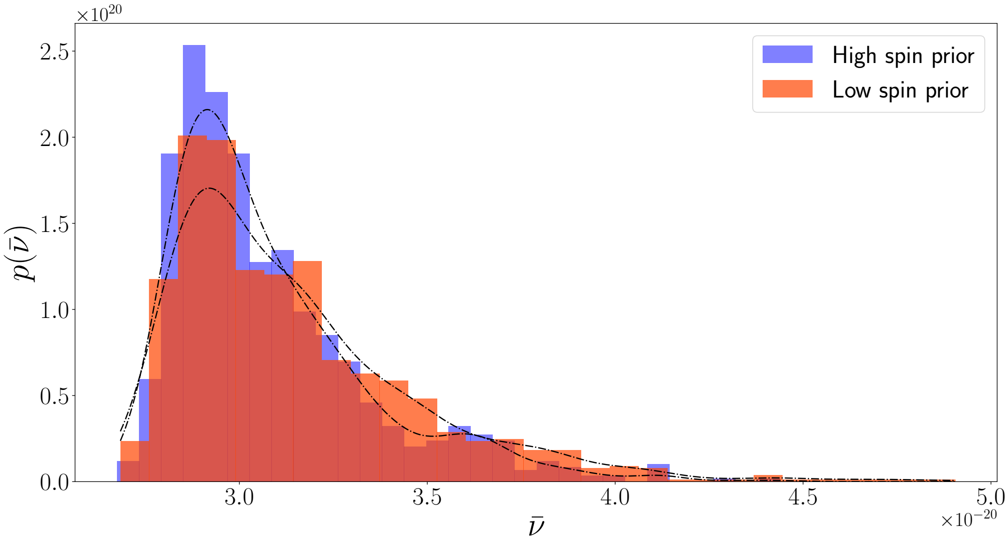

(a) Constraints on the polymer scale $\bar{\nu}$ inferred from the time delay between GRB170817A and GW170817.

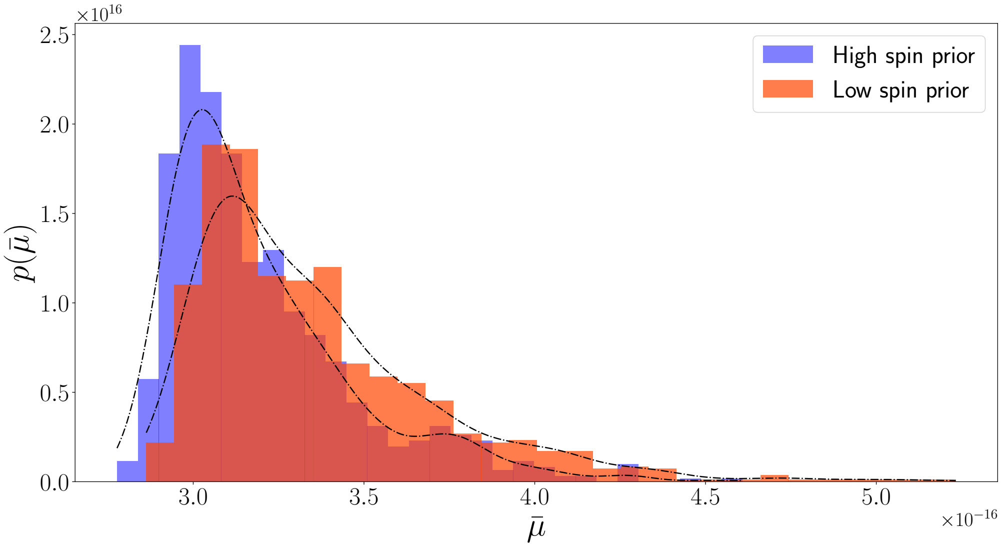

(b) Constraints on the polymer scale $\bar{\mu}$ inferred from the time delay between GRB170817A and GW170817.

Figure 6.5: Constraints on dimensionless polymer scale from coincident detections of GW170817 and GRB 170817A. The time delay between emission of the two signals is assumed to be Gaussian distributed with expectation value $E[\Delta t] = 1.74$ s and standard deviation $\sigma = 0.05$ s. The results for two priors on the neutron stars' spins are shown: one which disallows high spin values, and one which assumes all spin values are equally likely.

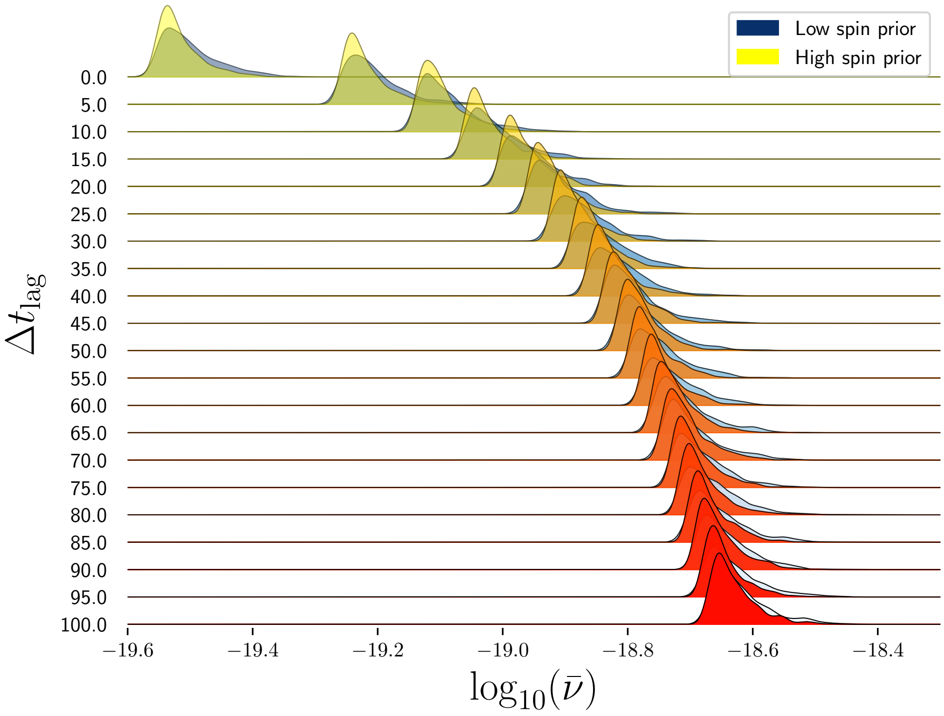

(a) Dependence of $p^{\mathcal{A}}(\bar{\nu})$ on the lag between signal emission, $\Delta t_{\mathrm{lag}} \equiv t_{0,\mathrm{GW}} - t_{0,\mathrm{EM}}$.

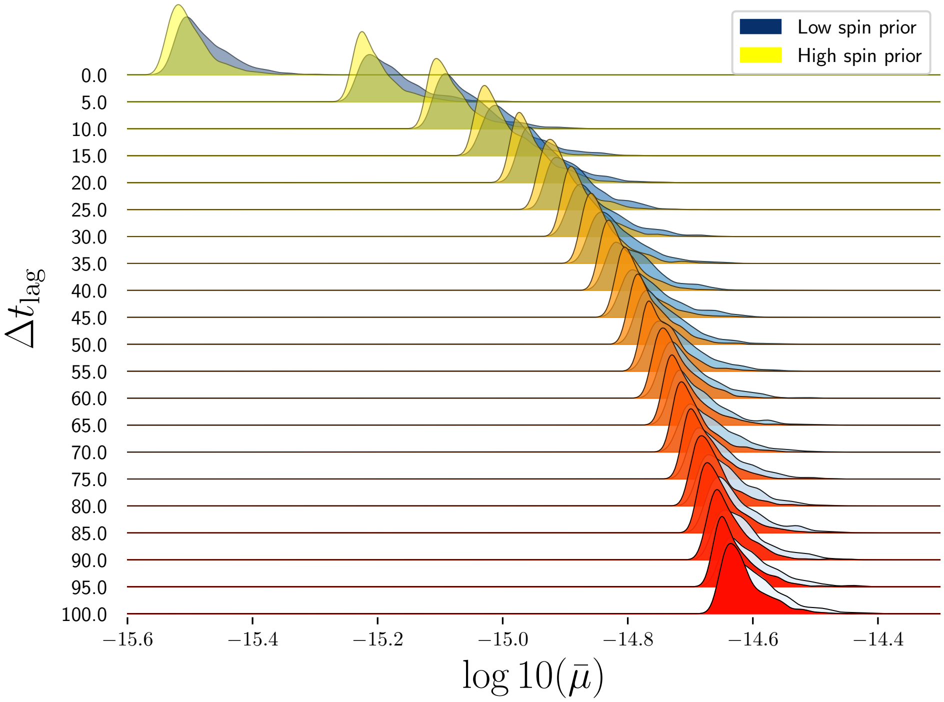

(b) Dependence of $p^{\mathcal{E}}(\bar{\mu})$ on the lag between signal emission, $\Delta t_{\mathrm{lag}} \equiv t_{0,\mathrm{GW}} - t_{0,\mathrm{EM}}$.

Figure 6.6: Dependence of polymer scale PDFs as a function of the lag time between emissions of GW signal GW170817 and gamma-ray burst signal GRB170817A.

of $\Delta v_g$ on the wavenumber in the polymer $\mathcal{E}$ case. The overall scale of the polymer parameters in both polymer quantization schemes is roughly $\sim 7$ orders of magnitude smaller than those from the inter-detector time delay constraints. This difference is almost entirely a function of the systematic uncertainty in $\Delta t_{\text{lag}}$. While the PDFs inferred from inter-detector time delays will likely see improvements in accuracy with additional GW detections, the constraints presented here from the multimessenger observations of GW170817 and GRB170817A may not improve in accuracy with additional detections until $\Delta t_{\text{lag}}$ is modeled accurately. To explore how multimessenger estimates of the polymer scale are affected by $\Delta t_{\text{lag}}$, we compute the PDFs on the polymer scale for 20 values of the lag, displayed in Figs. 6.6a and 6.6b.

In both cases, the means of the PDFs stay roughly within one order of magnitude of each other for lags ranging over 100s. However, it should be noted that the dependence of the PDFs on $\Delta t_{\text{lag}}$ is not asymptotic. This can be seen analytically by inverting Eqs. 6.23 and 6.24,

$$\bar{\nu}(\Delta v_g) = \frac{4\hbar}{\bar{h}_I}\sqrt{-\Delta v_g} \tag{6.38}$$

$$\bar{\mu}(\Delta v_g) = \frac{4\hbar}{\sqrt{3}\bar{h}_I k}\sqrt{-\Delta v_g}, \tag{6.39}$$

we see that with

$$\Delta v_g = \frac{\Delta t_{\text{poly}}}{d_L} = \frac{\Delta t_{\text{obs}} - \Delta t_{\text{lag}}}{d_L}, \tag{6.40}$$

the dependence of the polymer scales on the lag time is $\bar{\nu}, \bar{\mu} \sim \sqrt{\Delta t_{\text{lag}}}$. Therefore increasing the lag time will continue to increase the location of the polymer scale PDF.

### Conclusion

In this chapter, we present the first constraints on the scales describing quantum corrections to GWs under the polymer quantization scheme. The constraints are computed from PDFs on the propagation speed of GWs as inferred from GW observations and the observation of GRB170817 using two independent techniques. In the first, differences in arrival times of GWs in multiple detectors are used to infer the average velocity of the GWs over the distance between GW observatories. While the computed PDFs on the polymer scales are conditional on the GWs propagating slower than EM radiation, the associated probability of this occurring under the the GW-inferred PDF on $\Delta v_g$ is roughly 63%. This method is largely model independent and can be improved with additional high-SNR events which are currently available–a subject of future work.

The second approach uses the arrival time delay between GW170817 and its associated gamma-ray burst GRB170817A. While the PDFs under these two methods disagree by roughly $\sim 7$ orders of magnitude, this is largely due to systematic uncertainty in the knowledge of the lag time between emission of the GW and EM signals. We explore this dependency and conclude that improved models of GRB emission are needed before a conclusive measurement of $\Delta v_g$ is achieved using this method.

Most literature surrounding polymer quantization assumes the EM and gravity sectors are consistently quantized, however evidence to support this assumption is difficult to come by given quantum gravity remains largely a mystery. As the results reported here are the first empirical constraints on the polymer scale for GWs, we are forced to adopt this assumption in order to compare with previous results, which have only probed the polymer nature of the EM sector.

Ref. [62] quotes bounds on the dimensionless polymer scale of $\tilde{\mu} \equiv \mu/\Lambda_c^2 < 10^{-35}$, where $\Lambda_c$ is the energy cutoff scale introduced to maintain a countable number of polymer field Fourier modes. In natural units, the analogous dimensionless polymer scale is the quantity $\mu/\ell^{1/2}$, where as a reminder, $\ell$ is the intrinsic length scale of the quantization, chosen to be $10^{10}$ m. The inter-detector delay constraints yield $\mu/\ell^{1/2} \sim \mathcal{O}(10^{-24})$. When using time delays between GW170817 and its GRB counterpart, we find $\mu/\ell^{1/2} \sim \mathcal{O}(10^{-28})$. Both of the constraints on the polymer scale in the gravitational sector suggest higher values than those from GRB090510 under the EM polymer quantization.

We stress though that this comparison only holds in the case where both sectors are equivalently quantized, even though there is no empirical evidence to support such a claim.

In the future we plan to use the polymer corrections to the GW waveform in Eqs. 6.20 and 6.19 to perform a full Bayesian analysis on the existing confirmed GW detections to estimate the PDFs on the polymer scales, similar to the study presented in the previous chapter.

# Chapter 7

# Conclusions

It has already been well-established in recent years that gravitational-wave observations open up an exciting new window into the Universe. The GWs produced by mergers of compact objects throughout the Universe carry with them information of their sources. Such properties can be–and have been–inferred, with sufficient modeling and proper statistical treatment, from the strain they place on GW observatories here on Earth. Analysis of the existing 90+ confident GW signals already observed has yielded novel insight into the characteristics and populations of the most extreme astrophysical objects in our Universe.

The GW models used are reflections of a sophisticated understanding of gravity on large scales. We've seen here that extending these models to include subtleties of GR, such as the detection of propagation of GWs on the interior of the null cone, could further solidify its success as a theory of gravity. Much like the first detection of GWs [76], further support for GR is not the only exciting prospect of the detection of gravitational glints. Their confirmation could also provide evidence for compact dark matter objects and even characterize their distribution on astrophysical scales. In this work, we've determined a model for the modification to the null cone GW signal and its manifestation in GW detectors. Additionally, we've forecasted the prospect of their detection as a function of the parameters introduced by the model modifications and characterized the expected level of precision to which the glint parameters can be inferred. We finally present the first search for gravitational glints through reanalysis of 47 GW events from the first three gravitational-wave transient catalogs, and present the Bayes factors for each. While we find no evidence for glints in the data analyzed, non-detection is consistent with rate estimates for detectable glints, leaving the potential for detection open as more GW data becomes public.

Direct detection of GWs also open the door to discovery of extensions of GR as well. Quantum effects of gravitational radiation represents one of the most elusive intersections of physical phenomena, and could potentially be demystified by GW data. Any quantum effects on gravitational waveforms are almost certainly too small to detect at the scales accessible to GW observatories, but accumulated effects such as deviations from the classically predicted propagation speed of GWs can result in observable time delays that become large over the vast distances between Earth and GW sources. Adopting the polymer quantization of gravitational radiation, we compute the first constraints on the scales describing polymer quantum effects from measurements of the deviation from classical propagation speed using two techniques. While each of these methods has drawbacks that affect their accuracy, like in the case of gravitational glints, additional observations will alleviate this uncertainty and could yield profound insights into the quantum nature of gravity.

Secondary effects present in GW data will be a focus of scientific endeavor as next-generation GW observatories arrive and bring with them improved detector sensitivities and an ever-growing catalog of GW events. Thus the machinery developed and tested in this work represents an exciting part of the preparation for the next era of GW astronomy.

# Bibliography

[1] Benjamin P Abbott et al. "Observation of gravitational waves from a binary black hole merger". In: *Physical review letters* 116.6 (2016), p. 061102 (cit. on p. 2).

[2] Wiley-Blackwell, 2011. ISBN: 9783527636037. DOI: `10.1002/9783527636037.ch3`. eprint: `https://onlinelibrary.wiley.com/doi/pdf/10.1002/9783527636037.ch3`. URL: `https://onlinelibrary.wiley.com/doi/abs/10.1002/9783527636037.ch3` (cit. on pp. 15, 20).

[3] Luc Blanchet. "Gravitational Radiation from Post-Newtonian Sources and Inspiralling Compact Binaries". In: *Living Reviews in Relativity* 17.1 (2014), p. 2. DOI: `10.12942/lrr-2014-2`. URL: `https://doi.org/10.12942/lrr-2014-2` (cit. on p. 26).

[4] Ian Hinder. "The current status of binary black hole simulations in numerical relativity". In: *Classical and Quantum Gravity* 27.11 (May 2010), p. 114004. DOI: `10.1088/0264-9381/27/11/114004`. URL: `https://dx.doi.org/10.1088/0264-9381/27/11/114004` (cit. on p. 26).

[5] P. Ajith et al. "Template bank for gravitational waveforms from coalescing binary black holes: Nonspinning binaries". In: *Phys. Rev. D* 77 (10 May 2008), p. 104017. DOI: `10.1103/PhysRevD.77.104017`. URL: `https://link.aps.org/doi/10.1103/PhysRevD.77.104017` (cit. on p. 26).

[6] Ilana MacDonald et al. "Suitability of post-Newtonian/numerical-relativity hybrid waveforms for gravitational wave detectors". In: *Classical and Quantum Gravity*

28.13 (June 2011), p. 134002. DOI: `10.1088/0264-9381/28/13/134002`. URL: `https://dx.doi.org/10.1088/0264-9381/28/13/134002` (cit. on p. 26).

[7] Thibault Damour et al. "Erratum: Comparison of search templates for gravitational waves from binary inspiral: 3.5PN update [Phys. Rev. D 66, 027502 (2002)]". In: *Phys. Rev. D* 72 (2 July 2005), p. 029901. DOI: `10.1103/PhysRevD.72.029901`. URL: `https://link.aps.org/doi/10.1103/PhysRevD.72.029901` (cit. on p. 27).

[8] Alejandro Bohé et al. "Improved effective-one-body model of spinning, nonprecessing binary black holes for the era of gravitational-wave astrophysics with advanced detectors". In: *Phys. Rev. D* 95 (4 Feb. 2017), p. 044028. DOI: `10.1103/PhysRevD.95.044028`. URL: `https://link.aps.org/doi/10.1103/PhysRevD.95.044028` (cit. on p. 27).

[9] Stanislav Babak et al. "Validating the effective-one-body model of spinning, precessing binary black holes against numerical relativity". In: *Phys. Rev. D* 95 (2 Jan. 2017), p. 024010. DOI: `10.1103/PhysRevD.95.024010`. URL: `https://link.aps.org/doi/10.1103/PhysRevD.95.024010` (cit. on p. 27).

[10] Andrea Taracchini et al. "Effective-one-body model for black-hole binaries with generic mass ratios and spins". In: *Phys. Rev. D* 89 (6 Mar. 2014), p. 061502. DOI: `10.1103/PhysRevD.89.061502`. URL: `https://link.aps.org/doi/10.1103/PhysRevD.89.061502` (cit. on p. 27).

[11] Andrea Taracchini et al. "Prototype effective-one-body model for nonprecessing spinning inspiral-merger-ringdown waveforms". In: *Phys. Rev. D* 86 (2 July 2012), p. 024011. DOI: `10.1103/PhysRevD.86.024011`. URL: `https://link.aps.org/doi/10.1103/PhysRevD.86.024011` (cit. on p. 27).

[12] L. Santamarıéa et al. "Matching post-Newtonian and numerical relativity waveforms: Systematic errors and a new phenomenological model for nonprecessing black hole binaries". In: *Phys. Rev. D* 82 (6 Sept. 2010), p. 064016. DOI: `10.1103/`

PhysRevD.82.064016. URL: https://link.aps.org/doi/10.1103/PhysRevD.82.064016 (cit. on p. 27).

[13] Mark Hannam et al. “Simple Model of Complete Precessing Black-Hole-Binary Gravitational Waveforms”. In: *Phys. Rev. Lett.* 113 (15 Oct. 2014), p. 151101. DOI: 10.1103/PhysRevLett.113.151101. URL: https://link.aps.org/doi/10.1103/PhysRevLett.113.151101 (cit. on p. 27).

[14] Sascha Husa et al. “Frequency-domain gravitational waves from nonprecessing black-hole binaries. I. New numerical waveforms and anatomy of the signal”. In: *Phys. Rev. D* 93 (4 Feb. 2016), p. 044006. DOI: 10.1103/PhysRevD.93.044006. URL: https://link.aps.org/doi/10.1103/PhysRevD.93.044006 (cit. on p. 27).

[15] Sebastian Khan et al. “Frequency-domain gravitational waves from nonprecessing black-hole binaries. II. A phenomenological model for the advanced detector era”. In: *Phys. Rev. D* 93 (4 Feb. 2016), p. 044007. DOI: 10.1103/PhysRevD.93.044007. URL: https://link.aps.org/doi/10.1103/PhysRevD.93.044007 (cit. on p. 27).

[16] B. P. Abbott et al. “GWTC-1: A Gravitational-Wave Transient Catalog of Compact Binary Mergers Observed by LIGO and Virgo during the First and Second Observing Runs”. In: *Phys. Rev. X* 9 (3 Sept. 2019), p. 031040. DOI: 10.1103/PhysRevX.9.031040. URL: https://link.aps.org/doi/10.1103/PhysRevX.9.031040 (cit. on pp. 28, 62, 65, 81).

[17] R. Abbott et al. “GWTC-2: Compact Binary Coalescences Observed by LIGO and Virgo during the First Half of the Third Observing Run”. In: *Phys. Rev. X* 11 (2 June 2021), p. 021053. DOI: 10.1103/PhysRevX.11.021053. URL: https://link.aps.org/doi/10.1103/PhysRevX.11.021053 (cit. on pp. 28, 62, 65).

[18] The LIGO Scientific Collaboration et al. “GWTC-3: Compact Binary Coalescences Observed by LIGO and Virgo During the Second Part of the Third Observing Run”. In: *arXiv e-prints*, arXiv:2111.03606 (Nov. 2021), arXiv:2111.03606. DOI:

10.48550/arXiv.2111.03606. arXiv: 2111.03606 [gr-qc] (cit. on pp. 28, 62, 65).

[19] Matthew Pitkin et al. "Gravitational Wave Detection by Interferometry (Ground and Space)". In: *Living Reviews in Relativity* 14.1 (2011), p. 5. DOI: 10.12942/lrr-2011-5. URL: https://doi.org/10.12942/lrr-2011-5 (cit. on p. 29).

[20] Brian J. Meers. "Recycling in laser-interferometric gravitational-wave detectors". In: *Phys. Rev. D* 38 (8 Oct. 1988), pp. 2317–2326. DOI: 10.1103/PhysRevD.38.2317. URL: https://link.aps.org/doi/10.1103/PhysRevD.38.2317 (cit. on p. 34).

[21] Muzammil A. Arain and Guido Mueller. "Design of the Advanced LIGO recycling cavities". In: *Opt. Express* 16.14 (July 2008), pp. 10018–10032. DOI: 10.1364/OE.16.010018. URL: https://opg.optica.org/oe/abstract.cfm?URI=oe-16-14-10018 (cit. on p. 34).

[22] J. Aasi et al. "Enhanced sensitivity of the LIGO gravitational wave detector by using squeezed states of light". In: *Nature Photonics* 7.8 (2013), pp. 613–619. DOI: 10.1038/nphoton.2013.177. URL: https://doi.org/10.1038/nphoton.2013.177 (cit. on p. 34).

[23] LIGO. *LIGO Livingston.* https://www.ligo.caltech.edu/WA/image/ligo20150731c. 2015 (cit. on p. 34).

[24] LIGO. *LIGO Hanford.* https://www.ligo.caltech.edu/WA/image/ligo20150731e. 2008 (cit. on p. 34).

[25] The Virgo collaboration/CCO 1.0. *Virgo.* https://www.ligo.caltech.edu/image/ligo20170927b. 2017 (cit. on p. 34).

[26] Bernard F Schutz. "Networks of gravitational wave detectors and three figures of merit". In: *Classical and Quantum Gravity* 28.12 (May 2011), p. 125023. DOI:

10.1088/0264-9381/28/12/125023. URL: https://dx.doi.org/10.1088/0264-9381/28/12/125023 (cit. on p. 35).

[27] Bruce Allen et al. "Robust statistics for deterministic and stochastic gravitational waves in non-Gaussian noise: Frequentist analyses". In: *Phys. Rev. D* 65 (12 June 2002), p. 122002. DOI: 10.1103/PhysRevD.65.122002. URL: https://link.aps.org/doi/10.1103/PhysRevD.65.122002 (cit. on p. 39).

[28] S.W. Hawking and W. Israel. *Three Hundred Years of Gravitation*. Philosophiae Naturalis, Principia Mathematica. Cambridge University Press, 1987. ISBN: 9780521379762. URL: https://books.google.com/books?id=Vq787qC5PWQC (cit. on p. 39).

[29] Nelson Christensen and Renate Meyer. "Using Markov chain Monte Carlo methods for estimating parameters with gravitational radiation data". In: *Phys. Rev. D* 64 (2 May 2001), p. 022001. DOI: 10.1103/PhysRevD.64.022001. URL: https://link.aps.org/doi/10.1103/PhysRevD.64.022001 (cit. on p. 40).

[30] Christian Röver et al. "Bayesian inference on compact binary inspiral gravitational radiation signals in interferometric data". In: *Classical and Quantum Gravity* 23.15 (July 2006), p. 4895. DOI: 10.1088/0264-9381/23/15/009. URL: https://dx.doi.org/10.1088/0264-9381/23/15/009 (cit. on p. 40).

[31] Christian Röver et al. "Coherent Bayesian inference on compact binary inspirals using a network of interferometric gravitational wave detectors". In: *Phys. Rev. D* 75 (6 Mar. 2007), p. 062004. DOI: 10.1103/PhysRevD.75.062004. URL: https://link.aps.org/doi/10.1103/PhysRevD.75.062004 (cit. on p. 40).

[32] M. V. van der Sluys et al. "Gravitational-Wave Astronomy with Inspiral Signals of Spinning Compact-Object Binaries". In: *The Astrophysical Journal* 688.2 (Oct. 2008), p. L61. DOI: 10.1086/595279. URL: https://dx.doi.org/10.1086/595279 (cit. on p. 40).

[33] Marc van der Sluys et al. "Parameter estimation of spinning binary inspirals using Markov chain Monte Carlo". In: *Classical and Quantum Gravity* 25.18 (Sept. 2008), p. 184011. DOI: `10.1088/0264-9381/25/18/184011`. URL: `https://dx.doi.org/10.1088/0264-9381/25/18/184011` (cit. on p. 40).

[34] Marc van der Sluys et al. "Parameter estimation for signals from compact binary inspirals injected into LIGO data". In: *Classical and Quantum Gravity* 26.20 (Oct. 2009), p. 204010. DOI: `10.1088/0264-9381/26/20/204010`. URL: `https://dx.doi.org/10.1088/0264-9381/26/20/204010` (cit. on p. 40).

[35] Nicholas Metropolis et al. "Equation of State Calculations by Fast Computing Machines". In: *The Journal of Chemical Physics* 21.6 (Dec. 2004), pp. 1087–1092. ISSN: 0021-9606. DOI: `10.1063/1.1699114`. eprint: `https://pubs.aip.org/aip/jcp/article-pdf/21/6/1087/8115285/1087\_1\_online.pdf`. URL: `https://doi.org/10.1063/1.1699114` (cit. on p. 41).

[36] W. K. HASTINGS. "Monte Carlo sampling methods using Markov chains and their applications". In: *Biometrika* 57.1 (Apr. 1970), pp. 97–109. ISSN: 0006-3444. eprint: `https://academic.oup.com/biomet/article-pdf/57/1/97/8545904/57-1-97.pdf` (cit. on p. 41).

[37] Robert H Swendsen and Jian-Sheng Wang. "Replica Monte Carlo simulation of spin-glasses". In: *Physical review letters* 57.21 (1986), p. 2607 (cit. on p. 42).

[38] Martin D. Weinberg. *Computing the Bayesian Factor from a Markov chain Monte Carlo Simulation of the Posterior Distribution.* 2010. arXiv: `0911.1777 [astro-ph.IM]` (cit. on p. 43).

[39] Tyson B. Littenberg and Neil J. Cornish. "Bayesian approach to the detection problem in gravitational wave astronomy". In: *Phys. Rev. D* 80 (6 Sept. 2009), p. 063007. DOI: `10.1103/PhysRevD.80.063007`. URL: `https://link.aps.org/doi/10.1103/PhysRevD.80.063007` (cit. on p. 43).

[40] John Skilling. "Nested sampling for general Bayesian computation". In: *Bayesian Analysis* 1.4 (2006), pp. 833–859. DOI: `10.1214/06-BA127`. URL: `https://doi.org/10.1214/06-BA127` (cit. on p. 44).

[41] J. Veitch and A. Vecchio. "Bayesian coherent analysis of in-spiral gravitational wave signals with a detector network". In: *Phys. Rev. D* 81 (6 Mar. 2010), p. 062003. DOI: `10.1103/PhysRevD.81.062003`. URL: `https://link.aps.org/doi/10.1103/PhysRevD.81.062003` (cit. on p. 44).

[42] Joshua S Speagle. "dynesty: a dynamic nested sampling package for estimating Bayesian posteriors and evidences". In: *Monthly Notices of the Royal Astronomical Society* 493.3 (Feb. 2020), pp. 3132–3158. ISSN: 0035-8711. DOI: `10.1093/mnras/staa278`. eprint: `https://academic.oup.com/mnras/article-pdf/493/3/3132/32890730/staa278.pdf`. URL: `https://doi.org/10.1093/mnras/staa278` (cit. on pp. 45, 47).

[43] J. Hadamard. *Lectures on Cauchy's Problem in Linear Partial Differential Equations*. Mrs. Hepsa Ely Silliman memorial lectures. Yale University Press, 1923. URL: `https://books.google.com/books?id=atVAAAAAIAAJ` (cit. on p. 49).

[44] Craig Copi and Glenn D. Starkman. "Gravitational Glint: Detectable Gravitational Wave Tails from Stars and Compact Objects". In: *Phys. Rev. Lett.* 128 (25 June 2022), p. 251101. DOI: `10.1103/PhysRevLett.128.251101`. URL: `https://link.aps.org/doi/10.1103/PhysRevLett.128.251101` (cit. on pp. 50, 72).

[45] K. Haris et al. *Identifying strongly lensed gravitational wave signals from binary black hole mergers*. 2018. arXiv: `1807.07062 [gr-qc]` (cit. on p. 57).

[46] Robert E. Kass and Adrian E. Raftery. "Bayes Factors". In: *Journal of the American Statistical Association* 90.430 (1995), pp. 773–795. DOI: `10.1080/01621459.1995.10476572`. eprint: `https://www.tandfonline.com/doi/pdf/10.1080/01621459.1995.10476572`. URL: `https://www.tandfonline.com/doi/abs/10.1080/01621459.1995.10476572` (cit. on p. 58).

[47] Planck Collaboration et al. “Planck 2015 results - XIII. Cosmological parameters”. In: *A&A* 594 (2016), A13. DOI: `10.1051/0004-6361/201525830`. URL: `https://doi.org/10.1051/0004-6361/201525830` (cit. on p. 59).

[48] Benjamin P Abbott et al. “GW170817: observation of gravitational waves from a binary neutron star inspiral”. In: *Physical Review Letters* 119.16 (2017), p. 161101 (cit. on pp. 62, 67, 89).

[49] B. P. Abbott et al. “GW190425: Observation of a Compact Binary Coalescence with Total Mass  3.4 M⊙”. In: *The Astrophysical Journal Letters* 892.1 (Mar. 2020), p. L3. DOI: `10.3847/2041-8213/ab75f5`. URL: `https://dx.doi.org/10.3847/2041-8213/ab75f5` (cit. on p. 62).

[50] R. Abbott et al. “GW190814: Gravitational Waves from the Coalescence of a 23 Solar Mass Black Hole with a 2.6 Solar Mass Compact Object”. In: *The Astrophysical Journal Letters* 896.2 (June 2020), p. L44. DOI: `10.3847/2041-8213/ab960f`. URL: `https://dx.doi.org/10.3847/2041-8213/ab960f` (cit. on pp. 62, 65, 67).

[51] Luciano Rezzolla et al. “Using Gravitational-wave Observations and Quasi-universal Relations to Constrain the Maximum Mass of Neutron Stars”. In: *The Astrophysical Journal Letters* 852.2 (Jan. 2018), p. L25. DOI: `10.3847/2041-8213/aaa401`. URL: `https://dx.doi.org/10.3847/2041-8213/aaa401` (cit. on p. 65).

[52] Philippe Landry and Jocelyn S. Read. “The Mass Distribution of Neutron Stars in Gravitational-wave Binaries”. In: *The Astrophysical Journal Letters* 921.2 (Nov. 2021), p. L25. DOI: `10.3847/2041-8213/ac2f3e`. URL: `https://dx.doi.org/10.3847/2041-8213/ac2f3e` (cit. on p. 65).

[53] Geraint Pratten et al. “Computationally efficient models for the dominant and subdominant harmonic modes of precessing binary black holes”. In: *Phys. Rev. D* 103 (10 May 2021), p. 104056. DOI: `10.1103/PhysRevD.103.104056`. URL: `https://link.aps.org/doi/10.1103/PhysRevD.103.104056` (cit. on p. 66).

[54] Éanna É. Flanagan and Tanja Hinderer. “Constraining neutron-star tidal Love numbers with gravitational-wave detectors”. In: *Phys. Rev. D* 77 (2 Jan. 2008), p. 021502. DOI: `10.1103/PhysRevD.77.021502`. URL: `https://link.aps.org/doi/10.1103/PhysRevD.77.021502` (cit. on p. 66).

[55] Marc Favata. “Systematic Parameter Errors in Inspiraling Neutron Star Binaries”. In: *Phys. Rev. Lett.* 112 (10 Mar. 2014), p. 101101. DOI: `10.1103/PhysRevLett.112.101101`. URL: `https://link.aps.org/doi/10.1103/PhysRevLett.112.101101` (cit. on p. 66).

[56] Leslie Wade et al. “Systematic and statistical errors in a bayesian approach to the estimation of the neutron-star equation of state using advanced gravitational wave detectors”. In: *Phys. Rev.* D89.10 (2014), p. 103012. DOI: `10.1103/PhysRevD.89.103012`. arXiv: `1402.5156 [gr-qc]` (cit. on p. 66).

[57] Benjamin D. Lackey and Leslie Wade. “Reconstructing the neutron-star equation of state with gravitational-wave detectors from a realistic population of inspiralling binary neutron stars”. In: *Phys. Rev.* D91.4 (2015), p. 043002. DOI: `10.1103/PhysRevD.91.043002`. arXiv: `1410.8866 [gr-qc]` (cit. on p. 66).

[58] Ka-Wai Lo and Lap-Ming Lin. “THE SPIN PARAMETER OF UNIFORMLY ROTATING COMPACT STARS”. In: *The Astrophysical Journal* 728.1 (Jan. 2011), p. 12. DOI: `10.1088/0004-637X/728/1/12`. URL: `https://dx.doi.org/10.1088/0004-637X/728/1/12` (cit. on p. 66).

[59] Jason W. T. Hessels et al. “A Radio Pulsar Spinning at 716 Hz”. In: *Science* 311.5769 (2006), pp. 1901–1904. DOI: `10.1126/science.1123430`. eprint: `https://www.science.org/doi/pdf/10.1126/science.1123430`. URL: `https://www.science.org/doi/abs/10.1126/science.1123430` (cit. on p. 66).

[60] M. Burgay et al. “An increased estimate of the merger rate of double neutron stars from observations of a highly relativistic system”. In: *Nature* 426.6966 (2003),

pp. 531–533. DOI: `10.1038/nature02124`. URL: `https://doi.org/10.1038/nature02124` (cit. on p. 66).

[61] B. P. Abbott et al. “Properties of the Binary Neutron Star Merger GW170817”. In: *Phys. Rev. X* 9 (1 Jan. 2019), p. 011001. DOI: `10.1103/PhysRevX.9.011001`. URL: `https://link.aps.org/doi/10.1103/PhysRevX.9.011001` (cit. on p. 68).

[62] Yuri Bonder et al. “Bounds on the polymer scale from gamma ray bursts”. In: *Phys. Rev. D* 96 (10 Nov. 2017), p. 106021. DOI: `10.1103/PhysRevD.96.106021`. URL: `https://link.aps.org/doi/10.1103/PhysRevD.96.106021` (cit. on pp. 73, 87, 94).

[63] M. Ackermann et al. “FERMI OBSERVATIONS OF GRB 090510: A SHORT–HARD GAMMA-RAY BURST WITH AN ADDITIONAL, HARD POWER-LAW COMPONENT FROM 10 keV TO GeV ENERGIES”. In: *The Astrophysical Journal* 716.2 (May 2010), p. 1178. DOI: `10.1088/0004-637X/716/2/1178`. URL: `https://dx.doi.org/10.1088/0004-637X/716/2/1178` (cit. on p. 73).

[64] Abhay Ashtekar et al. “Quantum gravity, shadow states and quantum mechanics”. In: *Classical and Quantum Gravity* 20.6 (Feb. 2003), p. 1031. DOI: `10.1088/0264-9381/20/6/302`. URL: `https://dx.doi.org/10.1088/0264-9381/20/6/302` (cit. on p. 74).

[65] Alejandro Corichi et al. “Polymer quantum mechanics and its continuum limit”. In: *Phys. Rev. D* 76 (4 Aug. 2007), p. 044016. DOI: `10.1103/PhysRevD.76.044016`. URL: `https://link.aps.org/doi/10.1103/PhysRevD.76.044016` (cit. on p. 74).

[66] Hugo A. Morales-Técotl et al. “Path integral polymer propagator of relativistic and nonrelativistic particles”. In: *Phys. Rev. D* 95 (6 Mar. 2017), p. 065026. DOI: `10.1103/PhysRevD.95.065026`. URL: `https://link.aps.org/doi/10.1103/PhysRevD.95.065026` (cit. on p. 74).

[67] Hugo A. Morales-Técotl et al. “Polymer quantization and the saddle point approximation of partition functions”. In: *Phys. Rev. D* 92 (10 Nov. 2015), p. 104029. DOI: `10.1103/PhysRevD.92.104029`. URL: `https://link.aps.org/doi/10.1103/PhysRevD.92.104029` (cit. on p. 74).

[68] Nirmalya Kajuri. “Strong equivalence principle in polymer quantum mechanics and deformed Heisenberg algebra”. In: *Phys. Rev. D* 94 (8 Oct. 2016), p. 084007. DOI: `10.1103/PhysRevD.94.084007`. URL: `https://link.aps.org/doi/10.1103/PhysRevD.94.084007` (cit. on p. 74).

[69] Angel Garcia-Chung et al. “Propagation of quantum gravity-modified gravitational waves on a classical FLRW spacetime”. In: *Phys. Rev. D* 103 (8 Apr. 2021), p. 084053. DOI: `10.1103/PhysRevD.103.084053`. URL: `https://link.aps.org/doi/10.1103/PhysRevD.103.084053` (cit. on p. 74).

[70] Angel Garcia-Chung et al. *A model of polymer gravitational waves: theory and some possible observational consequences*. 2022. arXiv: `2111.00292 [gr-qc]` (cit. on p. 74).

[71] Angel Garcia-Chung et al. “What do gravitational wave detectors say about polymer quantum effects?” In: *Journal of Cosmology and Astroparticle Physics* 2022.11 (Nov. 2022), p. 054. DOI: `10.1088/1475-7516/2022/11/054`. URL: `https://dx.doi.org/10.1088/1475-7516/2022/11/054` (cit. on pp. 78, 79).

[72] B. P. Abbott et al. “Gravitational Waves and Gamma-Rays from a Binary Neutron Star Merger: GW170817 and GRB 170817A”. In: *The Astrophysical Journal Letters* 848.2 (Oct. 2017), p. L13. DOI: `10.3847/2041-8213/aa920c`. URL: `https://dx.doi.org/10.3847/2041-8213/aa920c` (cit. on pp. 80, 87, 88).

[73] Xiaoshu Liu et al. “Measuring the speed of gravitational waves from the first and second observing run of Advanced LIGO and Advanced Virgo”. In: *Phys. Rev. D* 102 (2 July 2020), p. 024028. DOI: `10.1103/PhysRevD.102.024028`. URL:

https://link.aps.org/doi/10.1103/PhysRevD.102.024028 (cit. on pp. 80–82).

[74] Riccardo Ciolfi and Daniel M. Siegel. "SHORT GAMMA-RAY BURSTS IN THE "TIME-REVERSAL" SCENARIO". In: *The Astrophysical Journal Letters* 798.2 (Dec. 2014), p. L36. DOI: 10.1088/2041-8205/798/2/L36. URL: https://dx.doi.org/10.1088/2041-8205/798/2/L36 (cit. on p. 88).

[75] Luciano Rezzolla and Pawan Kumar. "A NOVEL PARADIGM FOR SHORT GAMMA-RAY BURSTS WITH EXTENDED X-RAY EMISSION". In: *The Astrophysical Journal* 802.2 (Mar. 2015), p. 95. DOI: 10.1088/0004-637X/802/2/95. URL: https://dx.doi.org/10.1088/0004-637X/802/2/95 (cit. on p. 88).

[76] B. P. Abbott et al. "Observation of Gravitational Waves from a Binary Black Hole Merger". In: *Phys. Rev. Lett.* 116 (6 Feb. 2016), p. 061102. DOI: 10.1103/PhysRevLett.116.061102. URL: https://link.aps.org/doi/10.1103/PhysRevLett.116.061102 (cit. on p. 96).